

**BRNO UNIVERSITY OF TECHNOLOGY**

VYSOKÉ UČENÍ TECHNICKÉ V BRNĚ

**CENTRAL EUROPEAN INSTITUTE OF TECHNOLOGY BUT**

STŘEDOEVROPSKÝ TECHNOLOGICKÝ INSTITUT VUT

**STRUCTURE AND PROPERTIES OF HYDROXYAPATITE-  
MAGNESIUM COMPOSITES PRODUCED BY THE MEANS  
OF CURRENT ASSISTED INFILTRATION SINTERING**

STRUKTURA A VLASTNOSTI KOMPOZITŮ NA BÁZI HYDROXYAPATITU A HOŘČÍKU, PŘIPRAVOVANÝCH  
METODOU PROUDEM ASISTOVANÉ SLINOVACÍ INFILTRACE

**DOCTORAL THESIS**

DIZERTAČNÍ PRÁCE

**AUTHOR**

AUTOR PRÁCE

**Mariano Casas Luna**

**SUPERVISOR**

ŠKOLITEL

**doc. Ing. Ladislav Čelko, Ph.D.**

**BRNO 2020**



## ABSTRACT

Magnesium and calcium phosphate composites are promising materials to create biodegradable and load-bearing implants for bone regeneration. The present work is focused on the design, processing and characterization of interpenetrated magnesium / calcium phosphate (Mg/CaP) composites. Calcium phosphates such as, hydroxyapatite (HA), calcium-deficient HA (CDHA) and tricalcium phosphate (TCP) were synthesized and used for the production of controlled porous scaffolds by means of robocasting technique. The final porous preforms with an orthogonal grid arrangement and internal macro-pores of  $\sim 500 \mu\text{m}$  were obtained and sintered at  $1100 \text{ }^\circ\text{C}$  for 5 h. The Mg/CaP interpenetrated composites were obtained by infiltrating the porous ceramic scaffolds with pure Mg and Mg alloys containing low amounts of calcium or zinc, i.e. Mg – 0.2 wt.% Ca and Mg – 1 wt.% Zn. The infiltration was carried out using a here-developed and recently introduced technique referred to as Current-Assisted Metal Infiltration (CAMI). The CAMI methodology allowed the infiltration of porous ceramic preforms with a molten metal in less than 15 minutes. Fast melting and final solidification of the Mg/CaP composites was achieved with the assistance of pulsed electrical current. The final interpenetrated composites were physicochemically characterized by means of scanning electron microscopy, X-ray computed micro-tomography, X-ray diffraction and optical microscopy in order to determine the phase distribution and the interaction between the materials. In addition, the mechanical resistance under compression, the degradation rate by different techniques, and the biocompatibility of the produced composites were evaluated in an attempt to introduce these types of materials as potential degradable biomaterials for use in the manufacturing of plates and/or screws for orthopaedics.

## Abstrakt

Hořík a kompozity fosforečnanu vápenatého jsou slibnými materiály pro biodegradabilní a nosné implantáty určené pro regeneraci kostí. Předložená práce je zaměřena na návrh, zpracování a charakterizaci vnitřně propojených kompozitů hoříku s fosforečnanem vápenatým (Mg/CaP). Fosforečnany vápenaté jako jsou hydroxyapatit (HA), kalcium-deficitní hydroxyapatit (CDHA) a fosforečnan vápenatý (TCP) byly syntetizovány a použity pro výrobu skafoldů s kontrolovanou porozitou pomocí metody robocastingu. Byly připraveny porézní předlisky s ortogonální mřížkou a s vnitřními makropóry o velikosti  $\sim 500 \mu\text{m}$ , které byly následně slinovány za teploty  $1100 \text{ }^\circ\text{C}$  po dobu 5 hodin. Vnitřně propojené Mg/CaP kompozity byly připraveny infiltrací čistého hoříku a hoříkových slitin obsahujících malá množství vápníku nebo zinku, například 0,2 hm.% vápníku a 1 hm.% zinku do porézních keramických skafoldů. Infiltrace byla provedena pomocí naší vyvinuté a nově popsané metody známé jako “Proudem asistovaná slinovací infiltrace” (z angl. Current Assisted Metal Infiltration (CAMI)). CAMI metoda umožňuje do 15 minut infiltrovat porézní keramický předlisek roztaveným kovem. Pulzujícím elektrickým proudem bylo dosaženo rychlého tavení a následného tuhnutí Mg/CaP kompozitů. Fyzikálně-chemické vlastnosti finálních vnitřně propojených kompozitů byly stanoveny pomocí rastrovací elektronové mikroskopie, počítačové mikro-tomografie, rentgenové difrakční analýzy a optické mikroskopie za účelem stanovení fázové distribuce a interakce mezi materiály. Kromě toho byla u připravených kompozitů hodnocena jejich mechanická pevnost v tlaku, degradační rychlost pomocí různých metod a biokompatibilita spolu s pokusem o uvedení těchto typů materiálů jako potenciálních biodegradabilních biomateriálů určených pro výrobu desek a/nebo šroubů pro ortopedické aplikace.

**KEYWORDS:**

Magnesium, Hydroxyapatite, tricalcium phosphate, interpenetrated composites, Mechanical properties, Corrosion behaviour, Cytotoxicity.

**Klíčová Slova:**

Hořčík, Hydroxyapatit, trikalciumfosfát, interpenetratované kompozity, mechanické vlastnosti, korozní chování, cytotoxicita.

**BIBLIOGRAPHIC CITATION:**

CASAS LUNA, Mariano. *Structure and properties of Hydroxyapatite-Magnesium composites produced by the means of current assisted infiltration sintering*. Brno, 2020. Available from: <https://www.vutbr.cz/studenti/zav-prace/detail/128705>. Doctoral Thesis. Brno University of Technology, Central European Institute of Technology BUT. Supervisor Ladislav Čelko.

**Bibliografická Citace:**

CASAS LUNA, Mariano. *Struktura a vlastnosti kompozitů na bázi hydroxyapatitu a hořčíku, připravovaných metodou proudem asistované slinovací infiltrace*. Brno, 2020. Dostupné také z: <https://www.vutbr.cz/studenti/zav-prace/detail/128705>. Dizertační práce. Vysoké učení technické v Brně, Středoevropský technologický institut VUT, Středoevropský technologický institut VUT. Vedoucí práce Ladislav Čelko.

### **SWORN STATEMENT**

I hereby declare that I have written the PhD thesis on my own according to advice of my supervisor Assoc. Prof. Ladislav Čelko and that all the literary sources are quoted correctly and completely. This dissertation thesis is the property of the Central European Institute of Technology (CEITEC), Brno University of Technology (BUT), Czech Republic.

### **Čestné prohlášení**

Tímto prohlašuji, že jsem vypracoval doktorskou práci sám, dle doporučení vedoucího Assoc. Prof. Ladislav Čelko a že všechny literární zdroje jsou citovány správně a úplně. Tato disertační práce je majetkem Středoevropského technologického institutu (CEITEC), VUT v Brně.

**Mariano Casas Luna**

## ACKNOWLEDGEMENTS

To complete this thesis would not be possible without the generous constant support and help from the following people:

Special thanks to my supervisor Assoc. Prof. Ladislav Čelko, who has friendly instructed me all along the journey at the CEITEC-BUT.

My thanks go:

to Dr. Sebastián Díaz de la Torre and Dr. Edgar B. Montúfar, who helped me through the studies and shared their knowledge with me,

to my lovely family who despite the distance have always supported me. I love them,

to all my friends in the Czech Republic who helped me make the best of my stay in this beautiful country,

to my lunch-relax friends (Jorge and Martha), who almost every day were there to make my work easier,

to my colleagues and Professors at Brno University of Technology who helped me to improve my ideas and form myself in this career.

## CONTENT

<b>1. Introduction.....</b>	<b>8</b>
<b>2. Literature review.....</b>	<b>10</b>
2.1. Biomaterials .....	10
2.1.1. Degradable biomaterials .....	11
2.2. Bioabsorbable calcium phosphates (CaP) as orthopaedic materials .....	13
2.3. Magnesium and its alloys as degradable biomaterials for orthopaedic applications .....	15
2.4. Robocasting of porous controlled scaffolds.....	19
2.5. Liquid metal infiltration: manufacturing of interpenetrated composites.....	20
2.5.1. Current-assisted metal infiltration (CAMI).....	21
2.6. Magnesium / Calcium-phosphate (Mg/CaP) composite biomaterials.....	23
2.6.1. Mechanical properties of Mg/CaP composites.....	25
2.6.2. Corrosion behaviour of Mg/CaP composites .....	26
2.6.3. Biocompatibility of Mg/CaP composites.....	28
2.7 Remarks about Mg/CaP composites .....	29
<b>3. Aims of the Thesis .....</b>	<b>30</b>
<b>4. Materials and Methods .....</b>	<b>31</b>
4.1. Synthesis of calcium phosphates (CaP's) and production of controlled porous scaffolds .	31
4.1.1. Synthesis of HA and $\beta$ -TCP powders.....	31
4.1.2. Synthesis of calcium-deficient hydroxyapatite by hydration of $\alpha$ -TCP .....	32
4.1.3. Direct ink writing of calcium-phosphate injectable pastes .....	33
4.2. Manufacturing by indirect chill casting of Mg alloys .....	34
4.3. Magnesium infiltration of CaP scaffolds by current-assisted metal infiltration (CAMI) ..	35
4.4. Characterization of Mg alloys and Mg/CaP interpenetrated composites .....	37
4.4.1. Physicochemical characterization .....	37
4.4.2. Mechanical properties.....	38
4.4.3. Degradation assessment under simulated physiological conditions.....	39

4.4.3.1. H <sub>2</sub> evolution assessment.....	40
4.4.3.2. Tafel extrapolation of polarization curves .....	40
4.5. Biocompatibility evaluation.....	41
4.6 Statistical analysis .....	42
<b>5. Results and Discussion .....</b>	<b>43</b>
5.1 Infiltration of $\beta$ -TCP scaffolds with Mg: Preliminary case study and proof of concept.....	43
5.1.1 Processing of initial materials .....	43
5.1.2 Robocasting of $\beta$ -TCP scaffolds with different pore sizes .....	44
5.1.3 Manufacturing and characterization of Mg/ $\beta$ -TCP interpenetrated composites .....	46
5.2. Manufacturing and testing of interpenetrated Mg/CaP systems. ....	54
5.2.1 Synthesis and manufacturing of CaP scaffolds. ....	54
5.2.2. Casting of pure Mg, Mg-Ca and Mg-Zn alloys and their degradation behaviour in simulated body fluid.....	61
5.2.3. Development of interpenetrated Mg/CaP composites .....	69
5.2.3.1. Mechanical behaviour of interpenetrated Mg/CaP composites .....	79
5.2.3.1. Corrosion resistance of interpenetrated Mg/CaP composites.....	85
5.2.3.1. Cytotoxicity and cell viability of interpenetrated Mg/CaP composites .....	91
<b>6. Conclusions.....</b>	<b>96</b>
<b>Suggested future work .....</b>	<b>99</b>
<b>Bibliography.....</b>	<b>100</b>
<b>List of abbreviations .....</b>	<b>119</b>
<b>List of publications.....</b>	<b>121</b>
<b>Patents .....</b>	<b>122</b>
<b>Internship, trainings and other activities.....</b>	<b>123</b>
<b>Participation in research projects .....</b>	<b>123</b>
<b>List of figures .....</b>	<b>124</b>
<b>List of tables .....</b>	<b>128</b>

## 1. INTRODUCTION

At the present human life, where the number of inhabitants has increased tremendously together with the life expectancy, health problems such as degenerative diseases including accidents that could cause any kind of injuries are promoting the development of useful techniques and materials capable of solving efficiently and economically the required medical applications.

Bone degenerative problems besides numerous bone fractures, osteoporosis, and other musculoskeletal problems are affecting millions of people worldwide and they need to be solved by using permanent or temporary implants. The number of new fractures in 2010 in the EU was estimated at 3.5 million, expecting a rise of 28% by 2025 [1]. Only in the Czech Republic, approximately 72,000 fractures were reported in 2010, representing an average economic burden of € 273 million each year [2]. From this point of view, the design and study of new materials for orthopaedic applications are of high interest for the industry and the research field, with the aim to increase the quality of life among afflicted people.

Orthopaedic biomaterials are meant to be implanted in the human body as constituents of devices that are designed to perform certain biological functions by substituting or repairing different bone tissues.

Up to now, a wide range of materials have been used for bone repairs. Metallic devices are usually implanted for load bearing applications while ceramics and polymers are mostly used as bioactive and degradable materials, respectively. Recently, new types of advanced composites have appeared because of their unique properties inside the human body, combining bioactivity with adjusted mechanical behaviour.

Calcium phosphates (CaP's) such as hydroxyapatite (HA), calcium-deficient hydroxyapatite (CDHA) and tricalcium phosphates ( $\alpha$ -TCP or  $\beta$ -TCP) are the most commonly used materials for bioactive implants due to their chemical composition, which is similar to the inorganic phase of the natural bone. This chemical composition similarity gives them good biocompatibility. However, the ceramic nature of CaP's makes them possess low ductility and fragile behaviour, impeding their application in the treatment of bone defects under load-bearing conditions.

Consequently, metallic and CaP degradable composites are gaining attraction for the fabrication of osteosynthetic implants [3–5]. The driving force is the effort to increase the

mechanical strength of CaP's, without sacrificing its degradability and osteoconductivity [6,7]. Among the different degradable metals available, magnesium (Mg) appears to be one of the best alternatives due to its good tolerance in the human body, its osteogenic effect, and mechanical properties similar to the human bone [8–10]. Nevertheless, the degradation rate of pure magnesium is faster than the bone regenerative capacity and several works are focused on increasing its corrosion resistance in the biological environment [9,11–14].

Composites and functionally graded materials (FGM's) consisting of Mg and CaP are a promising solution to yield bioactive/degradable implants in orthopaedics. Different methods have been developed to produce Magnesium - Calcium phosphate (Mg/CaP) composites. For example, common powder metallurgy routes are used to produce particle-reinforced composites, with either Mg or CaP matrix [4,5,7]. A high-performance type of composites are the interpenetrated materials, in which both the matrix and the reinforcement form a continuous three-dimensional network in the material [15]. Most of the interpenetrated composites are fabricated by metal infiltration of the porous ceramic preforms [16,17], having as a limitation the mechanical strength of the preform [17].

In the present work, the synthesis and production of functionally interpenetrated materials based on CaP (such as HA and TCP) and Mg alloys (i.e. Mg-Ca and Mg-Zn) was performed. Robocasting was used to build cylindrical CaP scaffolds with interconnected pores of ~500  $\mu\text{m}$ . Later, scaffolds of ~8 mm in diameter and ~10 mm in height were successfully infiltrated by Mg or Mg alloys to obtain the interpenetrated Mg/CaP composites. At the same time, a new pressureless infiltration method was explored and implemented in the study. The process referred to as current-assisted metal infiltration (CAMI) uses the principle of spark plasma sintering [18,19] to melt magnesium under vacuum, and once it is in the liquid state, infiltrate the bioceramic preform by gravity and vacuum suction. Finally, the chemical and the structural characterizations of the interpenetrated composites were performed and their degradation rate and cytotoxicity response were calculated under simulated physiological conditions as an initial attempt to use these composites as resorbable biomaterials for orthopaedic applications.

## 2. LITERATURE REVIEW

### 2.1. BIOMATERIALS

The term biomaterial is used for any material used to make devices that replace a part of a living system or function in intimate contact with a living tissue in a safe, reliable, economic, and physiologically acceptable manner. The use of biomaterials ranges from replacing of a body part that has lost its function due to disease or trauma, to assisting in healing, improving or correcting a function or cosmetic abnormalities, and serving as an aid to diagnosis and treatment [20].

During most of the last century, the availability of biomaterials for the production of implants was based on the materials developed for other industrial applications [20,21]. Nevertheless, the human body represents a multifaceted and dynamic environment; strict requirements are mandatory on the properties of the biomaterials. Among these requirements, the biocompatibility and the mechanical properties are the most important aspects that play the leading role in the material selection during the design and manufacturing of implants [20]. The evolution of biomaterials - and consequently the so-called tissue engineering - is classified in three different generations, which are not chronological. The first generation consisted of inert materials that were available from the industrial applications, and its main requirement was to be completely inert in order to avoid the corrosion and release of particles or ions after implantation [21]. Later on, during the second generation, the concept of biocompatibility - associated with toxicity - was introduced in order to evaluate the biological behaviour of materials when they exhibited some bioactive response of a certain degradation process (biodegradability) [21,22]. Finally, the third generation opened up new possibilities for different applications; the novel materials in this stage are designed to stimulate some specific biological response at the molecular level [22,23].

The improvement in the materials for any kind of application that implies the human body contact, like in the case of tissue engineering, has been achieved thanks to the development of the studies of advanced materials which possess similar properties that mimic natural tissues (**Figure 1**). Advances in research and the technological development in this field continue to progress, based on the large funds and grants provided by government bodies worldwide and on the rising demand for medical implants. According to a survey by Markets & Markets 2019, the global biomaterials market is set to reach almost US \$ 207 billion by 2024, having an annual growth rate of 14.5 %, and representing one of the fastest growing economic sectors [24].

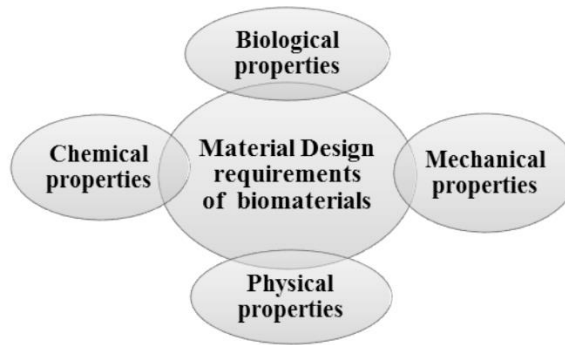


**Figure 1.** Schematic representation of material design requirement for biomaterials

### **2.1.1. DEGRADABLE BIOMATERIALS**

The study and design of degradable biomaterials has become one of the most revolutionary research topics at the forefront of the biomaterials field. This novel class of biomaterials are expected to be used as implants to fulfil a temporary function. The use of temporary implants is necessary in clinical cases where the implant covers the function of the surrounding living tissue while the body regenerates and heals [3,25].

Most of the commercial implants used nowadays are permanent devices. Nevertheless, the possibility of tailored degradable biomaterials was opened with the evolution of biocompatible resorbable polymers [3]. The use of degradable implants is important in some orthopaedic and cardiovascular applications where the implant must be removed after the healing of the damaged tissue, involving a second surgery, which implies personal, medical, social, and economic consequences [26]. All such complications can be solved by the development of degradable biomaterials with controlled degradation rate inside the human body. Therefore, over the last two decades, significant scientific and industrial efforts have been conducted to develop not only degradable polymers but also ceramic and metallic materials for implants that can combine the required mechanical properties and an adequate degradation rate under physiological conditions [3].

An ideal degradable material should exhibit bioactivity while the degradation rate is in accordance with the healing time without compromising the mechanical requirements during the process (**Figure 2**). In addition, the corrosion/degradation products must be inert – not toxic – in the human body [3,26]. Thus, depending on the tissue being reabsorbed and regenerated, degradable polymers, ceramics or even metals can be used. In the case of soft tissues, polymers

and hydrogels are the best option while for hard tissues – as in orthopaedics – ceramics and metals are more convenient.

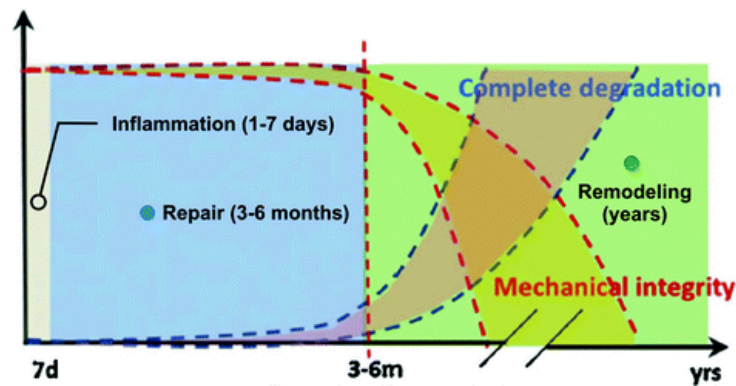


**Figure 2.** Schematic time-line for an ideal degradable biomaterial depicting the healing period against the degradation time [3].

In the case of bone regeneration, avoiding a second surgery to remove implants like plates or screws is of high importance since it reduces the risk to both the specialist and the patient. In these terms, degradable polymers are mostly limited to low load-bearing applications due to their scarce mechanical properties, and in this field the degradable ceramics or metals fulfil this requirement and extend the possibilities for the development of a next generation of degradable and bioactive implants for orthopaedics.

The most studied ceramics in orthopaedics are the family of calcium phosphates due to their very well-known bioactivity, mostly osteoconductivity, which is a product of their chemical composition, similar to the inorganic phase of bones [27,28]. Additionally, some of the calcium phosphates possess some reabsorption properties when they are implanted. In the same way, some silicate-based ceramics known as bioactive glasses – or bioglasses, BGs – are gaining attention due to their good bioabsorption behaviour [29].

In the case of metals, even though they exhibit excellent mechanical properties with more ductility response than ceramics, the selection of the material is limited to the biocompatibility properties. Up to now, most of the metallic implants are based on titanium and stainless steel alloys, which can be bioactive and chemically stable without exhibiting any degradability properties.

The term degradable biometal was introduced during the last decade with the aim of developing new metallic implants that can solve the problem of avoiding a second surgery and extend the use of temporal implants when they are needed. Nevertheless, the selection of a degradable biometal is quite restricted to the corrosion products and the degradation mechanism. Thus, the corrosion route must follow a biocompatible mechanism while assuring the integrity of the implant for guaranteeing the mechanical reliability during the healing process of the surrounding tissue. Only a few metals share the mentioned characteristic and the most studied candidates have until now been magnesium, iron, zinc, and their alloys [3,30].

Despite all the research, more investigation into degradable biomaterials that covers the best healing rate with appropriate mechanical and biocompatible properties is needed and is of high industrial and health importance.

## **2.2. BIOABSORBABLE CALCIUM PHOSPHATES (CAP) AS ORTHOPAEDIC MATERIALS**

Calcium phosphates belong to the group of bioactive ceramics that can trigger bone regeneration due to their chemical composition, similar to the natural bone. These bioceramics promote osteoinduction and osteoconduction by the interaction with the bone cells that leads to the reabsorption of these ceramics and their transformation into natural bone [6,28,31]. Osteoinduction is the process by which osteogenesis – bone regeneration – is induced and it happens during any type of bone healing [32]. On the other hand, osteoconduction is the process that involves the active surface of a material that is in contact with the bone tissue and promotes the growing of bone tissue on the surface of the material, which is a crucial process for the bone implants [33].

Among the most widely used CaP in orthopaedics and dentistry, hydroxyapatite – HA,  $\text{Ca}_{10}(\text{PO}_4)_6(\text{OH})_2$  – is the most renowned one and it has been tested as artificial bone since its chemical composition and structure are linked to the inorganic phase of the natural bone. Additionally, HA exhibits one the best biocompatibility responses in long-term implants for orthopaedics [34,35]. As a result, stoichiometric HA has been widely synthesised by many chemical routes and used to manufacture diverse forms of implants, as well as a coating on metallic prostheses with the aim to improve the bioactivity and adhesion of the implant [36–39]. Synthetic HA differs in chemical composition from the one in the mineral phase of bone. The inorganic phase

of bones is composed of apatite crystals arranged like the stoichiometric hydroxyapatite but with some deficiency of calcium and some ion exchange, containing ions such as sodium, magnesium and carbonate [40]. Even though the stoichiometric HA differs in composition from the natural mineral phase of bone, it does not affect the stability and biocompatibility of the synthetic HA devices; however, the stoichiometric HA has a very low dissolubility when it is implanted, compared with other CaP compounds.

On the contrary, when stoichiometric HA is deficient in calcium, known as calcium-deficient hydroxyapatite (CDHA,  $\text{Ca}_9(\text{HPO}_4)(\text{PO}_4)_5(\text{OH})$ ), the compound is more favourable as bone graft because it has a faster dissolution rate under physiological conditions than stoichiometric HA has. Additionally, CDHA has a higher osteoconduction, enabling fast bonding and interaction with the bone cells [41]. The main and easiest route to obtaining CDHA is to hydrate the monoclinic tricalcium phosphate ( $\alpha$ -TCP) in aqueous solution using elevated temperatures below 100 °C [42]. Chemical routes are more complex due to the post-processing of the obtained material that in most of the cases should be calcined or sintered, which is a process that makes the CDHA decompose into the low-temperature polymorph of tricalcium phosphate ( $\beta$ -TCP) due to loss of water between 700 and 800 °C [43].

Another widely used resorbable CaP is the tricalcium phosphate (TCP,  $\text{Ca}_3(\text{PO}_4)_2$ ), which is widely accepted for the fabrication of temporary implants because of its degradation capability inside the body and its excellent biocompatibility [44,45]. TCP exists in the form of three crystalline structures: monoclinic or  $\alpha$ -TCP, hexagonal or  $\alpha'$ -TCP (not stable at room temperature), and rhombohedral or  $\beta$ -TCP. The monoclinic and hexagonal phases are stable at high temperatures, above 1150 °C and >1430 °C, respectively [46]. However, an abrupt quenching of the ceramic can preserve the  $\alpha$ -TCP at room temperature as a metastable phase. TCP polymorphs differ significantly in their crystalline structure, consequently in their density and solubility, which in turn determine their biological response and clinical applications. Then,  $\alpha$ -TCP presents faster resorption than the  $\beta$ -TCP due to the rapid hydrolysis to CDHA [46]. However, both phases are now used for clinical applications in orthopaedics and dentistry; currently,  $\beta$ -TCP is one of the components of several commercial bioceramics and composites while  $\alpha$ -TCP is the major constituent in the fabrication of many calcium phosphate cements [27,46,47].

The biological response *in vivo*, as the resorption rate of the CaP, is a function of the chemical composition, crystallographic structure and microstructural morphology of these bioceramics. Under physiological conditions, i.e. pH = 7.2 – 7.4, the concentration of dissolved Ca and P from the here-mentioned CaP's decreases in the following order:  $\alpha$ -TCP >  $\beta$ -TCP > CDHA > HA (**Table 1**) [42,48]. Under these conditions, HA is the most stable phase and therefore it is the main precipitation product during the biodegradation and mineralization of the CaP bioceramics.

**Table 1.** Chemical formulas, Ca/P atomic ratios and solubility of some CaP compounds

Compound	Chemical formula (Ca/P)	Solubility [ $-\log(K_s)$ ]	
		25 °C	37 °C
$\alpha$ -Tricalcium phosphate $\alpha$ -TCP	$\alpha$ -Ca <sub>3</sub> (PO <sub>4</sub> ) <sub>2</sub> (1.5)	25.5	25.5
$\beta$ -Tricalcium phosphate $\beta$ -TCP	$\beta$ -Ca <sub>3</sub> (PO <sub>4</sub> ) <sub>2</sub> (1.5)	28.9	29.5
Calcium deficient hydroxyapatite CDHA	Ca <sub>9</sub> (HPO <sub>4</sub> )(PO <sub>4</sub> ) <sub>5</sub> (OH) (1.5 – 1.67)	~85.1	~85.1
Hydroxyapatite HA	Ca <sub>10</sub> (PO <sub>4</sub> ) <sub>6</sub> (OH) <sub>2</sub> (1.67)	116.8	117.2

The biodegradability of CaP's is considerably improved by increasing the porosity of the implants or scaffolds. Ideally, micro-porosity should be interconnected to allow the ingrowth of cells and vascularization [49,50]. In these terms, the desired porosity necessary to promote the absorption of the bioceramics increases the main drawback of the CaP's, which are the poor mechanical properties for load-bearing applications [6,49]. To overcome this drawback, a series of new composite materials have been synthesized and tested with the aim of obtaining a material of sufficient mechanical strength for load-bearing applications but still resorbable enough to allow a full conversion into bone tissue during bone regeneration [49].

### 2.3. MAGNESIUM AND ITS ALLOYS AS DEGRADABLE BIOMATERIALS FOR ORTHOPAEDIC APPLICATIONS

Nowadays, metal-based implants are the most common for load-bearing applications, based on their high mechanical strength and fracture toughness. Nevertheless, bone implants should have similar mechanical properties to the surrounding bone in order to guarantee bio-functionality

during the healing process; this is a drawback of the metallic biomaterials used today because most of them have higher mechanical properties than the bone, which results in a stress-shielding effect that leads to a low stimulation of the regenerated bone and to causing a decrement in the stability of the implant and surrounding tissue [7]. Additionally, the materials used for the fabrication of bone fixation tools are mainly bio-inert, requiring their removal after the bone healing. Therefore, the spot is now focussed on the development of degradable biomaterials that can replace the actual bone implants with the aim to avoid a second surgery [3].

Magnesium (Mg) and its alloys have attracted attention as potential degradable materials for bone regeneration [8,51]. Magnesium is an exceptional lightweight metal with a density of  $1.74 \text{ g}\cdot\text{cm}^{-3}$ . The fracture toughness of magnesium is higher in comparison with ceramic biomaterials such as HA or any other CaP present in the human bones, while the elastic modulus is close to that of bone, i.e. 40 GPa compared to  $\sim 20$  GPa, respectively. In addition, Mg is an important element for many essential metabolisms and is naturally found in all bone tissues, which makes it biocompatible; moreover, Mg exhibits osteoconductivity properties [8,51,52].

The main drawback of magnesium that limits its medical application is its high corrosion rate under physiological conditions, losing mechanical integrity before the tissue can be sufficiently healed. Additionally, the corrosion of Mg and its alloys (**Figure 3**) produces hydrogen at a fast rate (**Eq. 1**), which is not favourable for the host tissue and the healing process [8,51,52].

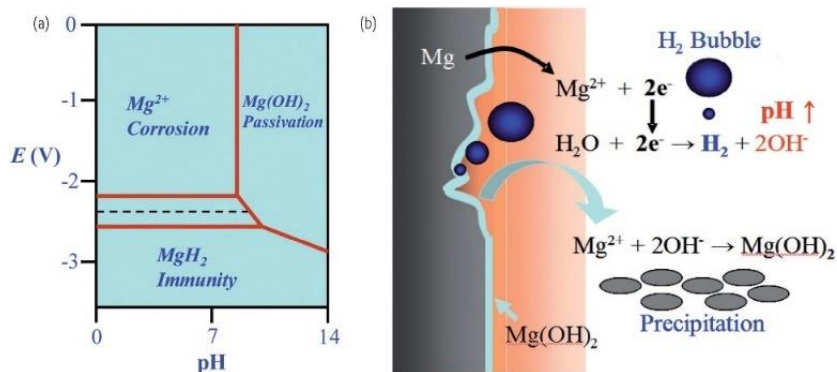
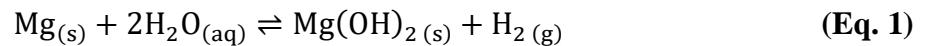


**Figure 3.** Pourbaix (potential-pH) diagram of pure Mg – H<sub>2</sub>O at 25 °C and schema of corrosion mechanism [53].

However, there are some possibilities of tailoring the corrosion rate of Mg under physiological conditions, most frequently by alloying the Mg with non-toxic elements such as calcium, manganese and zinc; or using protective coatings, usually based on calcium phosphate bioceramics [8,11,51,52].

There are three main considerations for the selection of the alloying element in degradable Mg-alloy biomaterials. The first and most important is the nontoxicity of both the alloying element and the corrosion products. The second consideration is the influence of the alloying element on the corrosion behaviour of the alloy. This factor is important when tailoring the degradation rate of the material; due to the low electrochemical potential of Mg (-2.37 V), if the alloy is not in solid solution, intermetallic phases are formed that induce the internal galvanic corrosion and decrease the corrosion resistance of the material. And the last main consideration is the effect on the mechanical properties of the alloy [11].

For the design of non-toxic Mg alloys, the chemical elements are limited to Ca, Zn, Si, Gd, Zr, Sr and Y [9,11,52,54]. The reasons are mainly based on the mechanical properties, bioactivity and degradation speed assays. Diverse investigations are focused on binary Mg alloys and their mechanical and corrosion behaviour. Calcium, zinc and rare-earth metals are the group of the most frequently studied alloying elements for Mg.

In the case of Mg-Ca alloys, calcium contributes to strengthening the alloy and acts as a grain-refining agent. Additionally, the Mg<sub>2</sub>Ca intermetallic improves the creep resistance, but a large amount of Ca, i.e. >1 wt. %, can promote problems during casting such as hot tearing or sticking [9]. For its part, Zn contributes to strengthening the Mg alloys when it is present in low concentrations and is in solid solution, i.e. >2 wt. %. Also, the addition of Zn improves the castability but in larger amounts it also leads to a brittle behaviour [9]. On the other hand, rare-earth elements can dissolve within Mg in a wide concentration, creating solid solutions with excellent mechanical strength and good degradation rate [9,55].

The diverse Mg alloys exhibit a wide range of degradation rates depending on the chemical composition and processing of the alloys. Moreover, the implantation area plays an important role: Mg-based materials degrade faster in the presence of higher vascular zones due to the higher fluid presence. In addition, the mechanical integrity is strongly connected to the final application and properties of the material [30].

To date, numerous Mg-based degradable biomaterials have been tested for bone regeneration in order to characterize their corrosion and tissue response. Some of the *in-vitro* degradation rates and the mechanical properties of binary Mg alloys are summarized in **Table 2**. Most of the investigated alloys indicate good biocompatibility after *in-vivo* tests, showing that Mg-based alloys can promote the formation of new bone around the implanted material. Additionally, the corrosion products reveal high deposition of CaP minerals, showing in some cases good contact between the implant and the adjacent bone. Nevertheless, the main drawback regarding the gas cavity presence is still observed in almost all the studies. The hydrogen production is usually higher in the initial post-implantation period and gradually decreases with time due to surface passivation of the implant [9,30].

**Table 2.** Mechanical and corrosion properties of binary Mg alloys for biodegradable implants [11,56].

Alloy	Condition	YS (MPa)	UTS (MPa)	In vitro corrosion rate (mm·year <sup>-1</sup> )	
				Weight loss	Electrochemical test (solution)
Mg	As-cast	21	-	-	-
Mg	As-extruded	90-105	-	-	-
Mg-1Ca	As-cast	40	71.38	-	12.56 (SBF)
Mg-1Al	As-cast	40	160	-	2.07 (SBF)
Mg-1Ag	As-cast	23.5	116.2	-	8.12 (SBF)
Mg-1In	As-cast	36.5	146	-	2.32 (SBF)
Mg-1Mn	As-cast	28.5	86.3	-	2.46 (SBF)
Mg-1Si	As-cast	79	194	-	6.68 (SBF)
Mg-1Sn	As-cast	35	149	-	2.45 (SBF)
Mg-1Y	As-cast	26.3	75	-	3.16 (SBF)
Mg-1Zn	As-cast	25.5	134	-	1.52 (SBF)
Mg-1Zr	As-cast	67.5	172	-	2.20 (SBF)
Mg-0.6Si	As-cast	60.11	166.2	-	0.8 (Hanks' sol.)
Mg-2Sr	As-rolled	147.3	213.3	0.37 (Hanks' sol.)	0.87 (Hanks' sol.)
Mg-6Zn	As-extruded	169.5	279.5	0.07 (SBF)	0.16 (SBF)
Mg-8Y	As-cast	156	257	-	2.17 (3.5 wt.% NaCl)
Mg-10Gd	As-cast	84.11	131.152	1.75	-
Mg-15Dy	As-cast	68.5	125	0.35 (DMEM)	-

**YS** = Yield strength; **UTS** = Ultimate tensile strength; **SBF** = Simulated body fluid; **DMEM** = Dulbecco's Modified Eagle Medium.

## 2.4. ROBOCASTING OF POROUS CONTROLLED SCAFFOLDS

New methodologies for materials fabrication have been developed lately; the additive manufacturing techniques have brought the ability to build-up three-dimensional structures following a computed pattern or design. These technologies are very useful for the manufacturing of porous scaffolds for orthopaedic applications, controlling the pore geometry and degree of porosity, which is an important factor for the vascularization process once the implants are placed inside the patient.

Due to its simplicity, robocasting, also known as direct ink writing (DIW), is one of the widely-used additive manufacturing technologies for the processing of biomaterials structures, bioceramics in particular. The technique is based on the direct extrusion of an ink, which is mainly composed of an injectable paste or slurry of the processed material. The process was developed at Sandia National Laboratories in 1997 as a method for rapid prototyping and free-forming objects with low-binder slurry following a computed design [57]. In more detail, robocasting is the robotic deposition of highly concentrated suspensions or pastes, between 50 to 65 vol.% of a powder in a solvent (typically water) with an organic additive or binder in order to provide good rheological properties, making it possible to construct a computed-design structure following a desired pattern on a layer-wise deposition [58,59]. In this process, the best ink must be able to flow through a nozzle of a desired aperture and have a shape retention capacity after the deposition [60–62]. After robocasting, the 3D object must be sintered to consolidate the powder particles and burn out the solvent and binder in order to obtain the final dense structure.

Thus, the robocasting technique allows the design and rapid fabrication of bioceramic materials in complex 3D shapes without the need for expensive tooling. Calcium phosphate structures with controlled interconnected porosity for cell seeding and promoting the bone formation have recently been produced by this technology and tested as bioactive scaffolds (**Figure 4**). They have shown excellent bioactive properties due to the microstructure and chemical composition but with the main drawback of poor mechanical properties due to the high porosity of the bodies, which in turn makes the compression strength vary from 1 MPa up to less than a hundred mega pascals, which is not suitable for load-bearing applications [63–69].

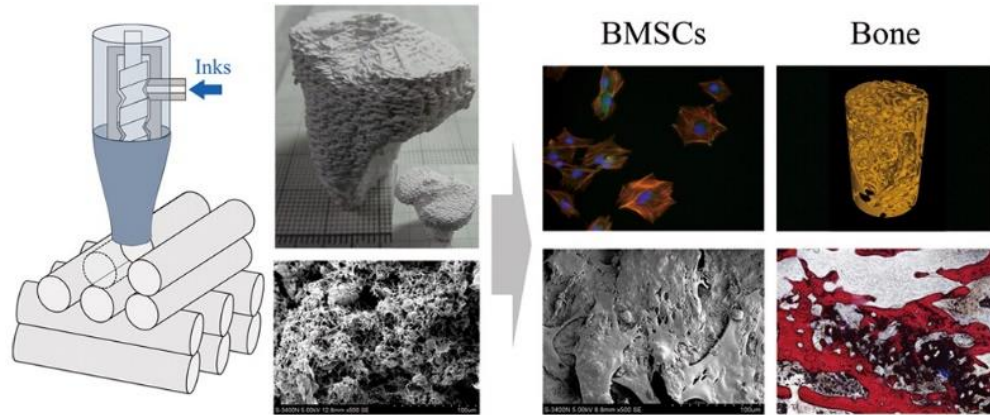


**Figure 4.** Schematic process for the robocasting manufacturing of porous scaffolds for orthopaedic applications [69].

## 2.5. LIQUID METAL INFILTRATION: MANUFACTURING OF INTERPENETRATED COMPOSITES

Liquid metal infiltration of ceramic preforms is one of the best-suited fabrication methods for the production of matrix-based graded composites with a variety of complex shapes having control over the volume fraction of the embedded materials. The metal infiltration procedure consists in a liquid-state fabrication method, in which a porous preform (usually as reinforcement) in the form of ceramic particles, fibres, or interconnected porous bodies, are embedded in a molten metal, which fills the porosity between the dispersed-phase material [16,17].

The liquid infiltration processes can be classified in two categories: i) spontaneous infiltration, and ii) forced infiltration. This classification depends on the wettability between the liquid component and the solid material to be infiltrated. Therefore, when the capillary action of the solid material acts as the driving force for the infiltration, then the process occurs spontaneously. On the other hand, when an external force such as gas pressure, mechanical pressure, squeeze, electromagnetic field, etc. is needed to make the liquid enter the pores of the solid material, then the process is considered as forced infiltration; this method is usually faster than spontaneous infiltration and, moreover, with better porosity filling [17,70].

The processing by liquid infiltration depends to a great extent on the chemical and mechanical properties of the porous body, called preform in the methodology. The depth and speed of the infiltration are dependent on the permeability coefficient of the preform. The permeability

coefficient will mainly depend on the processing parameters, the volume fraction of the preform phase and the open porosity dimensions [17].

The fabrication of interpenetrated materials can be successfully and easily performed by liquid infiltration. The interpenetrated composites can be classified according to the distribution of their phases along the volume in: i) randomly distributed or ii) well-ordered interpenetrated composites. Typically, the open porosity distribution and pore geometry are difficult to control when using free particles, fibres or porous bodies; however, with additive manufacturing, the fabrication of patterned pores is not a terminating issue when making of controlled interpenetrated composites. The advantage of each arrangement is different, depending on the application because the distribution and proportion of the materials determine the final properties of the interpenetrated composite [15].

### **2.5.1. CURRENT-ASSISTED METAL INFILTRATION (CAMI)**

The majority of infiltrated composites are made by pressure-assisted processes. The external pressure can be mechanical as in squeeze infiltration or provided by supplying a gas, which increases the pressure in the system. Some limitation for the squeeze infiltration is the melting point of the vessel that contains the molten phase – usually at a high temperature – and which should be able to contain the liquid while the infiltration takes place. On the other hand, the gas pressure method normally requires a well-sealed container [17,70]. Additionally, both methods take a relatively long time and may not be practical in many cases where the molten metals are highly reactive with the preforms or ambient atmosphere.

A novel and rapid infiltration method has lately been developed and introduced for the processing of interpenetrated composites where one of the phases, in principle metallic, is melted to fill the open porosity of a foam, which is usually ceramic-based.

The infiltration technique combines the melting of the metallic phase by an electric current flux and the mechanical pressing of the system by a set of punches in a graphite die. The design and arrangement of the initial materials are depicted in **Figure 5**.

With this approach, it is possible to minimise a potential reaction between the interpenetrated materials while assuring the filling of the porosity of the preform in a fast process.

The so-called current-activated, pressure-assisted infiltration was developed in 2013 and proved for the infiltration of  $Ti_2AlC$  foams with the 6061 aluminium alloy (AA6061) [71].

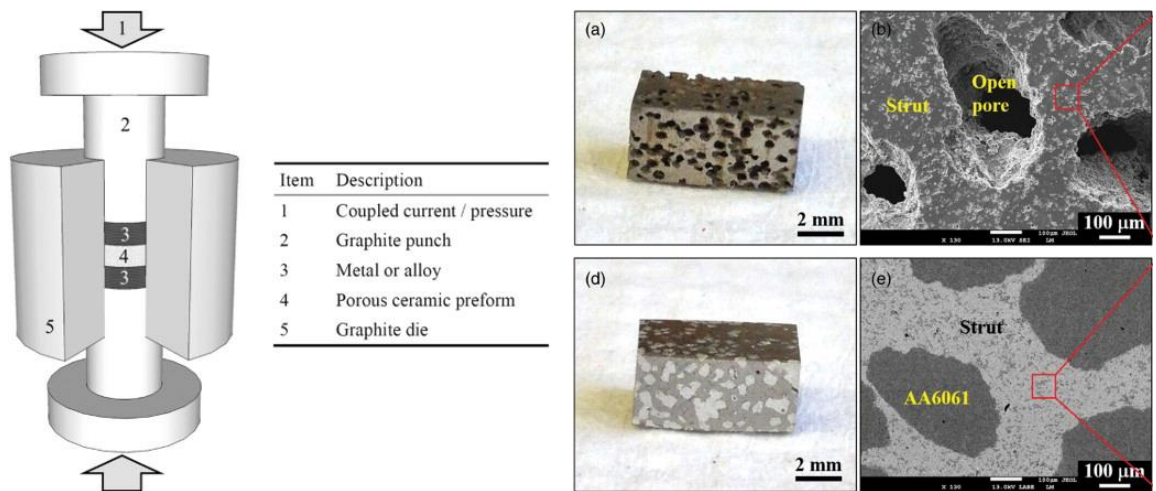


**Figure 5.** Schematic of the current-activated pressure-assisted infiltration for the production of interpenetrated ceramic-metal composites, and pictures of the resulting  $Ti_2AlC$  foams infiltrated by aluminium alloy [71].

The current-activated and pressure-assisted infiltration can be seen as an extension of the spark plasma sintering technique, as the processing happens in a graphite mould under vacuum and the heating of the powder particles is based on the Joule heating effect generated by the electrical current circuit. From this extent, the versatility of this infiltration method can be mixed with a densification or sintering process, achieving a rapid consolidation of green structures and infiltration of porous structures for the manufacturing of interpenetrated composites. In addition, the fast processing is able to co-sinter and handle highly reactive ceramic-metal composite systems [71,72].

Nevertheless, pressure-assisted methods cannot be used extensively for the infiltration of all preforms due to mechanical compressive resistance limitations, especially in ceramic foams that are very fragile. The redesign of the current-activated and pressure-assisted process was accomplished by the development of a new methodology that carries out the infiltration at the same time that the consolidation of the whole interpenetrated composite is taking place. The technique has been called current-assisted infiltration sintering (CAIS) [73] because it has the same principle of heating by the Joule-effect, so the entire process is accomplished in a few minutes.

A variant of the technique's name has been introduced, namely current-assisted metal infiltration (CAMI), considering that the sintering or consolidation happens when the infiltration process is taking place. The CAMI processing has been tested and proved for the infiltration of porous calcium-phosphate structures with molten magnesium and zinc. **Figure 6** shows the configuration and design of the graphite die for the CAMI processing and one of the interpenetrated composites consisting of a decellularized bovine bone with pure Mg [73–75].

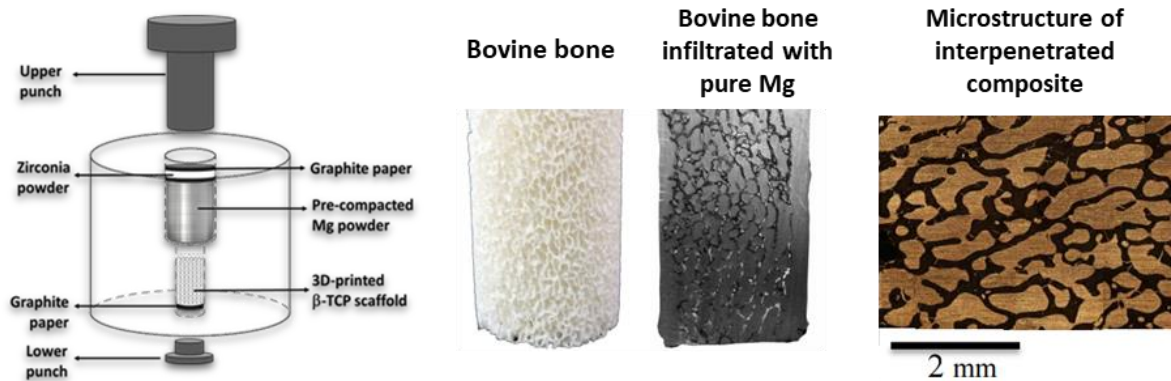


**Figure 6.** Schematic of the current-assisted metal infiltration arrangement and graphite die design to avoid the loading of fragile preform, and pictures of Mg/bovine bone before and after metal infiltration.

The design of the graphite container has a reduction area that separates the metallic phase, which is compressed between the upper punch and the reduction area, and the preform to be infiltrated, which is located under the reduction area free of any mechanical stress. In this way, the processing of brittle preforms can be performed while keeping the advantages of the fast infiltration.

## 2.6. MAGNESIUM / CALCIUM-PHOSPHATE (Mg/CaP) COMPOSITE BIOMATERIALS

A new generation of degradable biomaterials has been developed due to the need for more bioactivity and interaction of the implants with the surrounding tissues. Furthermore, the degradation behaviour is needed to avoid second surgeries, when it is necessary to remove the implants after the healing process.

In the last decade, the design and study of degradable metals and alloys became the key to the evolution of materials for biomedical applications. In this extent, magnesium (Mg) and its

alloys are potential candidates because of their similar strength to the bone tissue and biocompatibility, compared to the available metallic implants [8,9]. Nevertheless, Mg corrodes rapidly under physiological conditions, losing its integrity and mechanical properties before the healing process is finished or sufficient for mechanical loading. Thus, Mg alloys have found their application in the fabrication of stents for atrophied arteries or for screws that are not under considerable mechanical stress [3,29]. However, the desire to expand the use of Mg alloys for load-bearing applications with controlled degradation rate is ongoing.

There are three main possibilities of improving or adjusting the degradation rate of Mg inside the human body: i) using alloying elements, ii) surface treatment such as oxidation or protective bioactive coatings, and iii) developing metal matrix composites (MMCs) [76]. The last approach offers the advantage that Mg composites can provide a combination of exceptional characteristics, including controlled degradability and adjustable mechanical properties, which can appear close to the bone tissue, depending on the chemical composition of the composite, processing, and distribution of the present phases.

Recent findings have proved that the addition of ceramic reinforcement into Mg or its alloys can enhance the mechanical properties and corrosion resistance of the composites, compared to the bare metal. The most promising composites are based on reinforcing bioceramic phases, of particular interest are the family of calcium phosphates (CaP's) due to their high bioactive properties and possible bioresorption [6].

Therefore, extensive investigations have been focussed on composites based on pure Mg or Mg alloys containing diverse quantities of calcium, zinc, and rare-earth elements in combination with various CaP's such as hydroxyapatite (HA), calcium polyphosphate (CPP),  $\beta$ -tricalcium phosphate ( $\beta$ -TCP) or their combination produced by different manufacturing processes, which mostly include powder metallurgy, stirred casting method, or liquid infiltration of porous preforms [77].

A compilation of the state of the art of the Mg/CaP composite biomaterials is presented in **Annex 1**; the list reports the mechanical properties, corrosion rate, and biocompatibility registered for each material investigated until now, comparing them with the natural bone properties and with some biomaterials used nowadays for the manufacturing of implants.

### **2.6.1. MECHANICAL PROPERTIES OF Mg/CaP COMPOSITES**

It has been reported that the addition of CaP generally improves the mechanical properties of Mg alloys. The amount, size, shape, and distribution of the CaP reinforcements in Mg-based composites are of main importance to the mechanical performance of the final composites. The CaP ceramics are in general hard and brittle and thus the Mg/CaP composites exhibit higher compression strength but reduced tensile strength and elongation compared with the pure Mg-based phases [51]. Mechanical properties of the composites are similar to those of the natural bone tissues and good enough for orthopaedic applications. In particular, the elastic modulus is much closer to that of the natural tissue compared to any other metallic implant used nowadays in orthopaedics, which is an important feature from a biomechanics point of view since it helps to avoid stress shielding of the bone tissue to be regenerated.

The final mechanical response is highly dependent on the distribution of the ceramic phase in the composite. An inhomogeneous distribution produces locally different mechanical properties, resulting in stress concentrators that can fail easily [4].

Diverse studies conclude that a higher concentration of reinforcement particles can increase the agglomeration of these particles, causing a deterioration of the yield and ultimate strengths, particularly in tension. This effect is explained by the premise that agglomeration forms pores and defects in the volume of the composite [77].

Moreover, a higher concentration of free ceramic particles involves less consolidation of the material volume, decreasing the properties when the particles agglomerate. However, a correct processing of the Mg/CaP composites can assure a good mixing efficiency, resulting in better mechanical properties. In general, the tendency shows that Mg/CaP composites containing less than 20 wt. % homogeneously distributed ceramic phase are better due to their more reliable mechanical properties [51].

In addition, a comparison of the results of the processing of composites reveals that it has a significant effect on the mechanical properties of the final material. In this respect, the same Mg-based composites containing HA particles exhibit different mechanical properties when the material is processed by the casting and extrusion routes [5] or by the powder metallurgy route, which consists of mechanical mixing and/or extrusion consolidation [78]. The mechanical

properties of Mg/HA composites processed by powder metallurgy revealed a better mechanical performance even when they had lower density, which was related to a better homogeneous distribution of the phases. It has been reported that a post-treatment such as hot extrusion or subsequent heat treatment might improve the mechanical properties of the composites [79].

Another important factor in the mechanical response of the Mg/CaP composites is related to the effect of the addition of ceramic particles on the final Mg phase microstructure. Then, the effect of refining the grain size leads to higher compression strength and better corrosion resistance [77,80].

Another approach in the fabrication of Mg/CaP composites is the infiltration of ceramic preforms with molten Mg or its alloys. This process allows a reticulated dispersion of the CaP and can be varied by the architecture of the initial preform or scaffold. On the one hand, this process avoids the problem of particle agglomeration. On the other hand, it presents some concerns such as the chemical decomposition of the CaP promoted by the molten alloy or the limited wettability of the preforms leading to incomplete infiltration of the cavities [77].

The findings obtained for infiltrated CaP scaffolds with Mg alloys such as the Mg-Ca/HA-TCP composites revealed higher strength and elongation behaviour in comparison with the original scaffolds but inferior mechanical properties than in the pure metal phase. These lower properties can be attributed to the low interfacial bonding strength, which was found to be lower for the HA-based composites than for the  $\beta$ -TCP ones [81–83].

In general, the majority of the Mg/CaP composites exhibit similar mechanical properties. Individual variances depend on the chemical composition, concentration and homogeneous distribution of the phases as a result arising from the material processing.

### **2.6.2. CORROSION BEHAVIOUR OF Mg/CaP COMPOSITES**

The corrosion resistance of Mg/CaP composites could be either better or worse than that of the pure metal, depending on the distribution of the phases and the consolidation of the ceramic phase that can act as a channel increasing the surface area for the Mg phase to be corroded. Moreover, the CaP particles together with the processing route can produce a grain-refining effect in the Mg phase and thus provide good corrosion resistance [77].

It was found that HA particles generally stabilise the corrosion rate of Mg alloys, resulting in a more uniform corrosion attack due to the formation of a uniform passivation layer [4]. The corrosion of Mg was increased by larger amounts of the ceramic phase because of the increment in the galvanic coupling as a result of the decomposition of the CaP and the precipitation of intermetallic phases that act as anodic sites. In addition, an increase in the ceramic amount can lead to an agglomeration of particles, which is related to lower densification, an effect that reduces the corrosion behaviour [51,84].

The microstructure and porosity of the composites are the main factors controlling the corrosion rate. Thus, the addition of alloying elements and the used of manufacturing technologies that enhance a refined and dense microstructure are highly desirable in order to achieve the best corrosion resistance of the final composites [5,78].

In the case of interpenetrated Mg/CaP composites, the materials exhibit superior corrosion resistance due to the metal infiltration method and the distribution of the phases in the composite. This effect is increased when the bonding between the bioceramic and the metallic phases is good enough to avoid the channel infiltration of corroding liquid in the Mg matrix [83]. Thus, the porous  $\beta$ -TCP preforms have better attachment to the Mg alloy phase than the HA ones have, resulting in better corrosion resistance [81,82]. Nevertheless, all the infiltrated composites tend to form a protective layer along all the sample surface due to the activity of the CaP, which promotes the deposition of more calcium- and phosphorus-based compounds [4,77,85].

Special attention must be given to the chemical interaction between the Mg alloys and the CaP's in order to keep a good corrosion behaviour. Agglomeration must be avoided and therefore a high content of ceramic free particles is not suitable. Additionally, possible reaction between the materials results in the formation of intermetallic phases due to the calcium migration from the phosphates to the metal phase [86].

In general, the results for the corrosion behaviour of Mg/CaP composites published by different researchers cannot be properly compared due to the different conditions used in the evaluation. Consequently, it is not possible to determine what the best materials are. However, it can be concluded that the addition of CaP's in Mg-based volumes together with proper processing techniques for obtaining refined grains improve the corrosion resistance of the composites.

### 2.6.3. BIOCOMPATIBILITY OF Mg/CaP COMPOSITES

In terms of the biocompatibility behaviour, the Mg/CaP composites exhibit controversial responses under *in-vitro* and *in-vivo* tests. The failure of the biological response depends greatly on the fast degradation of the Mg, which increases the pH by the production of magnesium hydroxide and gaseous H<sub>2</sub>, which in turn promotes an inflammation of the surrounding tissue and makes the regeneration and healing process more difficult. On the other hand, the chemical properties of the CaP's ensure the bioactivity with the bone tissue.

The addition of HA in Mg is of good influence on the cytotoxicity properties by lowering the pH increment and enhancing the cell viability compared to the bare Mg alloys, tested in contact with different types of cell [4]. Moreover, all the studies have proved that the presence of CaP bioceramics promotes the deposition of apatite on the surface of Mg/CaP composites. This apatite formation increases the cell adhesion and bioactivity response [77,83,86].

Also, the antibacterial property of Mg alloys is a positive effect due to the local pH increment. This response is highly valuable in clinical applications since infections associated with the surgical procedures are a serious issue after the implantation of any kind of material in the human body [51,87].

On the other hand, some other composites have shown some degree of cytotoxicity due to the corrosion products formed in interaction with simulated body fluid environment after the immersion tests [88]. Nevertheless, controlled degradation rates allow the human body to reabsorb these corrosion products. Besides, as the human body is an active environment in motion, the release of these products can be easily managed and the localised pH changes dealt with in order to avoid some degree of cytotoxicity in the surrounding tissue.

Based on the contradictory results concerning the biocompatibility of the Mg/CaP composites, more *in vitro* and *in vivo* tests are necessary to provide a complete evaluation of this kind of degradable biomaterials, and at the same time a uniform methodology must be set to carry out a reliable *in vitro* test to predict the possible *in vivo* behaviour [51].

## **2.7 REMARKS ABOUT Mg/CaP COMPOSITES**

Degradable composites made up of various Mg alloys and bioceramics with different fabrication routes have been extensively investigated to assess their viability in biomedical applications.

Biomaterials with similar characteristics to the bone characteristics are very promising for hard tissue engineering applications. The CaP ceramics induce adsorption of ions and deposition of apatite mineral on the surface of the material, stimulating bone regeneration and growth. However, the degradation rate should match the bone-tissue healing. Therefore, the degradable biomaterial needs to be tailored according to a given application.

The selection of the chemical composition of composites needs to be based on the improvement of mechanical and corrosion resistance properties without sacrificing the biocompatibility of the material. Additionally, the processing of the composites plays an important role in the resulting properties. Thus different arrangements and techniques for the manufacturing of Mg/CaP systems and their full evaluation are still needed for the fabrication of degradable and bioactive devices dedicated to bone healing.

### 3. AIMS OF THE THESIS

The doctoral thesis is focused on the design and manufacture of interpenetrated magnesium/calcium-phosphate composites and their wide characterization as potential degradable biomaterials for orthopaedics.

In the study, hydroxyapatite, calcium-deficient hydroxyapatite and  $\beta$ -tricalcium phosphate were used for the fabrication of porous preforms by means of the robocasting technique in order to obtain a precise control of the porosity degree and pore geometry. The consolidated preforms were infiltrated with ultra-high pure Mg and Mg-X alloys (X = 0.2 wt. % Ca and 1 wt. % Zn) using the newly developed current-assisted metal infiltration (CAMI) technique.

The Mg/CaP interpenetrated composites were evaluated in terms of their microstructure, chemical composition, volumetric phase distribution, mechanical behaviour under compression, degradation behaviour in simulated physiological conditions, and *in vitro* test response.

The dissertation aim was accomplished fulfilling specific objectives linked to the following activities:

- Synthesis and processing of hydroxyapatite and tricalcium phosphate powders *via* soft chemistry routes and high-temperature treatment.
- Manufacture of controlled-porous scaffolds (preforms) using the robocasting technique.
- Consolidation and infiltration of bioceramic scaffolds with magnesium and magnesium alloys (containing calcium and zinc) using the current-assisted metal infiltration technique.
- Characterization of obtained interpenetrated composites using micro-computed tomography, X-ray diffraction and metallography observation by optical and scanning electron microscopy techniques.
- Evaluation of the mechanical properties by compression test of the produced Mg/CaP composites.
- Evaluation of the degradation rates under simulated physiological conditions of the produced Mg/CaP composites.
- Evaluation of the cytotoxicity response of the produced Mg/CaP composites.

## 4. MATERIALS AND METHODS

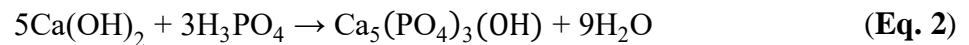
The dissertation topic aimed at the manufacture and verification of degradable properties of interpenetrated composites based on Mg alloys and CaP for bone replacement applications was divided into several activities and tests in the frame of the four subsequent stages: (i) synthesis of CaP and robocasting of controlled porous scaffolds; (ii) casting and measurement of corrosion behaviour of Mg alloys containing low amounts of calcium and zinc; (iii) infiltration of CaP scaffolds with pure Mg or Mg alloys using the CAMI technique; and (iv) physicochemical characterization of the composites produced and their mechanical and biocompatibility testing.

### 4.1. SYNTHESIS OF CALCIUM PHOSPHATES (CAP'S) AND PRODUCTION OF CONTROLLED POROUS SCAFFOLDS

#### 4.1.1. SYNTHESIS OF HA AND $\beta$ -TCP POWDERS

Hydroxyapatite powder was synthesised through a chemical precipitation reaction between phosphoric acid and calcium hydroxide at room temperature. This method has been widely studied for obtaining HA nano-particles [6]. The HA precipitation method has the advantage of being low-cost due to the cheap precursors and easy preparation process.

The synthesis follows the reaction:

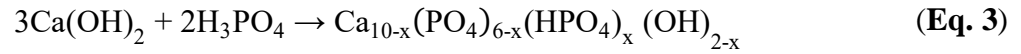


Initial solutions with each reactant in 1 M concentration were mixed by adding dropwise the phosphoric acid into the calcium hydroxide solution until reaching a pH of ~8.5. The stirring of the solution was kept for 1 hour to promote the precipitation of the HA particles. The final product was rinsed with distilled water three times and dried in a furnace at 100 °C for 4 hours in ambient atmosphere. Finally, the powder was calcined at 800 °C for 2 hours to ensure its crystallization.

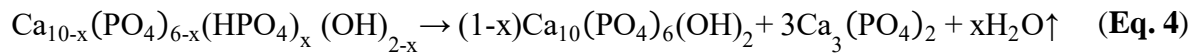
In the same way, the  $\beta$ -TCP powder was synthesised. The synthesis consisted in the precipitation of CDHA with a Ca/P atomic ratio of close to 1.5, which leads to the stoichiometry of the tricalcium phosphate. Several conditions were tested varying the Ca/P ratio, calcination treatment, and pH of the reaction solution.

The powders obtained were evaluated by X-ray diffraction to assure the chemical purity of the final product and establish the best conditions of the synthesis.

The reaction followed the chemical equation:



The calcium-deficient HA decomposes at temperatures above 800 °C to produce TCP; the decomposition reaction depends on the nature of the CDHA and can but need not be completed by the following reaction [46,89]:



#### 4.1.2. SYNTHESIS OF CALCIUM-DEFICIENT HYDROXYAPATITE BY HYDRATION OF $\alpha$ -TCP

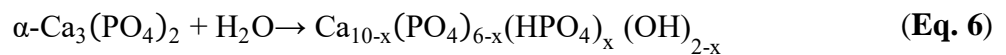
For the synthesis of calcium-deficient hydroxyapatite (CDHA), tricalcium phosphate in its monoclinic phase ( $\alpha$ -TCP) was produced by the high-temperature solid-state reaction between calcium carbonate and calcium hydrogen phosphate at 1400 °C. The method consists in mixing the solid precursor powders and heating them in a furnace at 1400 °C for 2 hours, where a high-temperature solid-state reaction (**Eq. 5**) takes place, followed by a rapid cooling down that maintains the  $\alpha$ -TCP polymorph metastable at room temperature.

Using a vibration disc mill (RETSCH, Germany), the product of the solid-state reaction was milled at 1000 rpm for 100 seconds in order to obtain a fine powder with a particle size below 36  $\mu\text{m}$ , which is the useful size for the preparation of ceramic pastes for robocasting.

The solid reaction for the production of  $\alpha$ -TCP is as follows:



The obtained  $\alpha$ -TCP powder hydrates under a humid atmosphere (~37 °C) to precipitate calcium-deficient hydroxyapatite crystals following the chemical reaction:



where  $x$  is between 0 and 1, keeping an elemental Ca/P ratio of between 1.67 and 1.5.

#### 4.1.3. DIRECT INK WRITING OF CALCIUM-PHOSPHATE INJECTABLE PASTES

The robocasting technique is a bottom-up computer-controlled fabrication process. A slurry, made from any kind of material in the shape of refined powder, is printed through a thin tip of a syringe following a set pattern. The robocasting process allows a good control of the dimensional tolerances (lower than 100 microns) and ensures almost 100% reproducibility of the 3D-printed structures. In the present work, a set of macro-porous cylindrical structures were produced by robocasting injectable bioceramics. At the beginning, four different pore sizes were used to determine a favourable pore size for the infiltration of the scaffolds with pure Mg by the current-assisted metal infiltration method.

Injectable paste of commercial  $\beta$ -tricalcium phosphate (VWR, Belgium) was obtained by mixing the commercial powder with a 40 wt. % Pluronic F-127 (Sigma-Aldrich, Germany) solution in distilled water. A liquid-to-powder ratio was set at 0.6 gram of Pluronic solution per each gram of commercial  $\beta$ -TCP powder.

The produced paste was introduced in a 3-mL cartridge set (Optimum® syringe barrels, Nordson EFD, USA) and placed in a 3D-printer (Pastecaster, Fundació CIM, Spain) for the robocasting of *in silico*-designed porous cylinders of 7.5 mm in diameter and 15 mm in height at atmospheric conditions. The deposition speed of the ceramic pastes was set at 8 mm·min<sup>-1</sup> using a tapered dispensing tip (SmoothFlow Tapered Tips, Nordson EFD, USA) with a nominal aperture of 250  $\mu$ m.

The initial porous cylinders were produced with nominal pore sizes of 150, 350, 500 and 1000  $\mu$ m. The macro-pores were homogeneously formed by the distance between adjacent ceramic strands, which were deposited in an orthogonal pattern, forming a parallel grid that was maintained through the whole longitudinal axis of the cylinders. The overlapping between layers was set at 5 % of the strand diameter. Once the cylinders were finished, they were dried at room temperature for 24 h and sintered at 1100 °C for 5 h, with a heating ramp of 2.5 °C·min<sup>-1</sup> inside a conventional furnace (LH30/13, LAC, Czech Republic).

After the molten-Mg infiltration of the different-pore-size cylinders by the CAMI technique, the effect of the pore size on the infiltration success was evaluated. After this preliminary analysis, the fabrication of injectable pastes from synthesised HA,  $\beta$ -TCP and  $\alpha$ -TCP powders was

carried out for the robocasting of porous cylindrical scaffolds of 10 mm in diameter and 10 mm in height with a macro-pore size of  $\sim 500$   $\mu\text{m}$ . The printing parameters and conditions were kept the same as for the initial scaffolds with the exception of using a tapered tip of a nominal aperture size of 410  $\mu\text{m}$ .

Finally, for the sintering of HA and  $\beta$ -TCP scaffolds, the sintering conditions were set at 1200  $^{\circ}\text{C}$  for 5 h. For the consolidation (hardening) of CDHA scaffolds, the hydration reaction of the  $\alpha$ -TCP scaffolds was carried out by storing the robocast structures at 37  $^{\circ}\text{C}$  in 100% humid atmosphere for 24 h and afterwards immersed in distilled water at 37  $^{\circ}\text{C}$  for 6 days to complete the hydrolysis of the TCP polymorph into calcium-deficient hydroxyapatite (**Eq. 6**).

All the CaP scaffolds obtained were stored for further infiltration by pure Mg and Mg alloys. Representative samples were characterized by means of X-ray diffraction (XRD; Rigaku SmartLab 3kW) using Cu  $K\alpha$  radiation, and scanning electron microscopy (SEM; LYRA3 XMU, TESCAN) on samples coated with a thin carbon layer to prevent charging during observation. Additionally, the mechanical response in compression was evaluated.

#### **4.2. MANUFACTURING BY INDIRECT CHILL CASTING OF Mg ALLOYS**

Ultra-high purity magnesium was used for the production of two degradable Mg alloys by the indirect chill casting method. Firstly, blocks of pure Mg were melted at 670  $^{\circ}\text{C}$  using an electronic resistance furnace under a protective atmosphere of Ar with 2 vol. % of  $\text{SF}_6$ . With the melting of Mg blocks completed, preweighed pellets of calcium (Ca, 1-cm pellets, 99 %, Alfa Aesar) or zinc (Zn, 1-cm pellets, 99.9 %, Alfa Aesar) were added to the molten Mg at a temperature of 750  $^{\circ}\text{C}$  in order to produce single-phase binary Mg alloys containing calcium or zinc below their solubility limits. The liquid system was manually mixed for 5 minutes. After that, the steel crucible with the molten alloy was taken out of the furnace and cooled down by a slow immersion into a bucket with water at room temperature.

The nominal calcium content for the Mg-Ca alloys was set at 0.2, 0.4, 0.6 and 0.8. wt. %, while for the Mg-Zn alloys, the nominal content of zinc was 1, 2 and 3 wt. %. The final ingots were machined into cylinders of 10 cm in diameter and 15 cm in length. The cylinders were annealed at

400 °C for 2 h and hot-extruded at 300 °C to obtain bars of 1 cm in diameter, using a ram speed of 0.6 mm·s<sup>-1</sup>.

The chemical composition of the alloys was determined by X-ray fluorescence (Spectrolab M9, Spectro-Ametek-Klave, Germany) and in the case of the calcium concentration, it was estimated by atomic absorption spectroscopy. Finally, the degradation behaviour of as-extruded alloys was evaluated in simulated body fluid (SBF) at 37 °C. From the results, the best two corrosion resistant alloys were selected for the infiltration of the CaP scaffolds.

#### **4.3. MAGNESIUM INFILTRATION OF CaP SCAFFOLDS BY CURRENT-ASSISTED METAL INFILTRATION (CAMI)**

Robocast CaP scaffolds were used as preforms for the liquid metal infiltration with pure Mg, Mg alloy containing 0.2 wt. % of Ca, and Mg alloy with 1 wt. % of Zn (alloys that revealed the best corrosion resistance) by means of the CAMI technique. Mg and Mg alloys discs of 10 mm in diameter and 10 mm in height were used for the infiltration of CaP preforms.

The special designed container for CAMI consisted of a graphite die with 50 mm in external diameter and 50 mm in length. The top part of the die was of an inner diameter of 20 mm, where the metallic magnesium disc was placed, and the bottom part was of an inner diameter of 10 mm, where the 3D-printed TCP preform was located prior to the infiltration. For the infiltration, the bottom aperture of the die was sealed using a graphite lid that works as a stand for the bioceramic preform and as a bottom punch closing the electrical current circuit of the system. The top part was sealed with a protruded punch of 20 mm in diameter. **Figure 7** shows the design of the CAMI die and the initial arrangement of the preform and metallic disc for carrying out the infiltration process for the manufacturing of the interpenetrated Mg/CaP composites.

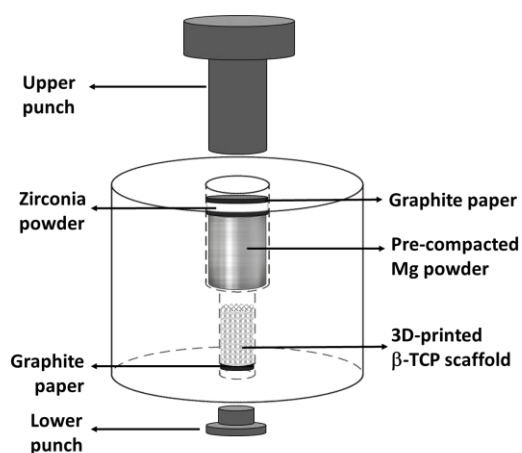


**Figure 7.** Graphite-die design and initial arrangement for the current-assisted metal infiltration technique.

Using the designed die for CAMI in the above-mentioned arrangement, the infiltration of magnesium was performed in a spark plasma sintering apparatus (SPS, Dr. Sinter 1050, Japan). The use of zirconia powder or any other type of insulation ceramic was needed to avoid overheating in the upper part of the Mg-based pellet. The effect of overheating has previously been reported for the extrusion of metallic samples by the spark plasma extrusion technique [73,90]; this is the reason of using an insulation layer, which would avoid the melting of the Mg and consequently its pouring out of the graphite die.

After placing the die set into the equipment, the electrical circuit was closed applying a constant mechanical load of 1 kN. Due to the design of the die, the mechanical load was supported by the graphite die and the Mg body and not by the bioceramic preform. Then, the melting of magnesium and the infiltration were achieved by heating up the die, reaching a temperature of 670 °C with a heating ramp of 100 °C·min<sup>-1</sup>, followed by one minute of dwell time under vacuum. The heating was done by applying a direct electrical current discharge at on-off cycles of 12 and 2 ms, respectively. The final cylindrical samples after CAMI had the dimensions of 10 mm in diameter and of approximately 20 mm in height.

The set of interpenetrated Mg/CaP composite samples is listed in **Table 3**. The specimens were machined and prepared for their physicochemical characterization, their mechanical and degradation behaviour, and their cytotoxicity response, considering for each evaluation an appropriate number of samples for statistical analyses.

**Table 3.** Number of interpenetrated Mg/CaP composites produced by the infiltration of CaP preforms with pure Mg and Mg alloys.

Bioceramic preform	Infiltrating alloy		
	Pure Mg	Mg-0.2%Ca	Mg-1%Zn
HA	15	15	-
CDHA	15	15	15
$\beta$ -TCP	15	15	-

#### 4.4. CHARACTERIZATION OF Mg ALLOYS AND Mg/CaP INTERPENETRATED COMPOSITES

The physicochemical characterization of pure alloys and interpenetrated composites was performed using micro-computed tomography ( $\mu$ CT), optical microscopy (OM), scanning electron microscopy (SEM) and X-ray diffraction (XRD).

Regarding the mechanical properties of the Mg/CaP composites, the compressive strength, yield strength and maximum strain of the materials at the uniaxial compression test were measured.

The degradation kinetics were assayed using a conventional simulated body fluid (c-SBF, composition and preparation procedure are in **Annex 3**) for 2 weeks at 37 °C. Similarly, the toxicity of the final materials was analysed during the first 6 days.

##### 4.4.1. PHYSICOCHEMICAL CHARACTERIZATION

For the microstructural analyses and phase composition characterization, samples were longitudinally cut and ground down, using 4000-grit SiC sandpaper.

The crystalline phase composition identification was carried out by X-ray diffraction (XRD, Rigaku SmartLab 3 kW). Scans were performed in the Bragg-Brentano geometry between 10° and 90° with a scan speed of 4 °.min<sup>-1</sup>, using Cu-K $\alpha$  radiation ( $\lambda = 0.154$  nm) at a voltage of 40 kV and a current of 30 mA.

The cross sections of the composites and pure metals were prepared for metallographic observation. A 0.25- $\mu$ m particle-size diamond suspension was used for the ultimate polishing step. Microstructures were revealed with picral solution (1.5 g of picric acid, 25 mL of ethanol, 5 mL of acetic acid and 10 mL of distilled water) and observed using optical microscopy (Olympus 8500) and scanning electron microscopy (SEM; TESCAN Lyra3). The SEM was equipped with an energy dispersive X-ray (EDX) spectroscope (INCA, Oxford Instruments, UK) for local chemical analysis

measurements. Representative images were obtained using an electron beam voltage of 5 kV on coated samples with a thin carbon layer to prevent charging during the SEM observation. In addition, EDX analysis was performed on different compounds to determine the ratio and distribution of the elements and track possible atomic diffusion between phases.

The three-dimensional architecture of the preforms was analysed by X-ray micro computed tomography ( $\mu$ -CT; GE phoenix v|tome|x L 240 system) at a voltage of 80 kV and a current of 150  $\mu$ A, using an aluminium filter. The isotropic linear voxel size (voxel resolution) of obtained volume was  $\sim 25$   $\mu$ m. A tomographic reconstruction of the samples was performed with the GE phoenix datos|x 2.0 software. Visualization of the samples and structural parameters quantifications were performed using the VG Studio MAX 3.1 software. A cylindrical region of interest that fitted the external diameter of each scaffold was created using the Chebyshev algorithm. A surface determination tool was used to determine the volumetric percentage of each phase in the composites, i.e. metal, ceramic and air (pores), together with their distribution. Finally, the efficiency of the infiltration was calculated and expressed in percentage, using (Eq. 7).

$$\% \text{ infiltration} = \frac{V_{Met}}{V_{Air} + V_{Met}} \times 100 \quad (\text{Eq. 7})$$

where,  $V_{Air}$  is the volume of pores in the composite after the infiltration and  $V_{Met}$  is the volume of metal in the composite after the infiltration.

The density of all processed materials was evaluated using helium pycnometry (Micromeritics AccuPyc II 1340).

#### 4.4.2. MECHANICAL PROPERTIES

The uniaxial compression test was performed at room temperature using a universal testing machine (Zwick/Roell Z010, USA) at a strain rate of  $0.5 \text{ mm} \cdot \text{min}^{-1}$ . The samples were machined in the shape of cylinders of 8 mm in diameter and 16 mm in length to meet the requirement of the E8/E8M-09 ASTM standard for ductile materials.

The engineering stress was calculated by dividing the load supported by the sample per the effective cross section area. Compressive yield strength ( $\sigma_y$ ) was determined at 0.2% of deformation. Compressive strength ( $\sigma_{max}$ ) was established as the maximum stress supported by the

sample before the failure, and the Young modulus (E) under compression was determined using the equation from the least-squares regression line from the steepest portion of the stress-strain curves. At least four samples of each material were used for testing and a statistical analysis was done to report the standard deviations.

Finally, the morphology of the samples' fracture surface was examined by means of SEM to obtain data for the fracture mechanism analysis.

#### **4.4.3. DEGRADATION ASSESSMENT UNDER SIMULATED PHYSIOLOGICAL CONDITIONS**

In order to determine the best alloy in terms of corrosion resistance, the corrosion rate of the initial Mg alloys was evaluated by 3 different methods: mass loss, H<sub>2</sub> evolution, and potentiodynamic measurements.

Small discs of each alloy of 10 mm in diameter and 3 mm in height were used. The discs were polished down, using #2400 SiC paper, cleaned with isopropanol and dried in air. For all the analyses, the c-SBF solution at 37 °C was used.

For the mass loss measurements, the discs were immersed in the SBF solution, keeping a sample surface-to-volume ratio of 9 mm<sup>2</sup>·mL<sup>-1</sup>. The degradation of each alloy was monitored by means of immersion tests after 1, 2 and 4 weeks. At each time, the corrosion products formed were removed by treating the corroded disc with chromic oxide and silver nitrate solution according to ISO 8407:2009(E). The weight change was registered and the degradation rate (DR) was calculated in mm·year<sup>-1</sup>, using the following equation:

$$DR = 8.76 \times 10^4 \frac{\Delta W}{S \cdot \tau \cdot \rho} \quad (\text{Eq. 8})$$

where  $\Delta W$  is the weight change in grams after the immersion time;  $S$  is the surface area of the sample in cm<sup>2</sup>,  $\tau$  is the immersion time in hours, and  $\rho$  is the bulk density of the specimens in g·cm<sup>-3</sup>.

#### 4.4.3.1. H<sub>2</sub> EVOLUTION ASSESSMENT

The corrosion rate of Mg alloys and interpenetrated Mg/CaP composites was also monitored by the hydrogen (H<sub>2</sub>) evolution test at a constant temperature of 37 °C. A set of three disc specimens of ~8 mm in diameter and ~3 mm in height of each material were immersed separately in 500 mL of c-SBF solution. The volume of H<sub>2</sub>-gas produced by the anodic dissolution of Mg was monitored during 14 days and the average corrosion rate was calculated using the following equation:

$$CR_H = 2.088 V_H \quad (\text{Eq. 9})$$

where  $CR_H$  is the instantaneous corrosion rate from hydrogen evolution, expressed in mm·year<sup>-1</sup>, and  $V_H$  is the volume of hydrogen gas produced per unit of surface area exposed to the c-SBF per time of reaction (mL·cm<sup>-2</sup>·day<sup>-1</sup>). At the end of the degradation test, the specimens were characterized via SEM and XRD in order to investigate the morphology and composition of the solid corrosion products.

#### 4.4.3.2. TAFEL EXTRAPOLATION OF POLARIZATION CURVES

A potentiodynamic polarization test for the Mg alloys and composites was conducted in SBF solution at room temperature. A three-electrode configuration was used, in which the sample was the working electrode. An Ag/AgCl electrode (3M KCl) was taken as the reference electrode and a graphite rod as the counter electrode. The polarization scan, performed with a Potentiostat/Galvanostat device (PGSTAT128N, Autolab), started immediately after the immersion of the sample from -2.0 to -1.0 V vs. Ag/AgCl at a scan rate of 5 mV·s<sup>-1</sup>. In all the cases, the sample surface exposed to the SBF was 0.2 cm<sup>2</sup> and the volume of SBF solution was 5 mL. The corrosion current density ( $j_{corr}$ ) was estimated by the Tafel slope analysis according to the ASTM G102-89 standard. The corrosion rate from the polarization test ( $CR_p$ ) was calculated according to Faraday's law (Eq. 10).

$$CR_p = \frac{c W_A j_{corr}}{n F \rho} \quad (\text{Eq. 10})$$

where  $W_A$  is the atomic weight of Mg (24.305 g·mol<sup>-1</sup>),  $n$  is the number of exchanged electrons during the anodic electrochemical reaction,  $F$  is Faraday's constant,  $\rho$  is the density of pure Mg (1.74 g·cm<sup>-3</sup> at 20 °C), and  $c$  is the conversion factor.

#### 4.5. BIOCOMPATIBILITY EVALUATION

Two different cell culture tests were carried out to evaluate the viability/cytotoxicity of the degradable materials produced.

The first test was used to classify the proliferation effect that the processed Mg alloys produced on backbone cells extracted from new-born mice. Discs of 10 mm in diameter and 2 mm in height of pure Mg, Mg-0.2%Ca, Mg-0.8%Ca, Mg-1%Zn, and Mg-3%Zn alloys were manually ground using 1200-grit sandpaper prior to the test. The samples were cleaned with isopropyl alcohol and washed with phosphate buffer solution (PBS), after which the discs were sterilised under UV-light for half an hour prior to the assay. The samples were placed inside a 24-well plate for triplicates and then immersed in Dulbecco's Modified Eagle's medium (DMEM) supplemented with foetal bovine serum (FBS, 10 vol. %), penicillin/streptomycin (1 vol. %) and L-glutamine (1 vol. %), in 5 % CO<sub>2</sub> humidified atmosphere at 37 °C for 2 hours. After that, the mice cells were seeded directly on the surface of the Mg-based samples in a concentration of 2.5x10<sup>4</sup> cells per well. The counting of the cells was carried out using a Burker chamber every 24 h up to 96 h after the initial time to evaluate the proliferation or cytotoxic effect of the alloys.

After the evaluation and selection of the Mg alloys in terms of their degradation behaviour and cell viability, the final processed interpenetrated Mg/CaP composites were submitted to an indirect cell culture test, using SAOS-2 human osteosarcoma cells cultured with Dulbecco's Modified Eagle's medium (DMEM) supplemented with foetal bovine serum (FBS, 10 vol. %), penicillin/streptomycin (1 vol. %) and L-glutamine (1 vol. %), in a 5 % CO<sub>2</sub> humidified atmosphere at 37 °C.

The indirect test means that the cells were not on the surface of the material but the material laid on them and had a direct contact with the cells adhering to the well.

The cells were seeded in 96-well culture plates at a density of 8x10<sup>3</sup> cells per well and left to attach for 24 h. After that, the wells were washed twice with PBS solution to remove the non-

attached cells, and 1 mL of cell culture medium was added. Immediately after that, one sterile sample (disc of 8 mm in diameter and 2 mm in height) was placed in the centre of each well. Prior to the study, all samples were sterilized inside ethanol (70 % in water) for 30 minutes and rinsed three times with PBS solution. Tissue culture-grade polystyrene (TCPS) was used as reference material.

The viability/cytotoxicity effect was determined by counting the nuclei of cells from recorded pictures of whole wells and analysed by the ImageJ software during the first 6 days of the experiment.

In the same way, the cell metabolic activity (LDH) was evaluated after 3 and 6 days of indirect culture using an XTT cell proliferation assay kit (American Type Culture Collection) according to the supplier instructions. Prior to the XTT assay, the samples were removed and the cells were rinsed twice with PBS solution.

The alkaline phosphatase (ALP) activity was determined on the same samples as those used for the cell metabolic activity test. The cells were thoroughly washed with PBS solution after the incubation with the XTT salt and lysed using 0.1 vol. % Triton X-100 in PBS for 10 minutes at 37 °C. The ALP activity was evaluated using an ALP colorimetric assay kit (Abcam) following the supplier instructions. The ALP activity was calculated as the p-nitrophenol (pNP) generated by samples during the assay per unit of sample volume and minute of reaction. All the experiments were run in triplicates for statistical analysis.

#### **4.6 STATISTICAL ANALYSIS**

All the mechanical tests, degradation behaviour and cytocompatibility assays were performed for each type of material in triplicates. The statistical differences between the interpenetrated Mg/CaP composites were determined using the *t*-student test and the one-way ANOVA analyses of variance.

The significance was set at  $p < 0.05$ . All data from statistical analyses presented in this thesis are expressed as a mean value with its standard deviation.

## 5. RESULTS AND DISCUSSION

### 5.1 INFILTRATION OF $\beta$ -TCP SCAFFOLDS WITH Mg: PRELIMINARY CASE STUDY AND PROOF OF CONCEPT.

#### 5.1.1 PROCESSING OF INITIAL MATERIALS

In order to evaluate the feasibility of the production of interpenetrated degradable biomaterials, an initial study was carried out using a commercial  $\beta$ -TCP powder and pure Mg. The ceramic powder was used for the fabrication of porous scaffolds of different nominal pore sizes, i.e. 150, 350, 500, and 1000  $\mu\text{m}$ . These porous scaffolds were infiltrated with pure-Mg pellets via CAMI.

The X-ray diffraction pattern from the initial commercial  $\beta$ -TCP powder revealed that the powder was formerly composed by a mixture of calcium hydrogen phosphate (monetite,  $\text{CaHPO}_4$ ) in a triclinic lattice structure (ICSD: 87196) and synthetic calcium-deficient hydroxyapatite (CDHA) in its hexagonal phase (ICSD: 082291). The Rietveld analysis showed that the initial mixture had ~35 wt. % of monetite and the rest was CDHA. The mixture reacted by a solid-state reaction at high temperature producing  $\beta$ -TCP [91]. The process happened by the decomposition of  $\text{CaHPO}_4$  into calcium pyrophosphate (CPP,  $\text{Ca}_2\text{P}_2\text{O}_7$ ), which later reacted with HA to form  $\beta$ -TCP. Thus, the heat treatment parameters such as temperature and dwell time are of high importance in the evolution of the reaction and final composition. In the case study, the final composition resulted in a mixture of  $\beta$ -TCP (ICSD: 006191) and tetragonal CPP (ICSD: 73712) with a mass composition of 80.7 % and 19.3 %, respectively.

**Figure 8a** shows the X-ray diffraction patterns of the commercial VWR powder and its microstructure by SEM. The powder contains a homogeneous distribution of coarse flake-like HA particles and small rounded monetite particles that are the reactants to produce  $\beta$ -TCP after the calcination or sintering at 1100  $^\circ\text{C}$  for 5 h (**Figure 8b**). These sintering conditions were selected for the consolidation of the initial scaffolds in **section 5.1.2**.

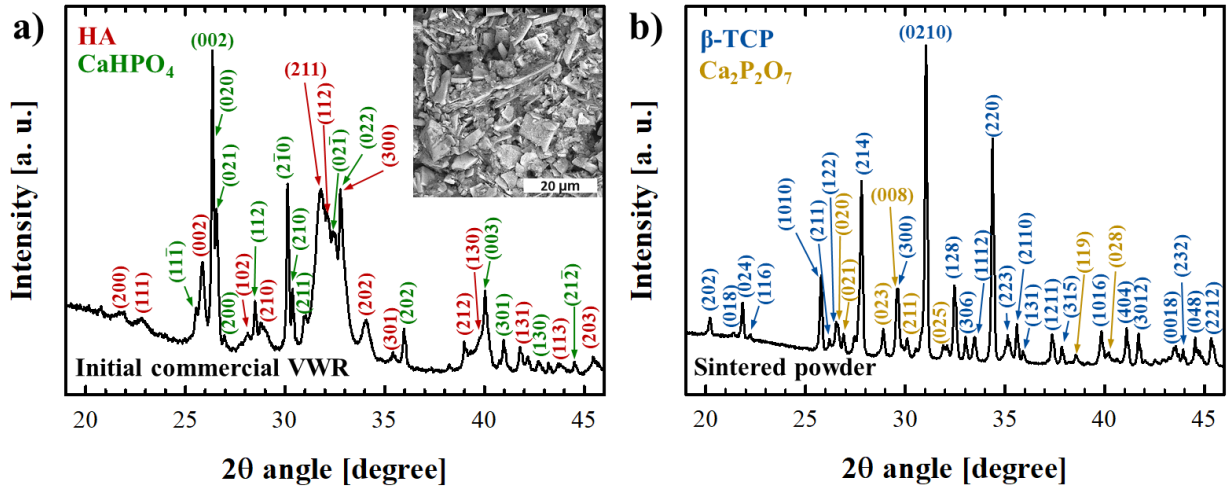


**Figure 8.** XRD pattern and microstructure observation of a) initial  $\beta$ -TCP powder (VWR, Belgium); and b) XRD after sintering at 1100 °C for 5 h.

### 5.1.2 ROBOCASTING OF $\beta$ -TCP SCAFFOLDS WITH DIFFERENT PORE SIZES

The  $\beta$ -TCP cylindrical scaffolds were 3D-printed with grid apertures of 150, 350, 500, and 1000  $\mu\text{m}$ . In **Figure 9** the whole processing and characteristic samples and their microstructures from the obtained  $\beta$ -TCP scaffolds are shown before the infiltration process.

All the samples were produced using the same parameters. After sintering at 1100 °C for 5 hours, the pore size of the porous structures was found to be different to the nominal pore size due to the anisotropic shrinkage of the samples during the drying and the sintering of the green bodies [57–59]. The final dimensions of the produced  $\beta$ -TCP scaffolds are listed in **Table 4**.

**Figure 9a** shows the robocasting process of a  $\beta$ -TCP scaffold with a nominal pore size of 150  $\mu\text{m}$ . The resulting cylindrical porous structure and precision of the deposition of the ceramic strands can be found only for the scaffolds with the smallest and biggest nominal pore sizes, namely 150  $\mu\text{m}$  (**Figure 9c**) and 1000  $\mu\text{m}$  (**Figure 9d**), respectively. After sintering, the pore geometry remained homogenous and the ceramic strands presented a typical sintered microstructure for  $\beta$ -TCP (**Figure 9e-f**), presenting an inner porosity below 5  $\mu\text{m}$  with homogeneous distribution along the whole specimens (**Figure 9f**).

The accuracy of the final geometry of the scaffolds following an orthogonal pattern depends highly on the rheology of the ceramic paste that is used for the robocasting and on the sintering

properties of the material. Therefore, a bigger aperture between the strands that form the pore channels in the preforms can lead to more imperfections in the final structure due to the absence of supporting material that keeps the scaffold integrity. The rheology effect on the robocasting has therefore been widely explained for a varied number of materials. In general, the injectable pastes are viscoelastic, having a transition from liquid to solid state after a stabilization time [92]; if the stabilization time does not match with the deposition speed and an upper layer is deposited over the previous one while this still remains in a semiliquid state, then the overlapping and distortion of the strands and thus its geometry are affected [57,93]. In addition, a long distance between the strands, i.e. a big pore aperture, produces a bending effect of the unsupported filament. This effect was observed in the  $\beta$ -TCP samples with a nominal pore size bigger than 500  $\mu\text{m}$  (**Figure 9d**).

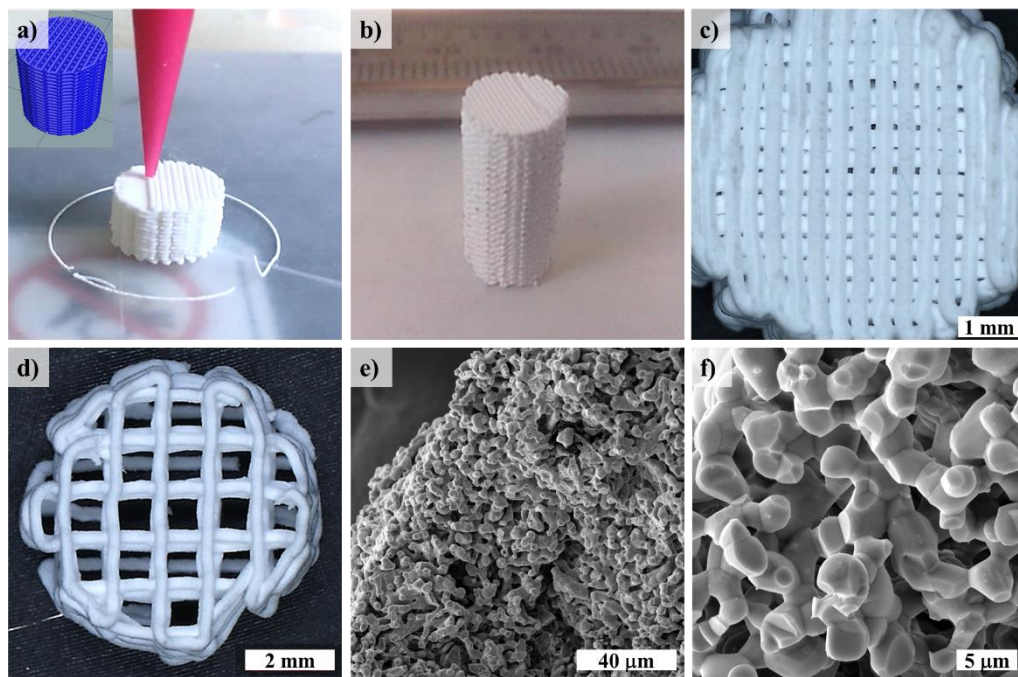


**Figure 9.** a) Computed design for the construction of cylindrical scaffolds in blue and real-time sample printing by means of robocasting process; b) characteristic sample after sintering with a nominal pore size of 150  $\mu\text{m}$ ; c) top view of a characteristic scaffold with a 150- $\mu\text{m}$  pore size; d) top view of a characteristic scaffold with a nominal 1000- $\mu\text{m}$  pore size; e) SEM image of typical microstructure after the sintering of  $\beta$ -TCP strands; and f) detailed micrograph of the microstructure and inner porosity of the  $\beta$ -TCP scaffolds.

**Table 4.** Nominal dimensions and final dimensions after the sintering of preliminary  $\beta$ -TCP scaffolds.

Nominal pore size [ $\mu\text{m}$ ]	Pore size after sintering 1100 °C for 5 h [ $\mu\text{m}$ ]	Nominal diameter / length of cylindrical scaffolds [mm]	Final diameter / length of cylindrical scaffolds [mm]
150	$150 \pm 16$	7.5 / 15	$6.8 \pm 0.2$ / $13.3 \pm 0.2$
350	$345 \pm 29$	7.5 / 15	$6.6 \pm 0.2$ / $12.6 \pm 0.1$
500	$533 \pm 32$	7.5 / 15	$6.5 \pm 0.4$ / $12.9 \pm 0.4$
1000	$935 \pm 39$	7.5 / 15	$6.2 \pm 0.2$ / $11.8 \pm 0.7$

### 5.1.3 MANUFACTURING AND CHARACTERIZATION OF Mg/ $\beta$ -TCP INTERPENETRATED COMPOSITES

The infiltration with pure Mg into the porosity of  $\beta$ -TCP preforms was carried out by means of current-assisted metal infiltration (CAMI). **Figure 10** shows a characteristic interpenetrated Mg/ $\beta$ -TCP composite, with a screw-like appearance. The metallic material covers and infiltrates the porous ceramic structure. Therefore, by performing cuts along the cylindrical samples, the infiltrated ceramic structure could be observed. The Mg seemed to successfully infiltrate the ceramic preforms, even the porosity of the strands and some cracks present in the ceramic scaffolds. Also, the presence of reactivity between the metallic and the ceramic phases was noticed after the metallographic sample preparation, especially in the vicinity of the ceramic strands (detail in **Figure 10**), revealing that the molten Mg partially dissolved the ceramic preform.

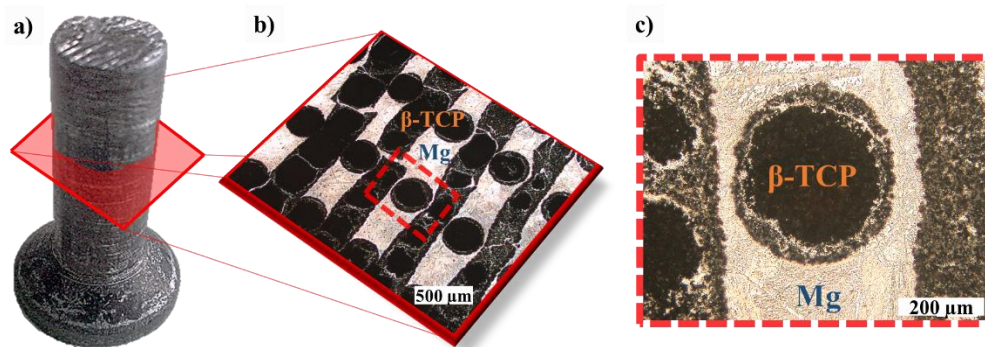


**Figure 10.** a) Characteristic screw-like specimen obtained from the CAMI of  $\beta$ -TCP preforms with a nominal pore size of 500  $\mu\text{m}$  infiltrated by pure Mg; b) optical microscopy images from a transversal cut of the cylindrical sample (the metallic and ceramic phases are marked); c) detail of a cylindrical strand revealing the molten metal infiltration and interaction between the materials.

The success of the infiltration process was analysed by micro-computed tomography ( $\mu$ -CT) and differentiating the pixels in the phases present within the composite: ceramic phase (commercial  $\beta$ -TCP), metallic phase (pure Mg), and remaining porosity (locked air). The results are shown in **Figure 11**.

The preservation of the ceramic preforms after the infiltration process was estimated by the volumetric analysis from the computed reconstruction of the samples in order to highlight the overload that the ceramic preform undergoes during the CAMI, correlate it with the 3D-printed perform pore size, and, consequently, determine the minimum pore size suitable for manufacturing the rest of the Mg/CaP composites.

The successful rate of infiltration was calculated for each set of scaffolds with a different pore size (**Eq. 7**). It was found that a larger pore size facilitates the infiltration process, keeping intact the ceramic preform structure. Samples with a pore size of about 1000  $\mu\text{m}$  revealed the highest degree of infiltration with an average value of 97.5 % of infiltrated volume of the total macro porosity, followed by the scaffolds with 500- $\mu\text{m}$  pores (96.3%). Higher amounts of remaining porosity were found in samples with a pore size of below 350  $\mu\text{m}$ . However, the reduction in the pore size did not have a significant effect on the degree of infiltration when comparing the scaffolds with pore sizes of 350 and 150  $\mu\text{m}$ , which were infiltrated by  $\sim$ 95.5 % of their initial porosity (**Figure 11**).

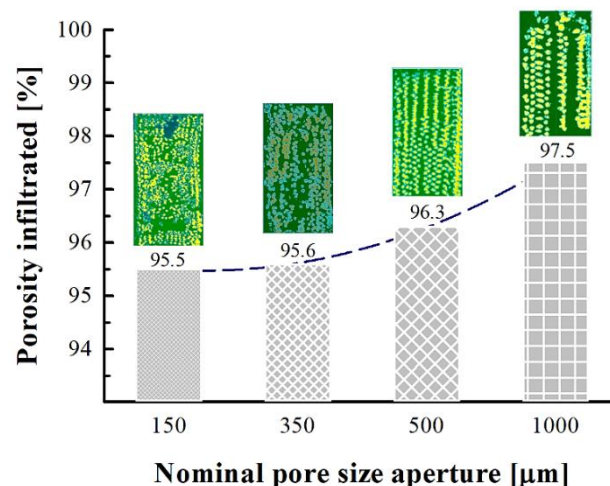


**Figure 11.** Percentage of infiltration degree in Mg/ $\beta$ -TCP composites obtained by CAMI with respect to the initial pore size of the ceramic preforms. Insets show the characteristic longitudinal cut of the imaging reconstruction by  $\mu$ -CT, where the ceramic phase is highlighted in yellow and the Mg in green.

The remaining porosity after the infiltration is mainly connected with the tendency of the molten Mg not to penetrate and fill the pores of the ceramic preforms, which might also cause their partial destruction if the molten metal exerts too high a pressure on the porous ceramic preforms.

**Figure 12** shows the computed reconstruction and separation of the phases for representative samples from each tested pore size of the ceramic preforms. The longitudinal-cut view revealed a clear evidence of the effect of the pore size on the restriction for the molten metal infiltration. Samples with a small pore size, i.e. below 350  $\mu\text{m}$ , tended to obtain more porosity after CAMI, which is connected to the higher resistance of the ceramic preform to being infiltrated, as is also stated by Darcy's law (**Eq. 11**).

$$v = \frac{k dp}{\mu dx} \quad (\text{Eq. 11})$$

where  $v$  is the infiltration rate of the molten metal,  $k$  is the permeability, which depends on the shape and size of the interconnected channels through which the molten metal flows,  $\mu$  is the viscosity of the molten metal,  $dp$  is the change in pressure correlated with the size and shape of the pores that are in contact with the molten metal, and  $dx$  is the infiltration distance.

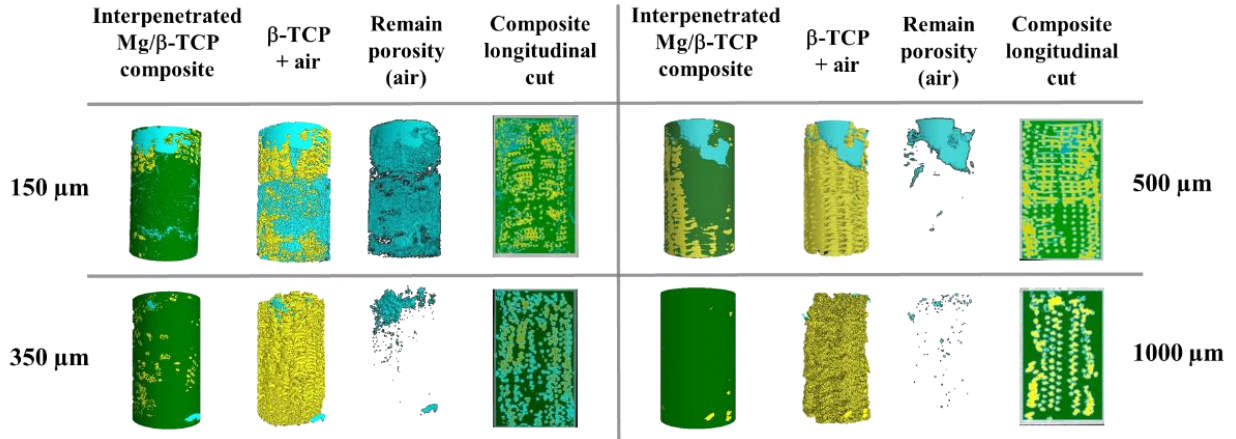


**Figure 12.**  $\mu$ -CT reconstruction of Mg/ $\beta$ -TCP composites with different nominal pore sizes of the ceramic preforms. Mg is highlighted in green colour,  $\beta$ -TCP is in yellow, and the remaining porosity is in blue.

Therefore, based on Darcy's law, the permeability and strength stability of the preforms during the infiltration process are important factors for a successful infiltration. Small-pore channels decrease the permeability, incrementing the stress in the preform [17]. This effect was

observed in the  $\beta$ -TCP porous structures with a small pore size, which presented a higher tendency to lose their integrity and be destroyed during the infiltration in comparison with the preforms with a pore size of above 500  $\mu\text{m}$ , i.e. samples in which the ceramic preform structures were generally preserved and the degree of infiltration was higher.

An X-ray diffraction analysis of the Mg/ $\beta$ -TCP composites revealed the presence of a chemical reaction between the  $\beta$ -TCP and molten Mg, resulting in the formation of an intermetallic phase characterized as  $\text{Mg}_2\text{Ca}$  (ICSD: 165564). This phase appears when the content of Ca in Mg is above 1.34 wt. %, i.e. above the solubility limit of Ca in Mg [94]. The precipitation of this intermetallic phase confirms the degradation of the calcium phosphate promoted by the interaction with the molten Mg [86,95]. Despite this degradation, the ceramic phase remained chemically structured as  $\beta$ -TCP (ICSD: 006491). Additionally, the presence of magnesium oxide ( $\text{MgO}$ , ICSD: 060492) was also registered (**Figure 13**).

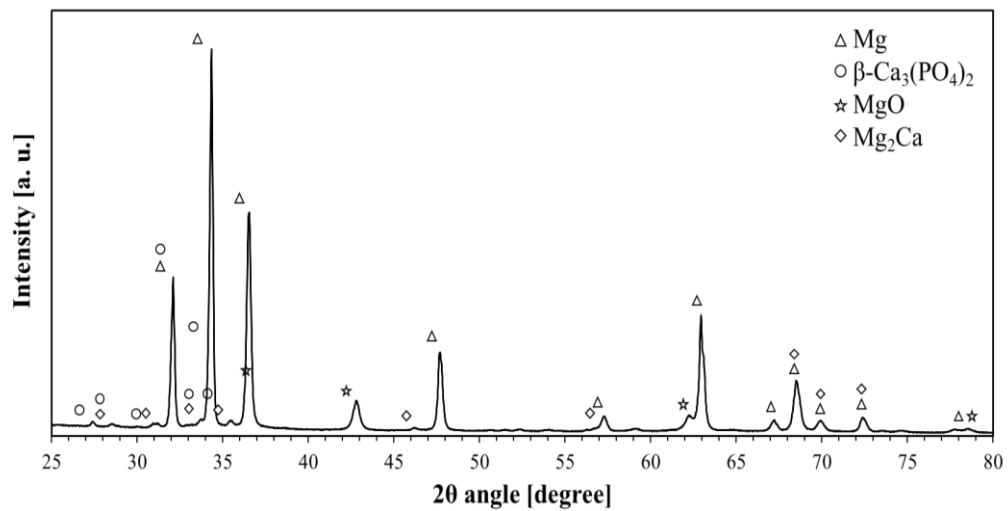


**Figure 13.** X-ray diffraction pattern from the interpenetrated Mg/ $\beta$ -TCP composite.

The microstructure of the interpenetrated Mg/ $\beta$ -TCP composite pointed out two main components, i.e. ceramic and metallic phases. The large grains of the metallic phase were visible after the polishing and etching of the samples (**Figure 14a**). Detailed observation of the metallic phase revealed the presence of a eutectic phase,  $\text{Mg} + \text{Mg}_2\text{Ca}$  (**Figure 14b**). The  $\text{Mg}_2\text{Ca}$  intermetallic is of brittle nature, tending to spall out and leave the Mg matrix, enhancing the effect of increasing the porosity in the metallic phase. This was supported by the shape of the pores in the

metallic section, which were of the same form and alignment as the intermetallic phase, see **Figure 14c**. The presence of the intermetallic phase corroborates the dissolution of the calcium phosphate in the interaction with the molten Mg during the infiltration process because it is the only calcium source in the Mg/ $\beta$ -TCP composite.

The microstructural analysis validated that the ceramic preform was infiltrated by the molten Mg even in the small pores (below 2  $\mu\text{m}$ ) that were also present within the ceramic filaments (**Figure 14b**), pointing out a good permeability in the composite manufacturing process.

The elemental mapping of the Mg/ $\beta$ -TCP composite in its chemical composition was done by the energy-dispersive X-ray spectroscopy (**Figure 14d**). The results confirmed that calcium is also entering the Mg phase while it forms a eutectic phase with a stoichiometry equivalent to the  $\text{Mg}_2\text{Ca}$  intermetallic phase. In addition, the presence of Mg inside the pores within the ceramic filaments was also detected and is in accordance with all the previously observed microstructures.

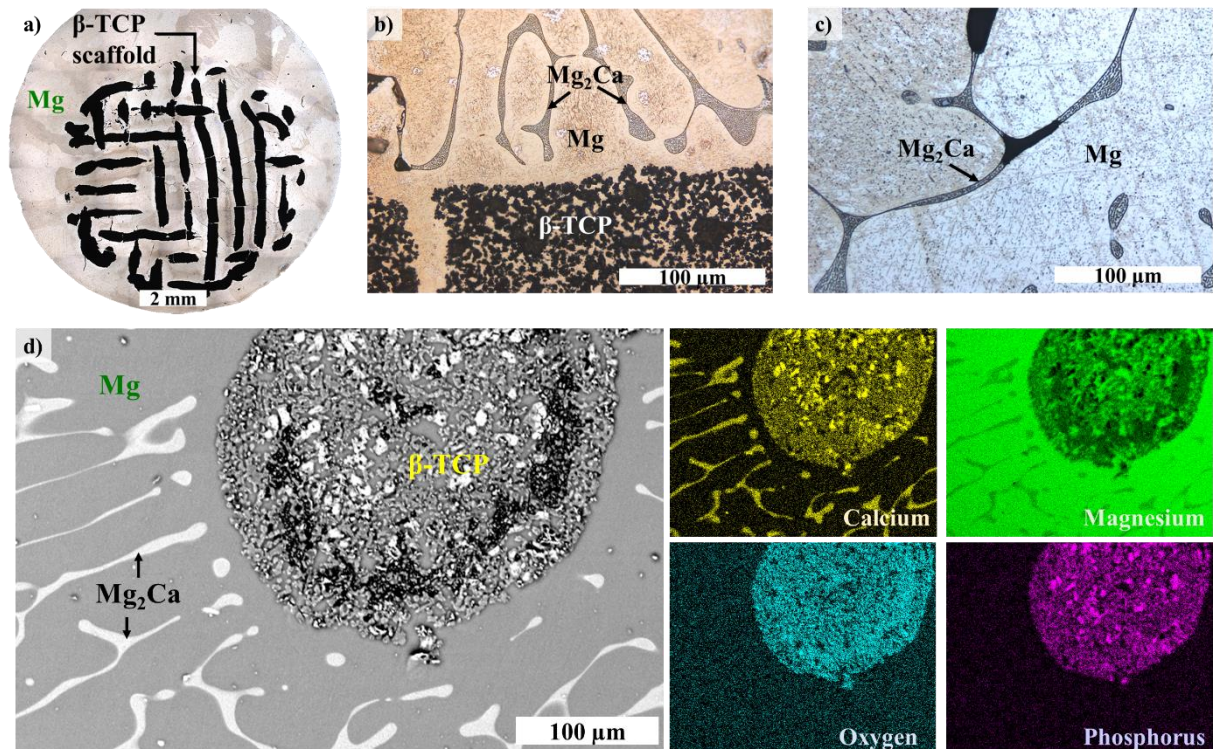


**Figure 14.** Optical microscopy images of Mg/ $\beta$ -TCP interpenetrated composite. a) General overview; b) detail of the interface; c) detail of the metallic phase revealing the presence of  $\text{Mg}_2\text{Ca}$  intermetallic phase; d) SEM micrograph and distribution of elements registered by EDX from a characteristic region of the composite.

In terms of mechanical properties, the pore size aperture of the initial  $\beta$ -TCP preforms resulted in a wide response behaviour under the compression test. The average values of the mechanical properties of the composites and their standard deviations are summarized in **Table 5**. The distribution and the amount of the phases in the interpenetrated composites had a clear effect on the elastic modulus and maximum load bearing values, as well as on their strain, i.e. ductility.

Higher amounts of the ceramic phase strengthen the composite, providing higher load bearing properties but losing ductility in contrast to the composites with a higher amount of the metallic phase. This change in mechanical properties is clearly seen when comparing the limits of the composites studied in this work, for instance when comparing the nominal pore sizes of 150  $\mu\text{m}$  and 1000  $\mu\text{m}$ .

**Table 5.** Mechanical properties of different interpenetrated Mg/ $\beta$ -TCP composites based on the initial nominal pore size of the ceramic preform measured under compressive test.

Pore size [ $\mu\text{m}$ ]	Young's modulus [GPa]	Compressive yield strength [MPa]	Ultimate compression strength [MPa]	Deformation [%]
150	$9.0 \pm 5.3$	$83.9 \pm 10.3$	$112.8 \pm 16.5$	$5.5 \pm 1.5$
350	12.7	134.6	164.3	6.1
500	$7.4 \pm 1.3$	$130.1 \pm 44.4$	$151.2 \pm 30.8$	$5.1 \pm 1.2$
1000	$4.1 \pm 1.3$	$59.4 \pm 38.4$	$116.5 \pm 36.8$	$9.3 \pm 3.0$

The characteristic stress-strain curves for each initial nominal pore size of the ceramic phase are shown in **Figure 15**.

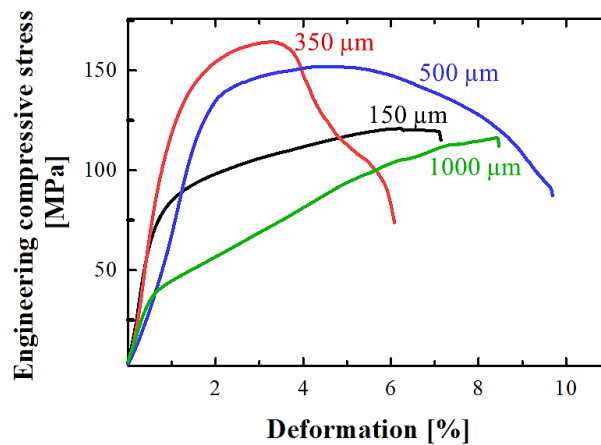


**Figure 15.** Compressive stress-strain curves for different  $\beta$ -TCP preforms infiltrated with pure Mg by CAMI.

The deviation in the mechanical properties of the same type of interpenetrated composites is considerably wide. This is attributed to the degradation of the ceramic phase provided by the reaction with the molten Mg during the infiltration, which cannot be precisely controlled.

In the same way, the damage to the ceramic preform is a significant factor for the mechanical response. Nevertheless and despite the wide range of the mechanical properties, the interpenetrated Mg/ $\beta$ -TCP composites revealed a suitable mechanical behaviour for load-bearing applications in orthopaedics compared to the natural bone properties. The best interpenetrated composite, in terms of the mechanical properties, was found for the  $\beta$ -TCP scaffolds with a nominal pore size between of 350 and 500  $\mu\text{m}$ , due to the cavity size, which is big enough for the penetration of molten magnesium. Moreover, the big cavities produce a bigger apparent density of the ceramic phase, leading to lighter composites.

Finally, the degradation test was carried out in order to evaluate the feasibility of Mg/CaP as degradable composites. For this purpose, a saline solution containing 0.9 wt. % of NaCl and discs obtained from the Mg/ $\beta$ -TCP composite with the 350- $\mu\text{m}$  nominal pore size preform (**Figure 16a**) were used. The immersion test was monitored during the first 24 h comparing the interpenetrated composite against pure Mg discs.

After 24 h of immersion, the interpenetrated composites surface was covered with a film formed by the precipitated salt and corrosion products (**Figure 16b**); nevertheless, the discs kept their integrity during the whole corrosion test.

Once the corrosion products were removed (**Figure 16c**), the estimated degradation rate (DR) was calculated vs time (**Figure 16d**). The results showed that the highest DR ( $135.6 \text{ mm}\cdot\text{year}^{-1}$ ) for pure magnesium presented after 6 h in saline solution, while the highest value for the interpenetrated composite was found after 3 h ( $40.8 \text{ mm}\cdot\text{year}^{-1}$ ). Afterwards, for both materials, the corrosion speed decreased, reaching the lowest registered values after 24 h of immersion. This can be attributed to the formation of the protective layer during the corrosion.

The pure Mg revealed a faster corrosion rate compared to the Mg/ $\beta$ -TCP composite. After 24 h of immersion in saline solution, the degradation rates of Mg and interpenetrated composite were  $52.4$  and  $12 \text{ mm}\cdot\text{year}^{-1}$ , respectively. The reduction in the degradation rate is attributed to the

formation of a MgOH layer on the surface of the samples, which impairs the corrosion process [9,94].

The results pointed out that the addition of  $\beta$ -TCP in a composite with Mg helps to increase the corrosion resistance of the material by decreasing the exposed surface area of Mg. Even though the combination of  $\beta$ -TCP with Mg significantly reduced the corrosion rate, the calculated values were found to be outside the requirements for a functional treatment of bone defects (at least 3 months of stability) [3,96].

Nevertheless, the degradation resistance is better if the precipitation of the  $Mg_2Ca$  intermetallic is avoided. This is in accordance with the premise that the presence of an intermetallic enhances the galvanic corrosion with the pure Mg phase. Thus, intermetallic phases increase the degradation speed but at the same time promote the formation of a protective layer composed by the corrosion products [94,97].

Based on the results obtained from the initial Mg/ $\beta$ -TCP composites, effort was made to avoid the precipitation of an intermetallic phase in further produced interpenetrated materials in order to improve their corrosion resistance.

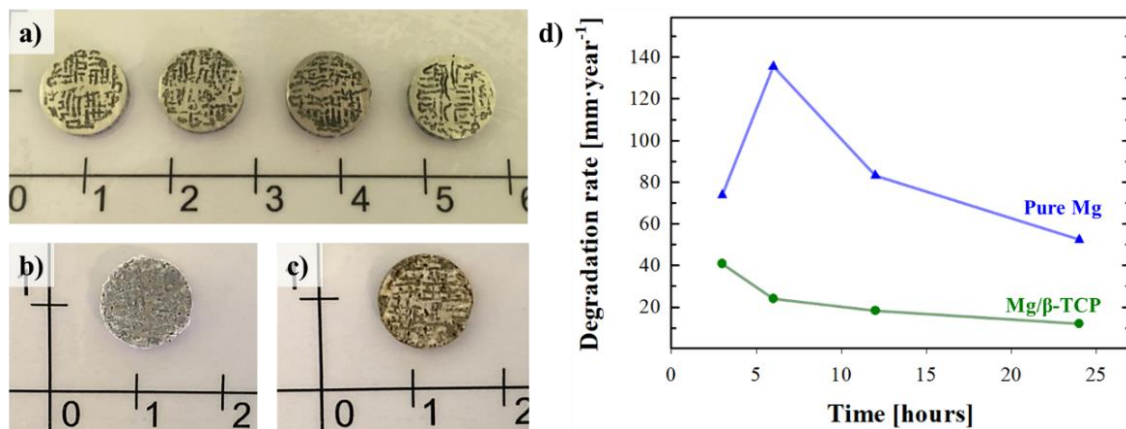


**Figure 16.** a) Initial Mg/ $\beta$ -TCP discs for the degradation test; b) Mg/ $\beta$ -TCP disc after 24 h of immersion in saline solution; c) Mg/ $\beta$ -TCP sample after the removal of corrosion products; d) corrosion rates over time for pure magnesium and Mg/ $\beta$ -TCP composite.

## **5.2. MANUFACTURING AND TESTING OF INTERPENETRATED Mg/CaP SYSTEMS.**

The selection of an optimal pore size in the interpenetrated Mg/CaP composites is quite challenging because of a compromise between the mechanical properties and the degradation rate. A small pore size in the ceramic preform results in better mechanical responses based on the higher amount of the ceramic phase, but it is unfavourable for the infiltration process and the integrity of the preform during the manufacturing. On the other hand, a larger pore size increases the area where the metallic phase is in contact with a corrosion medium, accelerating the degradation of the composite material.

The apparent discrepancy between the properties that could be considered as a drawback is in fact an advantage in the design of suitable degradable devices with tailored mechanical properties. The tailored properties can be achieved with the distribution of the phases in the produced interpenetrated composites, which leads to different mechanical and degradation behaviour.

From the results of the previous case study and based on the mechanical testing of the interpenetrated Mg/ $\beta$ -TCP composites, it was concluded that a pore size in the range of 350-500  $\mu\text{m}$  is the most suitable for the manufacturing of load-bearing composites in orthopaedics. Further Mg/CaP composites were therefore produced using preforms with a nominal pore size of 500  $\mu\text{m}$  after the robocasting to ensure optimal mechanical properties and controlled degradability.

The investigated CaP compounds in the following sections are: HA, CDHA and  $\beta$ -TCP. The aim was to compare the behaviour of interpenetrated composites using pure Mg, Mg containing 0.2 wt. % of Ca and containing 1 wt. % of Zn.

### **5.2.1 SYNTHESIS AND MANUFACTURING OF CAP SCAFFOLDS.**

The syntheses of HA and  $\beta$ -TCP powders were performed through wet chemistry by the chemical precipitation method. The reaction was between phosphoric acid ( $\text{H}_3\text{PO}_4$ ) and calcium hydroxide ( $\text{Ca}(\text{OH})_2$ ). Stoichiometric HA and  $\beta$ -TCP keep the Ca/P atomic ratio of 1.67 and 1.5, respectively. Thus, solutions of each of the reactants in 1-M concentration were mixed dropwise in an aqueous solution, keeping the respective Ca/P ratios in order to obtain the desired compound.

The solubility of CaP's in water solution depends on the pH and temperature. The solubility of HA is the lowest in a pH of above 4.2 at room temperature. Thus, HA is the most thermodynamically stable phase in a  $\text{Ca}^{2+}/\text{P}^{3-}$  solution, and, consequently, it precipitates in all cases where these two ions are present [98]. From this, it is clear that  $\beta$ -TCP cannot be directly obtained by the chemical precipitation method but it can be transformed from a non-stoichiometric apatite, whose Ca/P ratio is between 1.33 and 1.65. The transformation occurs as a decomposition process, which is promoted by heat treatment, usually below 900 °C [99]. Therefore, wet chemistry can be used for the synthesis of stoichiometric HA and calcium-deficient HA (CDHA), where the latter can be calcined to produce  $\beta$ -TCP.

The synthesis of HA was performed successfully by mixing the reactants solutions and keeping the pH between 8 and 9, to ensure the precipitation of stoichiometric HA. Nevertheless, the synthesis of  $\beta$ -TCP was more complicated due to the presence of remaining HA or CDHA in the final product. **Figure 17** shows the X-ray diffraction patterns of different synthesis conditions for  $\beta$ -TCP. The presence of CDHA is highlighted by the red section in the figure, where the main diffraction peak of the HA is listed.

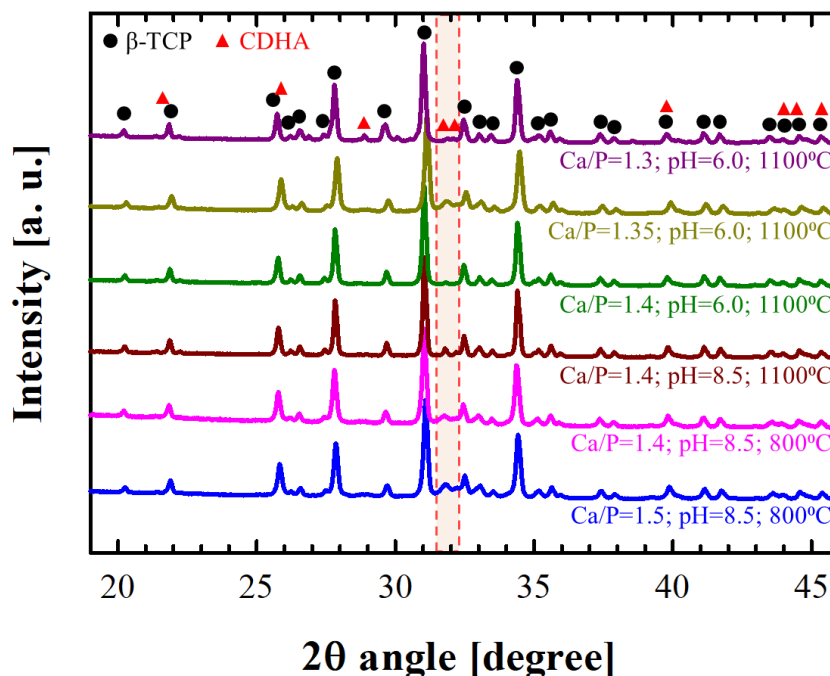


**Figure 17.** XRD of the different conditions for the synthesis of  $\beta$ -TCP. Variables are the Ca/P ratio, pH value and calcination temperature.

**Table 6** summarizes the most characteristic synthesis trajectories for various Ca/P molar ratios, pH values and post-heat-treatments and reports the chemical composition estimated by the Rietveld analysis from the X-ray diffractogram of the final products after the calcination. Generally, the acidic pH favoured the precipitation of CDHA, which can later transform to  $\beta$ -TCP after a high-temperature treatment.

Theoretically, the transformation of CDHA by thermal decomposition can result in the entire formation of  $\beta$ -TCP but the efficiency of the reaction is linked to the nature of the initial CDHA; thus, for different Ca/P molar ratios and different thermal treatments of the obtained CDHA powders, the decomposition process has different decomposition kinetics.

The results prove that at a Ca/P ratio of 1.3, calcium pyrophosphate (CPP,  $\text{Ca}_2\text{P}_2\text{O}_7$ ) was produced, showing a lack of calcium ions for the formation of either CDHA or  $\beta$ -TCP. In contrast, a Ca/P ratio of 1.4 and pH between 6 and 8.5 (which is suitable for stoichiometric HA production) are the best conditions for the synthesis of nearly pure  $\beta$ -TCP phase after the calcination at a temperature of 1100 °C.

**Table 6.** Synthesis conditions for HA and  $\beta$ -TCP powders produced by chemical precipitation and after 3-hour heat treatment, with the resulting chemical composition by the Rietveld analysis.

Synthesis	Ca/P ratio	pH	Heat treatment	HA [wt. %]	$\beta$ -TCP [wt. %]	CDHA [wt. %]	$\text{Ca}_2\text{P}_2\text{O}_7$ [wt. %]
HA	1.67	~ 8.5	800 °C	100 %	-	-	-
$\beta$ -TCP	1.5	~ 8.5	800 °C	-	80.0 %	20.0 %	-
$\beta$ -TCP	1.4	~ 8.5	800 °C	-	85.0 %	15.0 %	-
$\beta$ -TCP	1.4	~ 8.5	1100 °C	-	93.6 %	6.4 %	-
$\beta$ -TCP	1.4	~ 6.0	1100 °C	-	99.5 %	0.5 %	-
$\beta$ -TCP	1.35	~ 6.0	1100 °C	-	81.3 %	18.7 %	-
$\beta$ -TCP	1.3	~ 6.0	1100 °C	-	95.0 %	-	5.0 %

For the consolidation of preforms made of HA and  $\beta$ -TCP, a sintering process can be carried out; this is not the case for CDHA-based structures because a thermal treatment decomposes this type of calcium phosphate before the consolidation process is completed.

Therefore, the selected route for the processing of consolidated CDHA structures had to be different. Thus, a solid-state reaction between monetite (calcium hydrogen phosphate,  $\text{CaHPO}_4$ )

and calcium carbonate ( $\text{CaCO}_3$ ) was carried out at a temperature of 1400 °C in order to produce  $\alpha$ -TCP powder, which was used for the robocasting of the preforms. Later, the  $\alpha$ -TCP structures were hydrated to obtain consolidated CDHA preforms by inter-crossing a fine plate microstructure [100]. This hydration of  $\alpha$ -TCP has been described in detail and used for bone cements [42,46,101].

For the synthesis of  $\alpha$ -TCP, the initial reactants were mixed and sieved together to ensure a homogeneous distribution and a particle size of below 36  $\mu\text{m}$ . During the reaction (**Eq. 5**), monetite decomposes into calcium pyrophosphate ( $\text{Ca}_2\text{P}_2\text{O}_7$ ) above 400 °C [102], which reacts with the calcium oxide formed by the decomposition of  $\text{CaCO}_3$  (between 700 – 900 °C). This solid state reaction produces  $\beta$ -TCP at temperatures above 800 °C [91,102]. The monoclinic phase of the TCP ( $\alpha$ -TCP) is formed and stable above 1300 °C and it can be kept at room temperature by a fast quenching step [46].

**Figure 18** shows the XRD patterns from all the CaP powders used for the robocasting of porous preforms. Comparing the patterns with the standards and performing the Rietveld analysis:

- The initial HA powder was confirmed to be stoichiometric HA (ICSD: 087670).
- A minor trace of CDHA (0.5 wt.%) was detected in the  $\beta$ -TCP powder and the rest was found to be pure rhombohedral TCP ( $\beta$ -TCP, ICSD: 006191).
- The initial  $\alpha$ -TCP powder did not reveal any presence of secondary phases except single monoclinic TCP ( $\alpha$ -TCP, ICSD: 000923).
- CDHA was formed by the hydrolysis of  $\alpha$ -TCP; the composition analysis revealed the presence of two phases, mainly CDHA with 83.7 wt. % (ICSD: 087669) and unreacted monoclinic TCP (16.3 wt. %). The diffraction pattern indicated higher crystallinity for the  $\alpha$ -TCP compared with the CDHA. This is judged from the shape of the diffraction peaks, which is connected to either non-crystalline microstructure or extremely small crystal size in the CDHA phase.

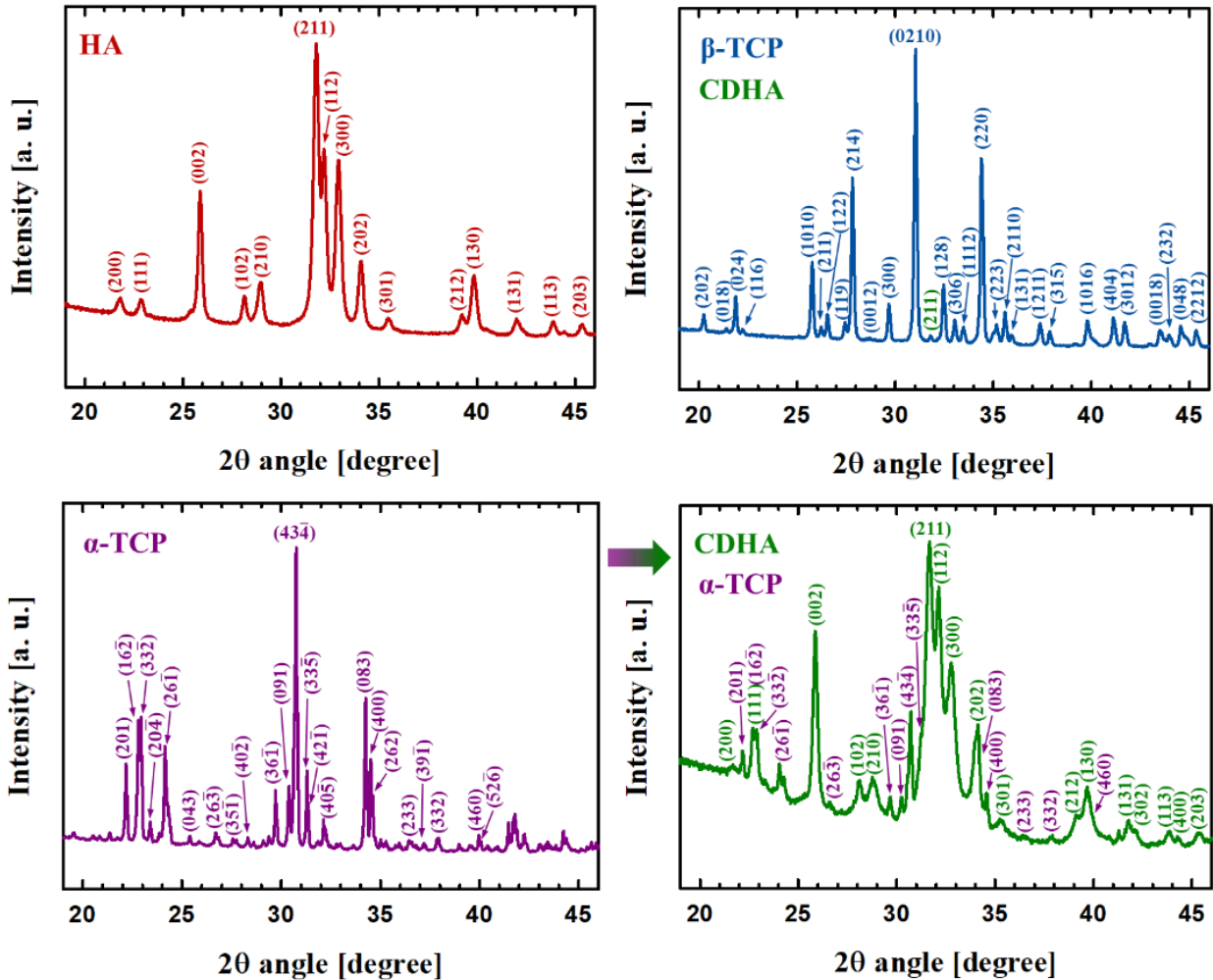


**Figure 18.** X-ray diffraction patterns of synthesised CaP powders. Arrow indicates the transformation of  $\alpha$ -TCP after the hydrolysis.

After the synthesis of the CaP ceramics, the powders were used for the fabrication of porous cylinders following an orthogonal pattern with a designed pore size of 500  $\mu\text{m}$ , which was changed after the consolidation of the structures, especially in the case of the structures that were sintered (HA and  $\beta$ -TCP).

**Table 7** summarizes the change in the dimensions of the cylinders after the consolidation. The HA and  $\beta$ -TCP scaffolds suffered a considerable shrinkage of about 20.0 % on their external dimensions, while the CDHA scaffolds had almost zero shrinkage due to the mechanism of hardening during the hydrolysis of  $\alpha$ -TCP (Eq. 6), which does not include the closing of porosity but a chemical transformation with a change in the microstructure.

The final pore size in the sintered scaffolds was about 300  $\mu\text{m}$ , which is still favourable for the mechanical properties, as was proved in the previously studied Mg/ $\beta$ -TCP interpenetrated composites. In the case of the CDHA preforms, the pore size slightly changed to a mean size of 483  $\mu\text{m}$  because no sintering process was needed for the consolidation.

**Table 7.** Final dimensions and shrinkage of bioceramic scaffolds after consolidation processing.

<b>Final dimensions</b>	<b><math>\beta</math>-TCP</b>	<b>HA</b>	<b>CDHA</b>
Diameter [mm]	$8.1 \pm 0.2$	$7.7 \pm 0.4$	$7.9 \pm 0.3$
Height [mm]	$11.5 \pm 0.3$	$10.9 \pm 0.5$	$11.8 \pm 0.3$
Pore size [ $\mu\text{m}$ ]	$311 \pm 27$	$281 \pm 37$	$483 \pm 36$
<b>Shrinkage</b>			
Diameter [%]	19.0	23.0	1.3
Height [%]	23.3	27.3	1.6
Pore size [%]	37.8	43.8	3.4

**Figure 19** shows the macrographs of the final scaffolds obtained by the robocasting of the HA and CDHA pastes in order to compare the difference between the sintering and the consolidation by hydrolysis. Both processing routes maintained the designed orthogonal pattern along the whole of the cylindrical samples. Nevertheless, a clear and considerable shrinkage in the pore aperture (~40.0 %) was found in the case of the sintered preforms from HA and  $\beta$ -TCP (**Figure 19a-c**), compared to the CHDA scaffolds (**Figure 19d-f**).

Finally, the robocast samples were stored for their further analysis and CAMI infiltration process until the casting and selection of the best corrosion resistant Mg alloy were tested.

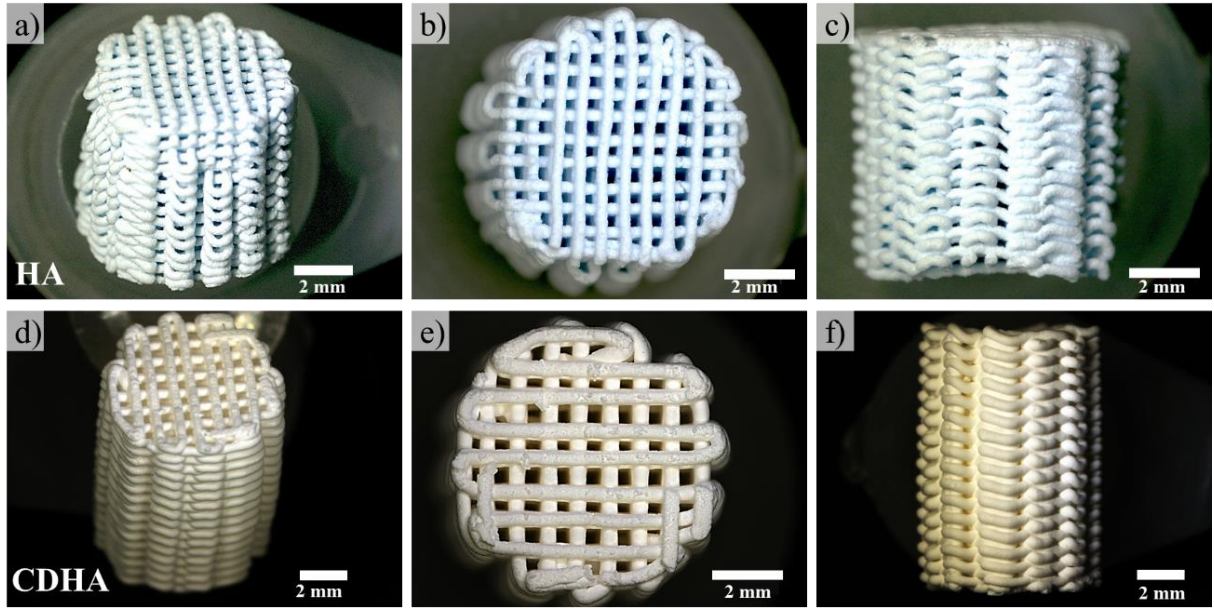


**Figure 19.** Characteristic consolidated HA (a-c) and CDHA (d-f) scaffolds obtained by the robocasting of ceramic pastes.

### 5.2.2. CASTING OF PURE Mg, Mg-Ca AND Mg-Zn ALLOYS AND THEIR DEGRADATION BEHAVIOUR IN SIMULATED BODY FLUID.

Mg containing Ca and Zn as alloying elements have previously been studied as degradable implants, with the finding that high concentrations of Ca or Zn above the solubility limit lead to the precipitation of intermetallic phases, which are detrimental due to the significant decrease in the corrosion resistance of the alloys [9]. Therefore, a proper selection of binary Mg alloys containing low amounts of alloying element, i.e. calcium or zinc, were prepared by casting and subsequently studied for their corrosion behaviour and preliminary cytotoxicity for further manufacturing of interpenetrated composites with CaP compounds by CAMI.

The maximum solubility limit of Ca in Mg is up to 1.34 wt. % at 516.6 °C. By contrast, Zn is slightly more soluble, with a maximum content of 6.2 wt. % at 340 °C [103]. Nevertheless, the maximum solubility drops to ~0.8 wt. % for calcium and 1.6 wt. % for zinc at 25 °C in the equilibrium state [104]. These alloying elements are present in the human body and are essential for many metabolic processes and bone regeneration [104–106].

The manufactured Mg alloys are listed in **Table 8** together with their elemental composition measured by X-ray fluorescence and atomic absorption spectroscopy for a precise estimation of calcium concentration. The chemical composition was in accordance with the nominal composition in the case of the main alloying element, exhibiting only a slight variance in the content of calcium and zinc. The presence of an ultra-low content of other elements that are inherent to the Mg extraction process was also detected and listed in **Table 8**.

**Table 8.** Elemental analysis (wt. %) of pure Mg and processed binary Mg alloys.

Nominal composition	Ca	Zn	Cu	Ni	Fe	Al	Si	Mn	Be
Pure Mg	0.0009	0.0028	0.0015	0.0015	0.0020	<0.01	0.012	0.034	0.00004
Mg-0.2%Ca	<b>0.26</b>	0.0032	0.0016	0.0011	0.0026	<0.01	0.028	0.033	0.00004
Mg-0.4%Ca	<b>0.45</b>	0.0029	0.0018	0.0011	0.0021	0.011	0.028	0.039	0.00004
Mg-0.6%Ca	<b>0.61</b>	0.0027	0.0014	0.0011	0.0022	0.012	0.027	0.036	0.00004
Mg-0.8%Ca	<b>0.81</b>	0.0027	0.0015	0.0020	0.0024	0.012	0.029	0.036	0.00004
Mg-1%Zn	0.0008	<b>0.98</b>	0.0016	0.0017	0.0016	<0.01	0.012	0.035	0.00004
Mg-2%Zn	0.0010	<b>1.93</b>	0.0016	0.0012	0.0017	<0.01	0.012	0.034	0.00004
Mg-3%Zn	0.0009	<b>2.91</b>	0.0015	0.0049	0.0018	<0.01	0.012	0.033	0.00004

The X-ray diffraction patterns for the pure Mg and Mg alloys containing low amounts of Ca or Zn are shown in **Figure 20a**. The typical reflection peaks of the Mg alloys were the same as those for pure magnesium, revealing no formation of intermetallic phases.

Preferential crystal plane orientation in the Mg alloys was found as a consequence of the extrusion and metallographic preparation. Nevertheless, the same diffraction pattern was detected in all Mg alloys. The presence of MgO was detected only in the case of the Mg-0.4%Ca alloy, showing a proper way of processing Mg alloys by means of indirect chill casting and extrusion treatment.

Characteristic microstructures of a pure Mg source and the cast Mg alloys are shown in **Figure 20**. The alloying elements together with the extrusion process led to a grain refinement effect of the alloys, which is desirable for the improvement of the mechanical properties and corrosion resistance of the Mg alloys [107].

The different concentrations of the alloying elements (Ca or Zn) did not have a significant effect on the microstructure of the final alloys. In the case of the Zn addition, the incremental concentration of doping element resulted in a slight coarsening of the Mg alloys microstructure, reporting a mean grain size of about 20  $\mu\text{m}$  (**Figure 20b**). On the other hand, the addition of calcium led to a finer polyhedral grain formation, with an average grain size of 10  $\mu\text{m}$  (**Figure 20c**). Microstructure images of all the processed Mg alloys after the extrusion are located in **Annex 2**.

It has been reported that increasing the amount of Ca in Mg-Ca alloys has a positive influence on the grain refinement effect [108] but in our processed alloys this effect was not clearly apparent.

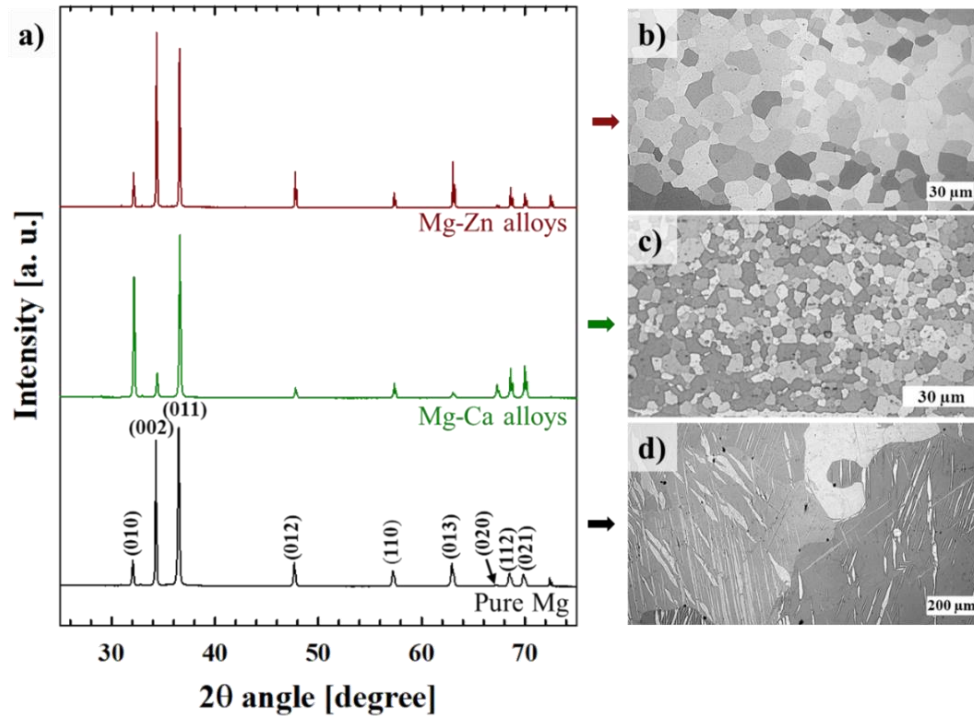


**Figure 20.** (a) Characteristic X-ray diffraction patterns of the initial pure Mg and Mg alloys. Representative optical micrographs of (b) Mg-1%Zn, (c) Mg-0.2%Ca, and (d) pure Mg.

There is a big variation in the methods for estimating the degradation rate of metals. The most precise seems to be the calculation of the direct mass loss after the metallic samples have been exposed to a corrosion medium and once the corrosion products have been removed. Nevertheless, in the case of Mg and its alloys, the removal of corrosion products involves the use of chromium solutions [109], which are toxic and detrimental to the environment. Based on this, different techniques have been developed to provide the basic information on the degradation speed of Mg alloys; among them, H<sub>2</sub> evolution assessment is one of the most widely used. In this study, both the mentioned techniques were used and compared to estimate the corrosion rate of the cast Mg alloys.

Generally, the corrosion rate values obtained by the mass loss technique are lower than those calculated by H<sub>2</sub> evolution assessment. This fact is based on the drawbacks that the H<sub>2</sub> evolution test exhibits; for example, some H<sub>2</sub> bubbles remain attached to the container and are not taken into account in the volumetric measurement. Additionally, the biggest drawback is based on the assumption of the same and constant surface area throughout the whole test [110]. However,

this technique reveals good reproducibility and it also monitors the amount of H<sub>2</sub>-gas production during the Mg degradation. The production of H<sub>2</sub>-gas is an important issue that must be controlled in Mg-based implants in order to prevent the formation of subcutaneous bubbles and the later rejection of the implants once they are inside the human body [111,112].

In **Table 9** are listed the values calculated for all the studied alloys by using both corrosion rate estimation techniques. The difference in estimated values as obtained by the two techniques is evident but the tendency is analogous: lower corrosion resistance when the amount of the alloying element increases.

**Table 9.** Comparison of degradation rate calculated by the mass loss and H<sub>2</sub> evolution techniques for pure Mg and its alloys containing a low amount of Ca or Zn after 2 weeks in SBF at 37 °C.

Mg alloy	Corrosion rate [mm·year <sup>-1</sup> ]	
	Mass loss	H <sub>2</sub> evolution
Pure Mg	-	4.24 ± 0.29
Mg-0.2% Ca	1.27 ± 0.01	2.88 ± 0.18
Mg-0.4% Ca	1.42 ± 0.03	3.02 ± 0.23
Mg-0.6% Ca	1.38 ± 0.04	2.80 ± 0.32
Mg-0.8% Ca	1.43 ± 0.04	2.80 ± 0.16
Mg-1% Zn	1.78 ± 0.04	1.90 ± 0.66
Mg-2% Zn	1.89 ± 0.01	3.25 ± 0.59
Mg-3% Zn	2.21 ± <0.01	2.90 ± 0.24

**Figure 21** shows the evolution of the corrosion rates of the Mg alloys processed by the mass loss technique. The corrosion rates of the Mg alloys are lower than the one reported for pure Mg after 15 days of immersion in simulated body fluid at 37 °C (~3 mm·year<sup>-1</sup>) [113], which is one of the main objectives for the final application as bone regeneration implants.

For the set of Mg-Ca alloys, as the presence of Ca was increased, the degradation rate was increasing. Only the Mg alloy with 0.4 wt. % of calcium revealed at the beginning of the corrosion test a big difference, pointing to a faster corrosion rate than in the case of other produced alloys with higher calcium concentrations. This effect is attributed to the presence of MgO, which was found by XRD only in this alloy. By the end of the assay (after 28 days), the corrosion rate was registered to be slightly incremental in correlation with the calcium concentration; however, all the Mg-Ca alloys were of a similar corrosion rate of about 1.0 mm·year<sup>-1</sup>.

On the other hand, the addition of Zn to Mg revealed a different corrosion resistance behaviour compared with Mg-Ca alloys. The results from the mass loss technique pointed to faster degradation rates, with a clear difference in the addition of Zn, thus, the corrosion rate for the alloy with 3 wt. % of Zn was found to be much faster than for those with a lower Zn concentration.

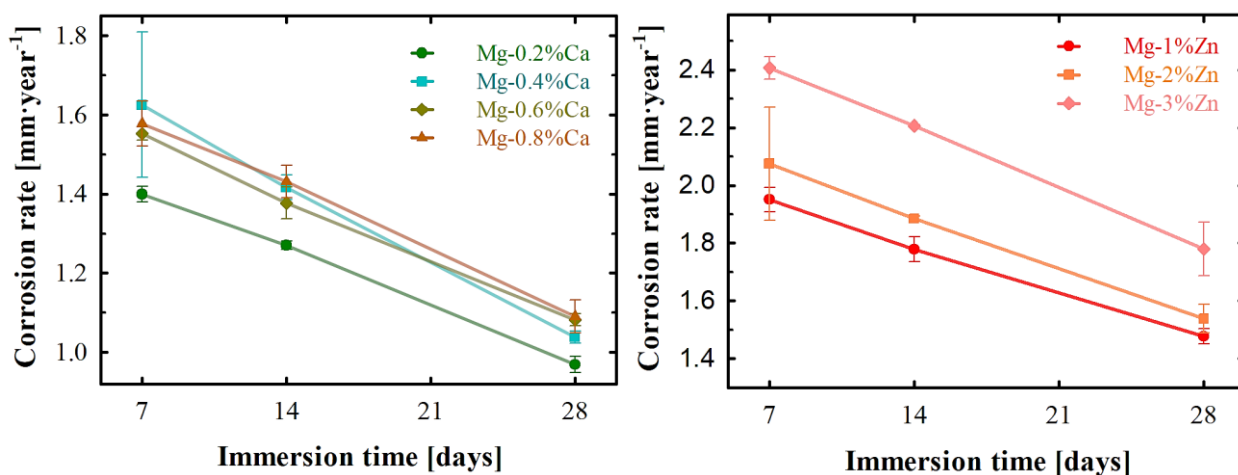


**Figure 21.** Degradation rates of Mg alloys through the first month of immersion in SBF at 37 °C, calculated by the mass loss technique.

The H<sub>2</sub> evolution test (**Figure 22**) revealed the same behaviour for all the Mg alloys compared with the pure Mg, but the degradation rate of the processed alloys was faster during the first hours of immersion, which is also linked to higher H<sub>2</sub>-gas production, which could be a disadvantage for *in-vivo* tests. Nevertheless, if this effect is known, a pre-corrosion process could be performed for the Mg-based biomaterials before they are implanted, to avoid fast gas generation by the formation of a protective corrosion layer.

In contrast to the mass loss technique for the Mg-Ca alloys, in the hydrogen evolution test, the Mg with 0.4 wt. % of Ca showed better corrosion resistance through all the assay. The Mg-Ca alloys reached a stationary state reporting almost the same corrosion rate ( $\sim 2.8 \text{ mm}\cdot\text{year}^{-1}$ ) except the Mg-0.4%Ca, which exhibited a faster corrosion rate (**Table 9**). This effect can be related either to the error of the assumption of a constant surface area along the whole experiment or to the presence of MgO detected by XRD in this alloy (**Annex 2**), which could help to decrease the corrosion rate as a protective layer at the beginning of the assay. This could also explain why this alloy produced the lowest amount of H<sub>2</sub> during the first days of immersion in SBF solution.

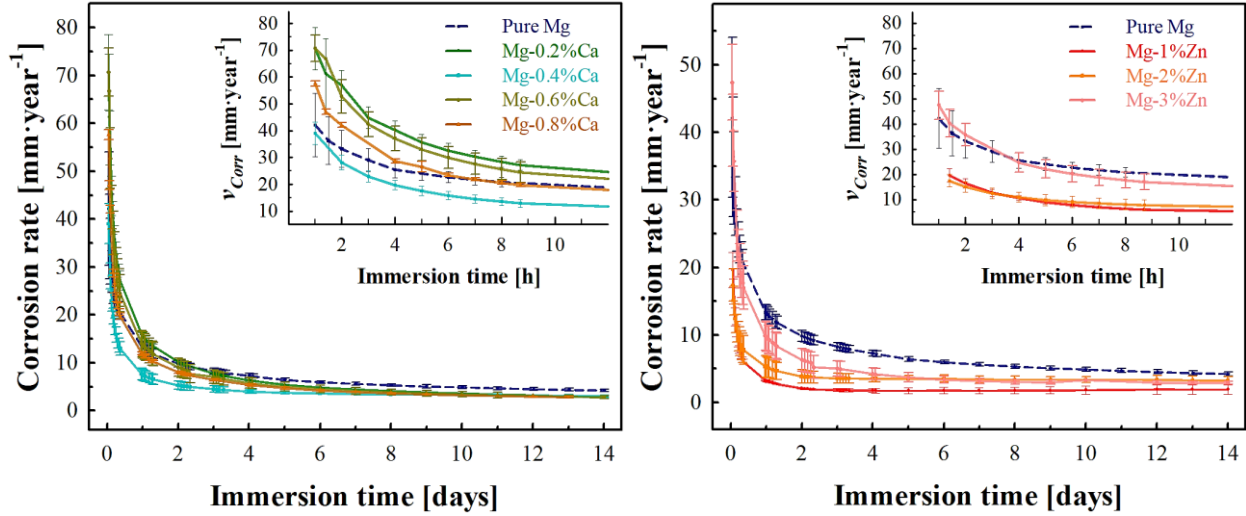


**Figure 22.** Degradation rate assessment of Mg alloys along 2 weeks of immersion in SBF solution at 37 °C by the H<sub>2</sub> evolution assay.

The results from the Mg-Zn alloys were in accordance with the mass loss technique, the increasing concentration of Zn was detrimental to the corrosion resistance. In contrast to the Mg-Ca alloys, the Mg-Zn alloys produced lower H<sub>2</sub> at the initial test state. However, at the end, the corrosion rate of the Mg-Zn alloys was higher than that of the Mg-Ca alloys.

The reactive behaviour of the Mg-Ca alloys can be attributed to the refinement of the microstructure, which is much finer than that of the Mg-Zn alloys. A finer microstructure has the disadvantage of being more reactive due to the higher concentration of grain boundaries. On the other hand, a finer grain-size microstructure corrodes faster at the beginning of the test and forms a protective layer that adheres better than when the grain size is bigger, which was the case of the Mg-Zn alloys. This corrosion layer acts as an inhibitor against further degradation in an SBF solution.

At the end of the H<sub>2</sub> evolution assay, Mg containing 1 wt. % of Zn provided the lowest corrosion rate of the three Mg-Zn alloys studied. In general, these Mg-Zn alloys reported a better corrosion resistance than pure Mg did.

The fast corrosion of pure Mg was attributed to the large grains in its microstructure due to the absence of indirect chill casting and extrusion processing compared with the rest of the alloys (**Figure 20d**).

A preliminary cytocompatibility test was carried out for selected Mg alloys based on the concentration of alloying elements. Thus, the lowest and the highest concentration of the alloying element were chosen for comparison between Mg alloys and pure Mg. **Figure 23** shows the cell proliferation for the bare alloys in contact with spine-bone cells from new-born mice along the first 4 days of the cytocompatibility test. All the metals exhibited good proliferation tendency at the beginning of the test, reaching the limit of cell proliferation after the third day.

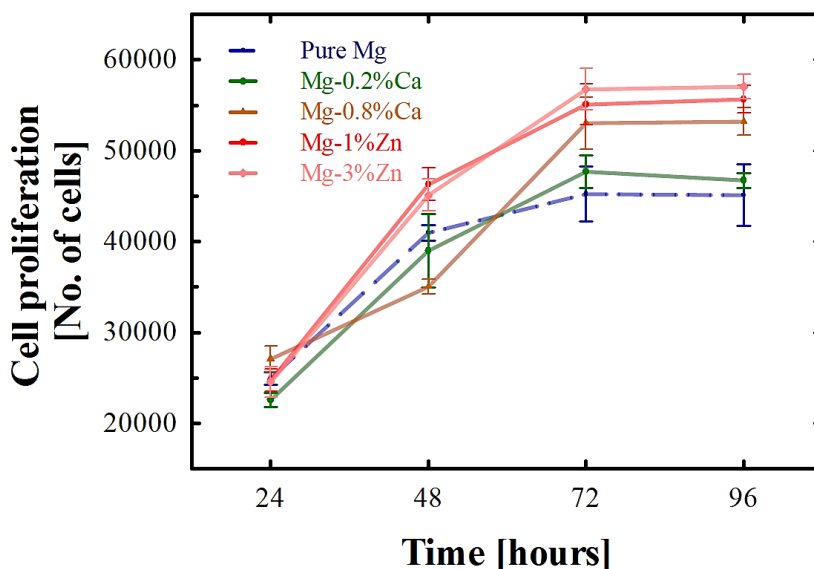


**Figure 23.** Cell proliferation assay of produced Mg alloys containing the lowest and the highest concentration of alloying elements compared with pure Mg.

The addition of Zn in Mg alloys increased the cytocompatibility response compared with the Mg-Ca alloys. It can be inferred from the tendency that the increment of the alloying element, i.e. Ca or Zn, has a positive effect on proliferation. This can also be attributed to the corrosion behaviour, in which, as discussed before, pure Mg exhibited a faster corrosion mechanism than the processed alloys did. Moreover, the production of  $H_2$  impairs the proliferation of the cells.

The best alloy in terms of compatibility was Mg-3%Zn, followed by Mg-1%Zn and Mg-0.2%Ca in the last place with only a slightly better response than that of pure Mg.

The positive proliferation of the cells in contact with the degradable Mg-based materials defined the possibility of these alloys being used as degradable biocompatible materials.

The processing of composites combining Mg alloys with bioactive calcium phosphates has a beneficial effect on the mechanical, corrosive and cytocompatible properties [76,77,114]. Therefore, the production of composites with a predesigned architecture can improve the final required properties.

In summary, based on the corrosion and cell proliferation tests, the alloys containing the lowest alloying element (Mg-0.2%Ca and Mg-1%Zn) revealed the best properties. Thus and therefore, these alloys were selected for the manufacturing of interpenetrated Mg-CaP composites.

### 5.2.3. DEVELOPMENT OF INTERPENETRATED Mg/CaP COMPOSITES

After the robocasting of CaP scaffolds and the casting and evaluation of corrosion resistance behaviour of the Mg alloys, the infiltration of the ceramic preforms was carried out by the CAMI technique in the same way as previously described for the Mg/ $\beta$ -TCP composites in **section 5.1**. The combination of materials for the manufacturing of interpenetrated Mg/CaP composites studied below is listed in **Table 3**.

Different infiltration temperatures were tried to investigate the optimal temperature for the infiltration process. The optimal temperature was found at 670 °C. **Figure 24** shows the heating ramp for the infiltration of the ceramic preforms by the processed Mg-based pellets. The time of the infiltration was set to be fast enough for the whole process (~15 min), with the aim of avoiding the chemical decomposition of the CaP in contact with molten Mg.

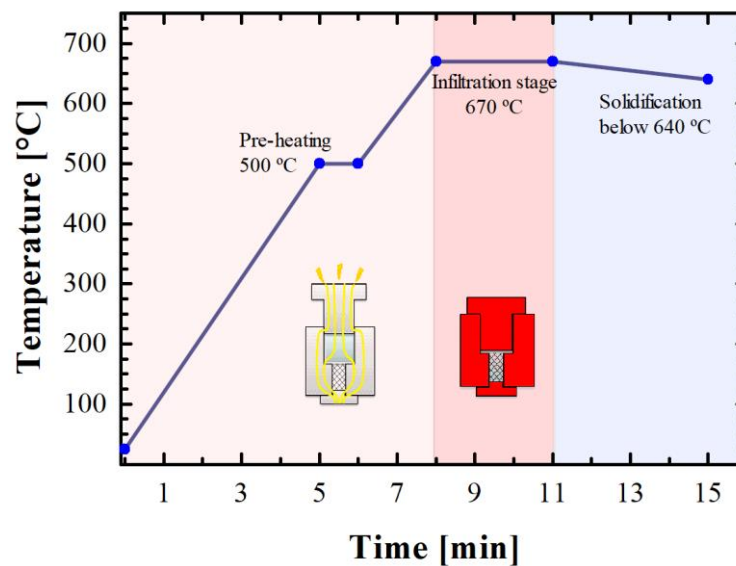


**Figure 24.** Current-assisted metal infiltration (CAMI) temperature ramp processing.

An initial heating ramp was set at below 500 °C as a pre-heating step. Above this temperature, a slower ramp was programmed in order to avoid an overheating on the melting point of Mg and its alloys, which usually caused liquid Mg to escape from the graphite mould. A controlled solidification by cooling down to 630 °C was used to avoid grain coarsening and to eliminate infiltration defects inherent to the molten Mg casting, which detrimentally affect the final properties of the processed materials [115].

After the infiltration, some samples were longitudinally cut to analyse the quality of the infiltration. A visual examination of the longitudinally cut samples revealed a reaction between the ceramic phases and molten Mg. A change in the colour of the ceramic strands indicated that their interaction with Mg triggers the reduction reaction of the calcium phosphates preforms, as previously observed in the Mg/ $\beta$ -TCP composites, forming MgO and decomposing the phosphate group. This reaction has been registered before in the literature but it has not been described extensively; investigations presumed the formation of gaseous phosphorous compounds such as phosphine (PH<sub>3</sub>) [116]. For example, the reaction between pure Mg and  $\beta$ -TCP has been recorded between 520 °C and 534 °C as an exothermic phenomenon involving an abrupt mass loss due to the decomposition of the CaP ceramic [95].

The decomposition of CaP can follow different mechanisms, all of them initiated by the Mg-assisted reduction of the phosphate groups (PO<sub>4</sub><sup>3-</sup>) to form magnesium oxide plus either a solid phosphorous allotrope (P<sub>4</sub>) or phosphide compounds such as calcium phosphide (Ca<sub>3</sub>P<sub>2</sub>) or magnesium phosphide (Mg<sub>3</sub>P<sub>2</sub>).

The phosphide group is highly reactive with air forming phosphine gas (highly toxic) and leaving the cation in a metallic phase instead. In any case, metallic calcium is free to be dissolved in the Mg-based phase, promoting the precipitation of Mg<sub>2</sub>Ca intermetallic due to the excessive amount of Mg compared with the calcium amount. Moreover, the presence of any phosphorous-based compound was accompanied by a smell of garlic, which is characteristic of the P<sub>4</sub> oxidation or the formation of PH<sub>3</sub>.

The garlic smell in the final composites was especially pronounced in the samples produced with the synthesised  $\beta$ -TCP preforms. After their visual examination, these interpenetrated composites were discarded from further characterization due to the presence of many imperfections in the final infiltrated samples, which apart from having a change in the colour of the ceramic phase (yellowish) presented a strong garlic smell even a long period after the infiltration. This effect was not so evident for the composites formed with HA and CDHA preforms, which were the final interpenetrated Mg/CaP composites fully characterized in this study.

The high reactivity of the  $\beta$ -TCP preforms compared with the other calcium phosphates could have been increased by the presence of CDHA phase with a smooth surface that allowed the wettability of chemically reactive CDHA scaffolds with molten Mg. Also, the reactivity of the

synthetic  $\beta$ -TCP obtained by the soft chemistry methodology is different to the commercial  $\beta$ -TCP powder (VWR) used in **section 5.1**, which in fact also revealed some degree of degradation of the ceramic phase and precipitation of the  $Mg_2Ca$  intermetallic (**Figure 14**).

The low reactivity of the HA and CDHA preforms can mostly be caused by two reasons: firstly because of the chemical stability of the compounds, and secondly, due to the microstructure of the preforms.

From this point of view, stoichiometric HA is more chemically stable but even though in some samples a visual reacted surface was observed by a change in colour (from initial bluish to sort of reddish). In addition, the garlic smell was not strong over the time and the integrity of the HA preforms was generally maintained after the infiltration by molten Mg.

In the case of the CDHA structures, the chemical reactivity could be higher than with stoichiometric HA due to calcium deficiency. Nevertheless, the microstructure of the samples played an important role. The roughness in the topography of the preforms reduced the wettability by molten Mg, and the reaction was therefore not as severe as in the case of the  $\beta$ -TCP preforms, which had a smooth surface after the sintering processing.

The microstructure of the initial HA and CDHA scaffolds was observed by SEM and shown for comparison in **Figure 25a-b**. A close-up in the microstructure of the strands that form the preforms revealed that the HA bodies consisted of equiaxial polyhedral grains with some remaining intergranular porosity (**Figure 25a**). On the other hand, the surface of the CDHA preforms consisted of radiating plate-like crystals (**Figure 25d**), which is characteristic after the hydrolysis of  $\alpha$ -TCP ceramics [100,117]. This microstructure provides higher roughness compared with the sintered HA and it is most likely the reason for the low interaction of the CDHA preforms with the molten metal phase during the infiltration.

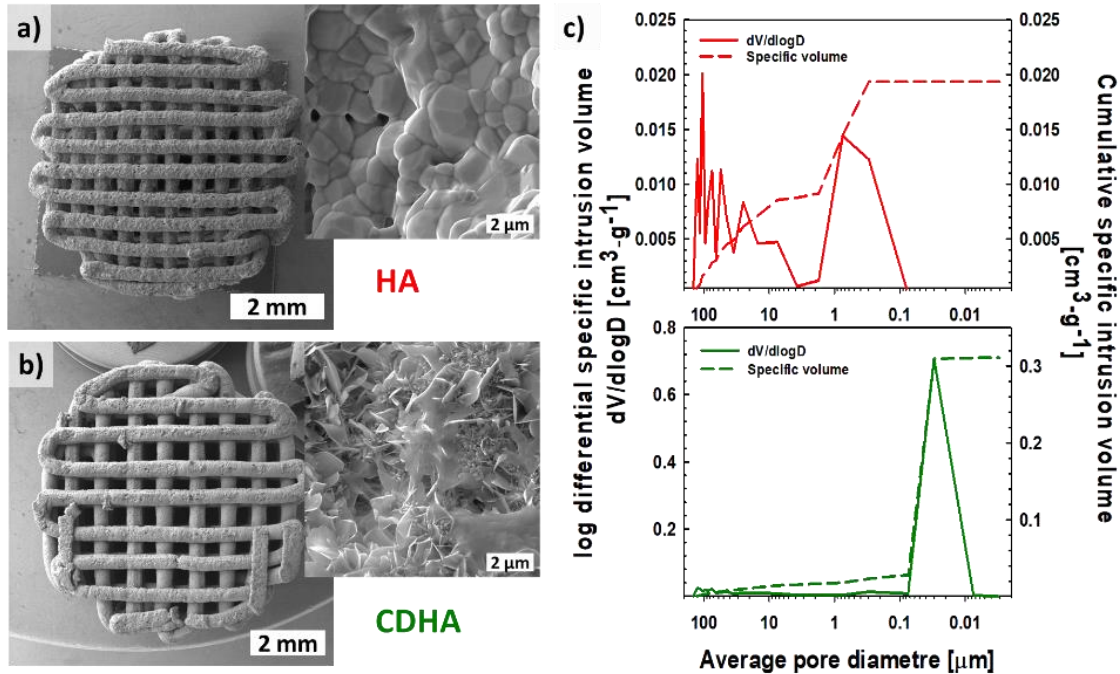


**Figure 25.** Characteristic HA and CDHA structures. (a) Top view of a HA preform after sintering and its characteristic microstructure; (b) Top view of a CDHA preform and its characteristic microstructure; (c) pore-size distribution of the HA and CDHA preforms measured by mercury intrusion porosimetry.

Additionally, the pore size distribution measured by mercury intrusion porosimetry verified the difference in size of the pore channels between the sintered HA and the CDHA preforms. The HA scaffolds had a wider pore size distribution, which was ranging between 10-150  $\mu\text{m}$ , which are values related to the size of the macro-pore channels. The CDHA preforms did not reveal any presence of big pores because the main pore channels were above the detection limit of the technique ( $\sim 483 \mu\text{m}$ , **Table 7**). In terms of the porosity below 1  $\mu\text{m}$ , the sintered HA samples presented a mean pore diameter of 30-75 nm; the CDHA scaffolds, due to their fine microstructure, possessed smaller pore diameters of about  $\sim 30 \text{ nm}$  (**Figure 25c**).

The physicochemical properties of the CaP preforms allowed understanding their reactive interaction with molten Mg-based alloys. The interpenetrated composites manufactured by CAMI, except from the  $\beta$ -TCP-based composites, were utilized for further full characterization as potential degradable biomaterials.

In order to evaluate the quality of the infiltration, random samples of the diverse Mg/CaP interpenetrated composites were taken for the  $\mu$ -CT reconstruction. Representative images of the Mg/CaP composites from  $\mu$ -CT are shown in **Figure 26**.

The high quality of the infiltration by CAMI was evident in all the cases. In general, a total porosity of about 1 vol. % was registered in the interpenetrated composites.

In addition, via the image reconstruction analysis it was found that the integrity of the scaffolds after the infiltration was preserved in the majority of the ceramic preforms. HA scaffolds showed more fractures after CAMI than the CHDA-based composites did. The reasons for this behaviour could be the smaller diameter of the HA strands together with the smaller pores, which need a higher pressure to be infiltrated, as stated by Darcy's law (**Eq. 11**). Therefore, as the stress is increased during the HA preform infiltration, the thin ceramic strands cannot bear the load that the molten Mg exerts on them and consequently they fracture, destroying the sintered preform.

Interpenetrated composite	Transversal section	Longitudinal section	Infiltration degree [%]	Phase volume % ceramic	metallic
Mg/HA			99.8	43.1	56.7
Mg/CDHA			98.0	56.4	41.6
Mg-0.2%Ca/HA			99.4	45.3	54.1
Mg-0.2%Ca/CDHA			99.2	54.6	44.5
Mg-1%Zn/CDHA			97.9	48.4	49.6



**Figure 26.** Image reconstruction made from X-ray computed tomography of Mg/CaP interpenetrated composites together with the calculated degree of infiltration and volumetric phase percent.

The  $\mu$ -CT reconstruction also allowed estimating the volumetric percentage of the ceramic and metallic phases. Due to the dissimilarity in the dimensions of the ceramic preforms, the sintered HA preforms constituted around 44 vol. % of the total volume of the interpenetrated composites, while the hydrolysed CDHA structures constituted around 53 vol. % of the composites. This represents a difference in the metallic/ceramic phase ratio of  $\sim 0.4$  between the HA-based and CDHA-based interpenetrated composites. This difference in the metallic/ceramic phase ratio certainly caused a variance in the performance of the Mg/CaP interpenetrated composites and it is discussed in the further sections.

No sign of a new phase formation from the reaction between the ceramic and molten metal phases was distinguished either in the reconstructed  $\mu$ -CT images or in X-ray diffraction analyses of the interpenetrated composites (**Figure 27**). Only characteristic peaks from the HA-based preforms and Mg-based alloys were detected.

For the composites formed with HA scaffolds, the peak intensity of the ceramic phase was found to be higher than that for the CDHA-based composites. This is due to the metallic phase covering the presence of the nanostructured ceramic preform, which as observed previously exhibited a non-crystalline pattern (see **Figure 18d**).

Important information obtained from the XRD patterns was that during the cooling of the molten Mg, this crystallises in a preferable plane orientation with an excessive grain growth, as previously observed in the Mg/ $\beta$ -TCP composites (**Figure 14a**). This consolidation process probably happens due to the different temperatures of the liquid metal and the ceramic preform and it is most likely different for each sample.

The grain growth of the metallic phase is detrimental for the corrosion and mechanical behaviour of the composites and it represents an issue that should be studied in more detail to discover the way to prevent it in order to homogenise the microstructure of further metal-ceramic interpenetrated composites.

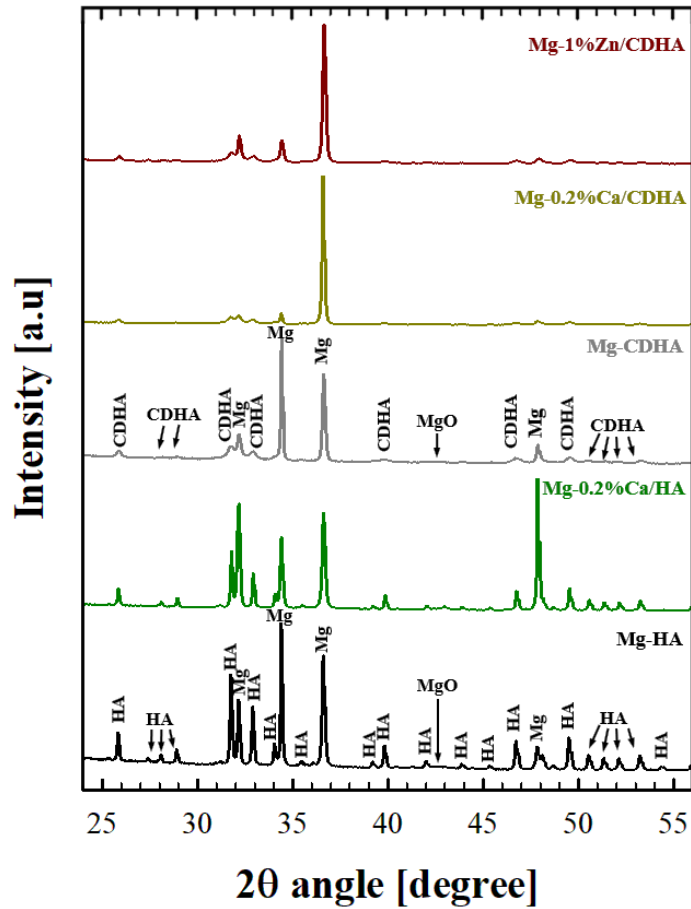


**Figure 27.** Representative X-ray diffraction patterns of interpenetrated Mg-based composites (Mg/HA and Mg/CDHA).

The image analyses of the internal Mg/CaP by SEM were carried out by slicing samples of the interpenetrated composites. **Figure 28** shows typical micrographs of infiltrated HA preforms with pure Mg and Mg-0.2%Ca alloy. The HA structure revealed a high amount of internal porosity that was not infiltrated by the molten metal during the CAMI process. Cracks were also observed in the HA phase; the origin of these cracks is unknown but it is mostly attributed to the CAMI process.

Only a small interface of ~200 nm in thickness between HA and Mg was found in the HA-based interpenetrated composites, confirming a good connection between both phases.

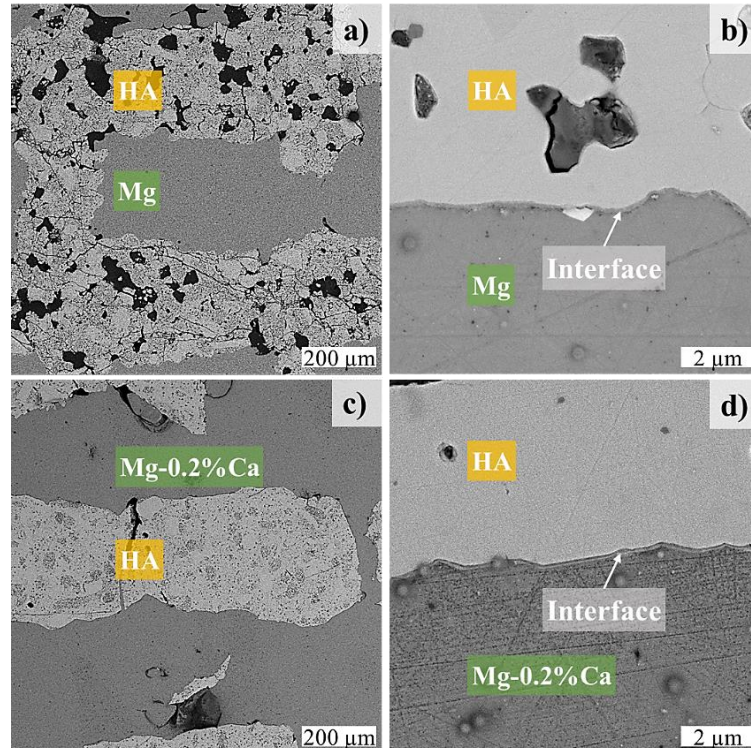


**Figure 28.** Representative micrographs of typical interpenetrated HA-based composites with pure Mg and Mg-0.2%Ca alloy: a) Mg/HA; b) detail of the interface between HA and Mg; c) Mg-0.2%Ca/HA composite; d) detail of the interface between Mg-0.2%Ca and HA.

In general, the infiltration of HA preforms was successful in the macro-channels of the ceramic structures, but because of the brittle nature of the ceramic filaments, many cracks and disintegration of the HA bodies were found within the HA-based composites.

In the case of the CDHA preforms, the interpenetrated composites were more homogeneous along the samples, and the ceramic phase kept its integrity through the molten Mg infiltration, probably due to the bigger strands' diameter.

As in the case of HA structures, the remaining inner porosity was present in the robocast CDHA preforms after their infiltration (**Figure 29**). Comparing the produced interface in the Mg/CaP composites, the reactivity of the CDHA with molten Mg was found to be higher than in the case of HA. The thickness of the interface between the Mg-based phases and the CDHA was in the range of several hundred nanometres up to  $\sim 10 \mu\text{m}$ , which was larger than the interface formed with the stoichiometric HA composites. This interaction of the molten Mg with the CDHA

preforms occurred despite the flake-like microstructure, which was previously assumed to decrease the wettability, reducing the interaction between the phases.

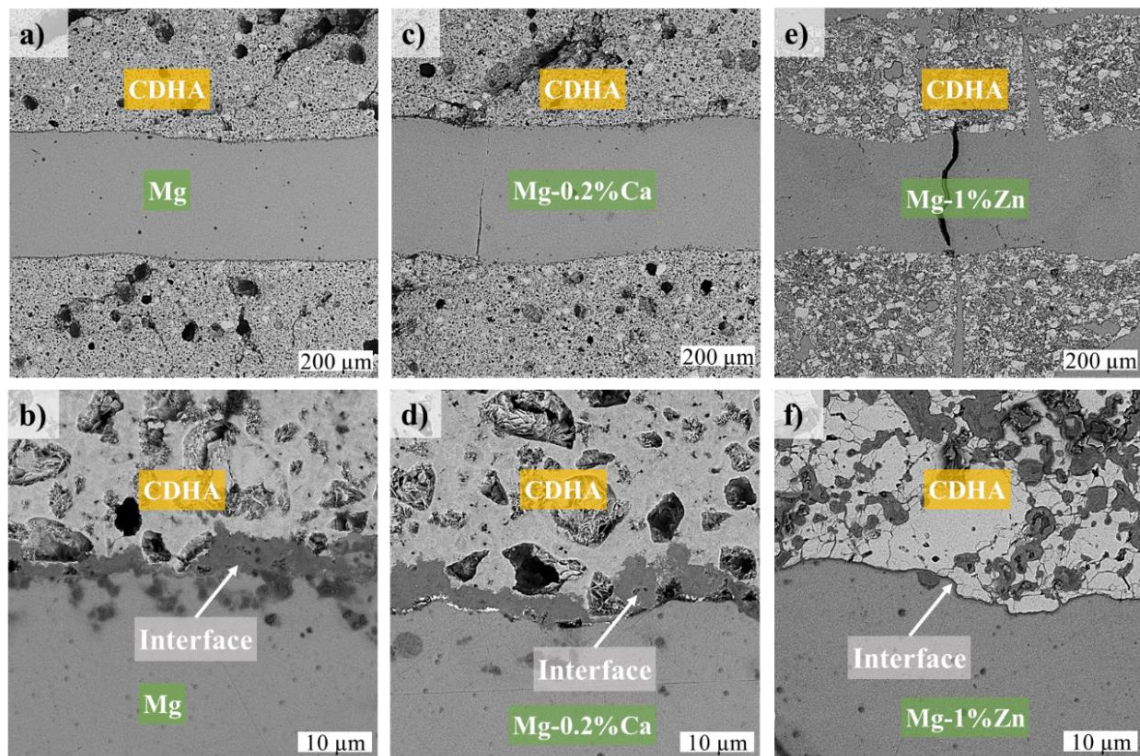


**Figure 29.** Representative micrographs of the interpenetrated CDHA-based composites with different Mg alloys: a) Mg/CDHA; b) detail of the interface between CDHA and pure Mg; c) Mg-0.2%Ca/CDHA; d) detail of the interface between CDHA and Mg-0.2%Ca alloy; e) Mg-1%Zn/CDHA; and f) detail of the interface between CDHA and Mg-1%Zn alloy.

The Mg alloy containing 1 wt.% of Zn showed a smaller interface area (**Figure 29f**) compared with the other metallic counterparts. Contradictorily, this alloy provided better infiltration, filling the inner porosity of the CDHA filaments and sometimes causing the origin of cracks within the ceramic structure (**Figure 29e-f**). This showed a preferable affinity between the calcium phosphate phase and the Mg when the latter is doped with zinc. Molten Mg-Zn alloys have been reported to be excellent reductants in the case of CO<sub>2</sub> and graphene oxide to produce graphene, which is a property that could also enhance the CaP decomposition [118,119].

In the majority of the produced samples, the molten metal was unable to penetrate the inner open porosity within the filaments during the infiltration process. However, in some cases, where the pore size was considerably big or when cracks were present in the preform, the liquid Mg

infiltrated and filled those defects. In addition, the infiltration produced an interface connection between the ceramic and the metallic phases, which is related to the affinity between the calcium phosphates and the Mg-based alloys. This contact between the phases could be beneficial or detrimental to the final properties, especially the mechanical properties of the composites. The good bonding between the former materials of the composite relies on the chemical composition, microstructure and thickness of the interface [120].

The connection between the ceramic and the metallic phase (interface) is highlighted for the Mg-0.2%Ca/CDHA composite in **Figure 30a**; an SEM micrograph together with a lineal EDX analysis showed that the interface between the Mg and the calcium phosphates consisted predominantly of magnesium and oxygen. Also, as a product of the chemical affinity between the CaP and molten Mg, the reduction of the CaP phase led to the dissolution of calcium ions into the Mg matrix, causing the precipitation of the eutectic Mg-Mg<sub>2</sub>Ca phase (**Figure 30b-c**).

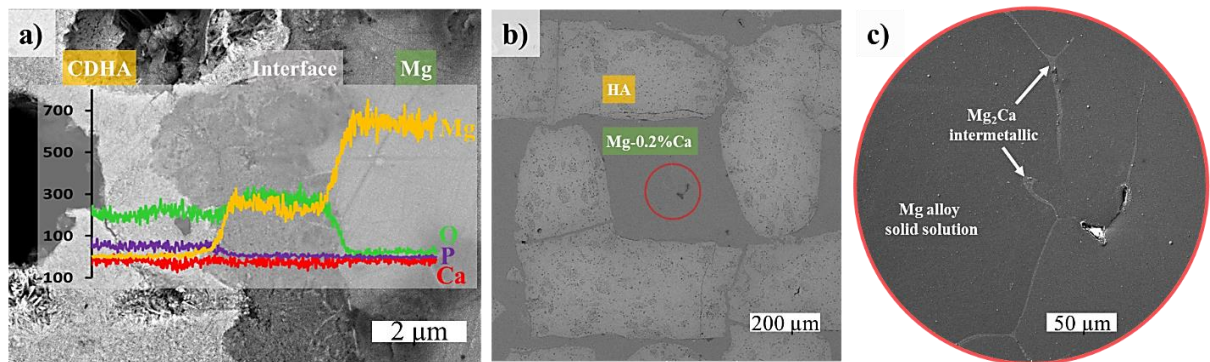


**Figure 30.** a) Lineal EDX chemical analysis on typical interface between Mg and CaP, interface from Mg/CDHA composite. b) Representative micrograph of interpenetrated composites, Mg-0.2%Ca/HA with Mg<sub>2</sub>Ca intermetallic phase; and c) detail of Mg phase pointing out the Mg<sub>2</sub>Ca intermetallic as a product of the reduction of the CaP phase.

A local EDX chemical analysis was performed in order to compare the chemical composition at the interface of all the interpenetrated composites. The results are summarized in atomic percent in **Table 10** and demonstrate the highest concentration of Mg and O. Based on the stoichiometry, the presence of MgO was presumed to be the predominant compound with some small concentration of calcium and phosphorus (most likely from the adjacent CaP structure).

**Table 10.** Chemical composition of the interface in the Mg/CaP composites

<b>Mg/CaP interpenetrated composite</b>	<b>Mg [at. %]</b>	<b>O [at. %]</b>	<b>Ca [at. %]</b>	<b>P [at. %]</b>
<b>Mg/HA</b>	56.1	31.3	6.1	5.8
<b>Mg/CDHA</b>	40.7	53.7	2.7	2.2
<b>Mg-0.2% Ca/HA</b>	32.2	40.8	17.2	9.1
<b>Mg-0.2% Ca/CDHA</b>	38.0	57.3	2.0	2.2
<b>Mg-1% Zn/CDHA</b>	44.9	45.0	4.4	4.8

The formation of MgO in the interface between Mg and the CaP was found to be beneficial to the mechanical properties of highly dense Mg/ $\beta$ -TCP composites. This is because the high hardness of MgO provides good load transfer from the Mg phase to the produced MgO layer [95]. However, the MgO interface formed in the interpenetrated Mg/CaP composites was not of high densification, it rather exhibited some porosity that was linked to the topography of the HA and CDHA preforms. This interface would play an important role in the mechanical and degradation properties of the composites, as discussed in the following sections.

### 5.2.3.1. MECHANICAL BEHAVIOUR OF INTERPENETRATED Mg/CaP COMPOSITES

A comparison of the mechanical behaviour of the Mg/CaP interpenetrated composites is summarized in **Table 11**. The mechanical properties were calculated from the stress-strain curves obtained by compression test.

**Table 11.** Compressive mechanical properties of interpenetrated Mg/CaP composites and the initial constituents.

<b>Material</b>	<b>Yield strength [MPa]</b>	<b>Ultimate compression strength, <math>\sigma_{max}</math> [MPa]</b>	<b>Deformation [%]</b>
<b>HA preform</b>	0.2±0.04	2.3±0.6	<0.2
<b>CDHA preform</b>	2.8±0.25	6.4±1.6	<0.8
<b>Mg</b>	154.3±31.2	172.9±23.8	27.1±4.7
<b>Mg-0.2% Ca</b>	164.8±6.4	358.5±2.4	19.5±0.1
<b>Mg-1% Zn</b>	103.6±2.8	336.1±7.4	17.7±0.3
<b>Mg/HA</b>	70.9±5.9	116.2±9.1	13.7±3.1
<b>Mg-0.2% Ca/HA</b>	60.8±8.6	119.2±32.7	14.8±1.6
<b>Mg/CDHA</b>	25.2±3.3	48.2±6.6	16.4±1.0
<b>Mg-0.2% Ca/CDHA</b>	23.9±1.8	40.9±5.1	13.9±1.5
<b>Mg-1% Zn/CDHA</b>	23.3±3.4	49.6±7.8	15.5±1.0

The initial porous preforms presented a very low mechanical strength, which is typical for porous ceramics. This low mechanical strength is the main limitation for ceramic scaffolds in load-bearing applications [121–123].

CDHA preforms exhibited a better mechanical performance than the HA preforms did. Two main reasons can be taken into account as potential explanation: first, the difference in microstructure after the consolidation process [124], and second and most significant, the difference in the dimensions of strands that form the cylindrical preforms [125]. Thus, in the case of the sintered HA preforms, the final dimensions were shorter than those of the CDHA bodies. Consequently, the CDHA preforms possessed a larger loading surface-area based on the bigger diameter of the strands, and slightly bigger general dimensions (**Table 4**).

In the case of the initial magnesium alloys, the mechanical behaviour was similar for all of the samples. The Mg alloys had an average ultimate compressive strength of about 350 MPa, which was twice that of the pure Mg (~173 MPa).

On the other hand, the yield strength revealed a larger difference between the alloys. Mg containing 1 wt. % of Zn showed a rapid plastic deformation compared with its counterpart alloy containing 0.2 wt. % of Ca, which exhibited a larger region of elastic deformation.

The different mechanical response of the Mg-based phases is attributed to the refining effect. The doping of Mg with a low content of Ca produced a greater grain-refining effect than the addition of Zn below their solid solubility limit (**Annex 2**). This explains the higher mechanical properties of the Mg-Ca and Mg-Zn alloys over the pure Mg.

Reports about the toughening of Mg alloys as an effect of grain refinement are widely known for Ca and Zn. Even above the solid solubility limit, both Ca and Zn increase the strength and the elongation rate of Mg alloys not only by the grain refinement, but also by the formation of intermetallic phases that are distributed along the grain boundaries [126]. The concentration of Ca above 1 wt.% in Mg-Ca alloys is detrimental due to the precipitation of a high volume fraction of Mg<sub>2</sub>Ca intermetallic particles that deteriorate the ductility and the corrosion resistance [127,128]. On the other hand, a Zn addition of up to 5 wt.% has a beneficial effect on the mechanical performance of the alloy by promoting the precipitation of MgZn intermetallic phases. Moreover,

a network-like distribution of the intermetallic phases deteriorates the deformation rate and promotes galvanic corrosion [129].

Beside the alloying effect of the Mg alloys, the plastic deformation during the extrusion processing enhanced the mechanical properties of the alloys. It is well known that the mechanical properties of most metals can be improved by refining the microstructure, and Mg is not an exception as regards this microstructural effect.

Several approaches to the grain refinement in Mg and its alloys, e.g. plastic deformation, heat treatment, and forming processing, have pointed out the benefits of a fine-grain microstructure to the mechanical properties of processed Mg-based materials [130–132]. This grain refinement by extrusion was yet another cause of the final microstructure of the cast and extruded initial Mg alloys (**Annex 2**).

The interpenetrated Mg/CaP composites exhibited mechanical properties whose values were between those of their former constituents (**Figure 31**). This behaviour reflects the good connection between the metallic and ceramic phases, which was previously assumed to be due to the formation of the MgO interface and previously registered for sintered Mg/ $\beta$ -TCP conventional composites [95].

Generally and despite the fact that the mechanical properties of the initial preforms showed contradictory behaviour, the composites constituted of HA preforms exhibited a higher strength than the CDHA-based composites did. Thus, Mg/HA and Mg-0.2%Ca/HA interpenetrated composites exhibited almost twice the yield and compressive strength of their CDHA-based counterparts (**Figure 31** and **Table 11**).

Interestingly, the set of the HA-based interpenetrated composites were of analogous mechanical properties. The same behaviour was observed for the set of composites based on CDHA (**Figure 31**). This behaviour indicates that the mechanical properties of the Mg/CaP interpenetrated composites are predominantly governed by the ceramic phase nature and they are not significantly dependent on the Mg composition. This minor dependence of the metallic phase on the mechanical properties can be attributed to the coarse microstructure of this phase, which was found to be similar for all the Mg/CaP composites.

As stated by the Hall-Petch relation, a coarse grain microstructure is detrimental to strength [133], as could be observed for the pure Mg source compared with the cast and extruded alloys. However, the Mg-1%Zn alloy revealed a lower yield strength than pure Mg did. This effect has not been reported before, on the contrary, the addition of Zn tends to increase the tensile yield strength of the Mg-Zn alloys. Despite this low-limit elastic stress, the Mg-1%Zn alloy revealed a substantial higher compressive strength compared to the pure Mg (~336 MPa vs ~173 MPa), similar to what was reported previously by other authors [129,134].

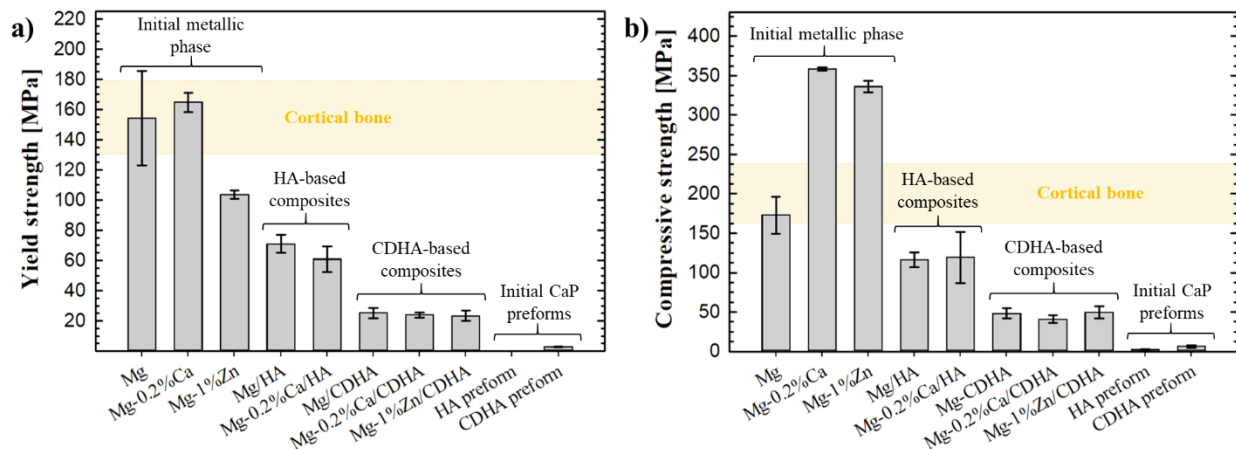


**Figure 31.** Room-temperature compressive mechanical properties of initial Mg alloys, CaP preforms, and processed interpenetrated composites: a) yield strength and b) ultimate compressive strength.

Despite the low strength of the Mg/CaP interpenetrated composites compared with the initial metallic phases, the infiltration of the ceramic scaffolds with Mg-based alloys provided a significant increase in the mechanical response of the infiltrated preforms and gave engineering strain to the composites (**Figure 32**). While the consolidated CaP preforms supported a maximum load of a few mega pascals, i.e. ~2 MPa for HA, and ~8 MPa for CDHA (**Figure 32d**), the interpenetrated composites bore an engineering stress of ~50 MPa for the case of the CDHA-based composites and ~120 MPa for the HA-based ones (**Figure 32a-c**).

An inspection of the fracture surface of the Mg/CaP composites (**Figure 32e-f**) revealed that the failure mechanism relies on the chemical composition and/or morphology of the CaP preforms. For HA-based composites, the failure of the specimens occurred due to the cracking of the ceramic preform (**Figure 32e**), whereas the CDHA-based composites failed predominantly by cleavage at the MgO interface between the ceramic preform and the metallic phase (**Figure 32f**).

This behaviour exposed the role of the interface thickness in the Mg/CaP composites; therefore, when the interface is large enough, the mechanical properties are more compromised by the fragility of the non-consolidated MgO layer than by the strength of the consolidated CaP phase. From this point of view, it can be inferred that the bonding force of the MgO interface is weak and thus the chemical reaction between Mg and CaP must be avoided.

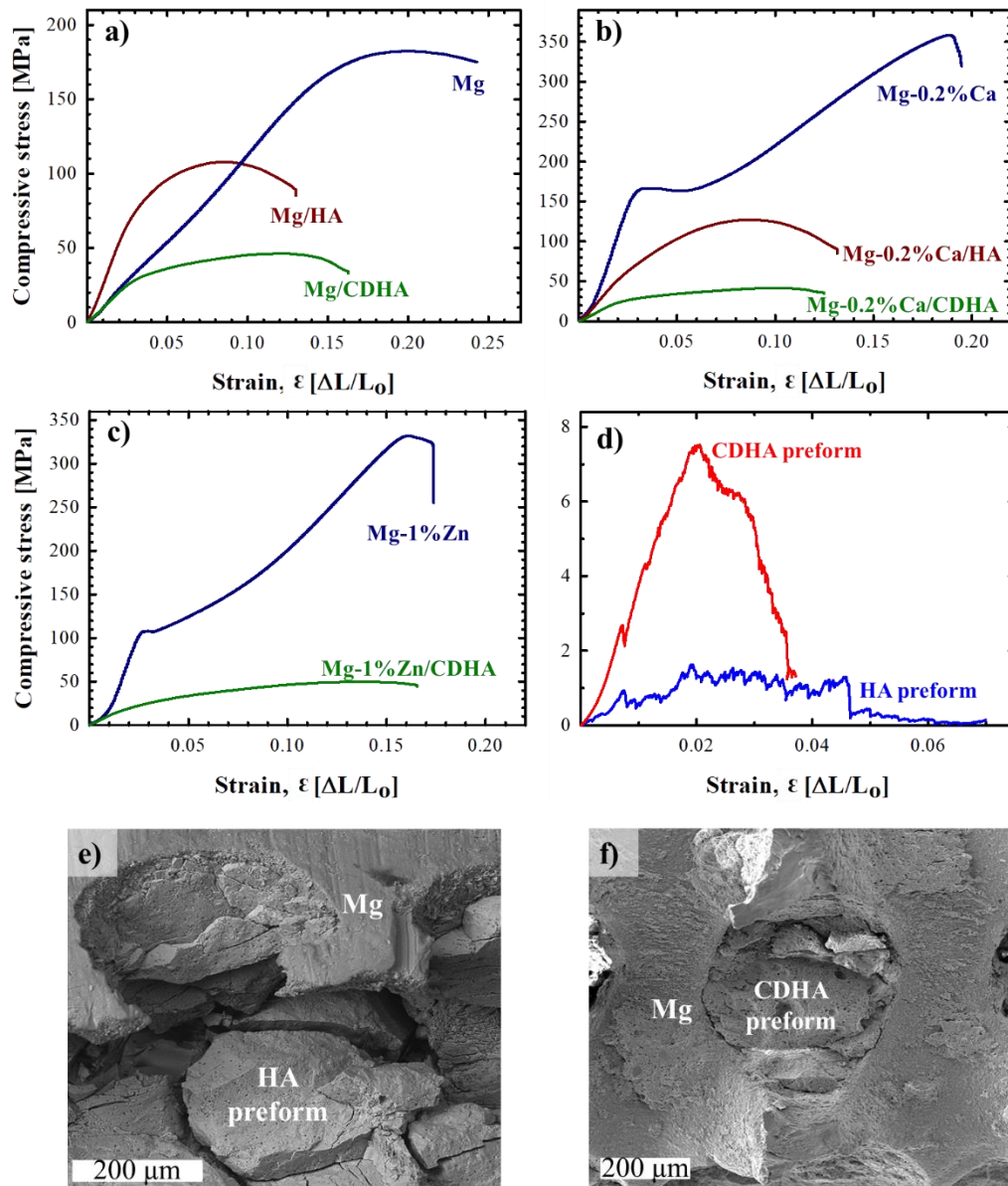


**Figure 32.** Representative stress-strain curves at room temperature from the compression test of interpenetrated Mg/CaP composites: a) Pure Mg-based composites; b) Mg-0.2%Ca-based composites; c) Mg-1%Zn-based composites; d) initial CaP preforms; e) typical fracture surface in HA-based composites; and f) typical fracture surface in CDHA-based composites.

In general, the best-interpenetrated composites in terms of the mechanical properties were the Mg-0.2%Ca/HA, followed by the Mg/HA composite. These two interpenetrated composites exhibited an average deformation of ~14% and a compressive strength of almost 120 MPa. These results are in agreement with other Mg/CaP composites manufactured by liquid infiltration reported in the literature, where the values of compressive strength varied between ~70–150 MPa and possessed an average deformation between 8-18 % [81–83,135–137].

Unfortunately, the mechanical properties of the interpenetrated Mg/CaP composites are below the prime requirements for cortical bone replacement (see **Figure 31** and **Annex 1**). However, the ductility and compressive strength exhibited in these structured composites makes them still suitable in orthopaedic applications where the load does not exceed the mechanical limits of the specimens, for example in the manufacture of plates and/or screws for bone fixation of non-weight-bearing zones or articulations, or in cancellous bone regeneration [138,139]. Additionally, one of the main advantages of these Mg/CaP composites over the current materials for bone fixation, such as stainless steel, is not only the degradation but also the very low stress-shielding effect that this light composites can provide during bone healing [140].

There are two main factors that can help to increase the mechanical properties of the interpenetrated Mg/CaP composites: (1) optimization of the CAMI process to reduce the chemical reaction between Mg and the CaP; and (2) control of a fine microstructure in the metallic phase.

Moreover, another advantage of the interpenetrated composites is that the mechanical response can be tailored by the geometrical distribution of the phases and/or by varying the metallic/ceramic phase ratio as it was observed between the Mg/HA and Mg/CDHA composites. This statement is one of the highlights of this type of composites presented here because in difference to other produced composites where the reinforcement phase is randomly distributed, in the architecture developed here, the phases are arranged in a predesigned pattern that can be modified to produce different distributions with diverse mechanical properties. All of this has been modelled for fibre-reinforced composites demonstrating that beside the volume fraction, the shape and orientation of the reinforcements and the distribution of them play a substantial role in the mechanical properties of composites [141,142].

### 5.2.3.1. CORROSION RESISTANCE OF INTERPENETRATED Mg/CaP COMPOSITES

In terms of corrosion resistance, the produced interpenetrated composites exhibited different behaviour. The measurements of the degradation rate were carried out primarily by H<sub>2</sub> evolution and potentiodynamic polarization measurements. The selection of these two techniques was based on the fact that monitoring the produced hydrogen during the corrosion of Mg offers a reliable corrosion profile over a prolonged period of time. On the other hand, the electrochemical measurement provides knowledge of the initial corrosion mechanism and reaction kinetics for physiologically realistic media [111,143,144].

The corrosion rate of the different composite systems estimated by H<sub>2</sub> evolution during 14 days under physiological conditions (immersion in SBF at 37 °C) are summarized in **Table 12**.

**Table 12.** Degradation rate of produced interpenetrated Mg/CaP composites and their metallic counterparts estimated by the H<sub>2</sub> evolution assessment after 2 weeks in SBF at 37 °C.

Material	Corrosion rate [mm·year <sup>-1</sup> ]
Pure Mg	4.24 ± 0.29
Mg/HA	3.69 ± 1.67
Mg/CDHA	5.62 ± 3.80
Mg-0.2%Ca	2.88 ± 0.18
Mg-0.2%Ca/HA	11.12 ± 2.30
Mg-0.2%Ca/CDHA	4.87 ± 0.53
Mg-1%Zn	1.90 ± 0.66
Mg-1%Zn/CDHA	5.90 ± 2.59

In general, the interpenetrated composites had a faster corrosion rate than the Mg-1%Zn and Mg-0.2%Ca alloys, which were in the range of 2–3 mm·year<sup>-1</sup>. Furthermore, the bare alloys presented almost twice the corrosion resistance of pure Mg, as expected from the difference in the grain size microstructure [111].

The best interpenetrated composite in terms of its corrosion resistance was found in the Mg/HA material with an average corrosion rate of 3.69 mm·year<sup>-1</sup> (estimated by H<sub>2</sub> evolution test). On the other hand, the fastest degradation rate was registered for the Mg-0.2%Ca/HA composite with a degradation rate of above 11 mm·year<sup>-1</sup>, followed by all the composites composed by the infiltrated CDHA structures. This set of CHDA-based composites exhibited similar corrosion rates of about 5 mm·year<sup>-1</sup>.

The wide range of the corrosion profile is due to several factors: (1) the grain size of the metallic phase was increased during the non-controlled solidification during the CAMI process; (2) the effective surface area of the metallic phase in the interpenetrated composites varied from sample to sample; and (3) the porosity of the CaP ceramic phase and MgO interface could act as absorbent channels, allowing the corrosive medium to reach the inner metal phase of the composite, consequently increasing the corrosion rate values.

The assessment of the H<sub>2</sub> production also allowed recognizing the changes in the corrosion mechanism along the first two weeks under simulated physiological conditions (**Figure 33a-c**). All the interpenetrated composites and initial Mg alloys reached a constant corrosion rate after the 5<sup>th</sup> day of immersion. This effect is common in Mg alloys due to the passivation of the surface by the formation of a protective Mg(OH)<sub>2</sub> layer and the deposition of calcium and phosphorus compounds [110,113,129]. During the second week, the degradation rate got stabilized with only a slight decrease for all materials.

The role of the porous interface and the ceramic phase in the Mg/CaP composites was also visible in the corrosion profiles obtained by the H<sub>2</sub> evolution (**Figure 33a-c**). In general, the pure metals started with a lower corrosion rate compared with their interpenetrated composites. Only the Mg-0.2%Ca/HA composite revealed a slower corrosion rate than the bare Mg-0.2%Ca alloy did. However, after the first 24 hours, most of the composites reached a certain degree of passivation, decreasing the H<sub>2</sub> production to almost half of that at the beginning.

Alternatively, the potentiodynamic polarization test in SBF at room temperature revealed a similar tendency in the degradation rate of the composites to that in the initial profiles registered by H<sub>2</sub> evolution. In the case of pure Mg and its composites, the results revealed that the corrosion potential ( $E_{\text{corr}}$ ) becomes more negative in the following order: Mg/HA  $\leq$  Mg/CDHA < pure Mg. By contrast, the Mg-0.2%Ca and Mg-1%Zn alloys revealed a less negative  $E_{\text{corr}}$  than their interpenetrated composites with HA and CDHA structures (**Figure 33d-e**). The higher negative values in the  $E_{\text{corr}}$  of the composites compared to the Mg alloys is related to a faster corrosion rate [145]. This effect is a consequence of the initial reactivity of the materials, which is increased by the grain size of the metallic phase and the presence of the Mg<sub>2</sub>Ca intermetallic [55,94,144,146].

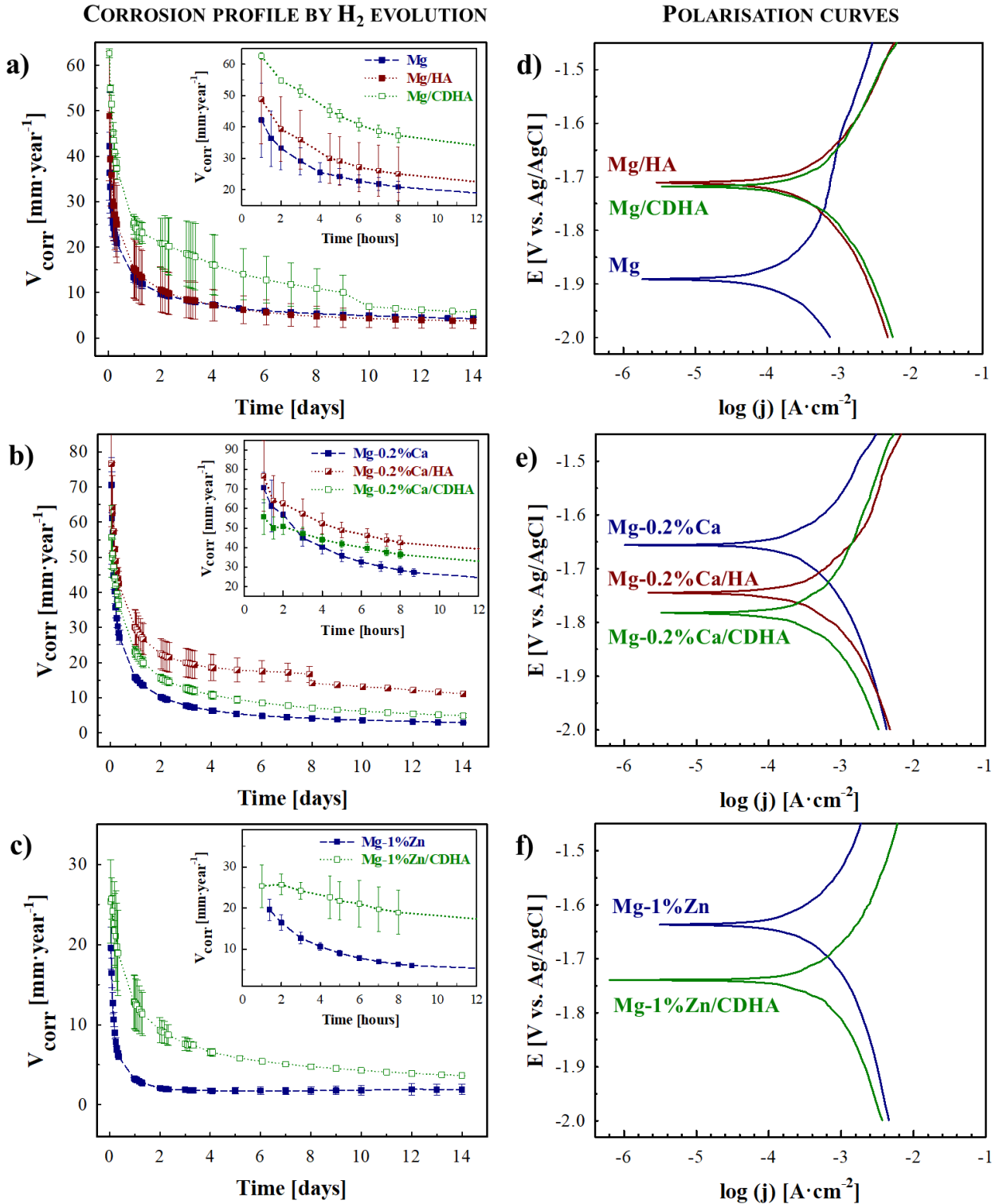


**Figure 33.** Corrosion rate profiles calculated from the H<sub>2</sub> evolution test of: a) pure Mg-based composites; b) Mg-0.2%Ca-based composites; and c) Mg-1%Zn-based composites. Also, characteristic polarization curves of d) pure Mg-based composites; e) Mg-0.2%Ca-based composites; and f) Mg-1%Zn-based composites.

**Table 13** summarizes the corrosion potential, corrosion current density ( $i_{\text{corr}}$ ) and corrosion rate of the different material systems calculated by the Tafel extrapolation of the polarization curves (**Figure 33d-f**) and using Faraday's law (**Eq. 10**).

**Table 13.** Corrosion potential, corrosion current density and degradation rate estimated by the Tafel extrapolation of obtained polarization curves using SBF at room temperature.

Material	Corrosion potential, $E_{\text{corr}}$ (V)	Corrosion current density, $i_{\text{corr}}$ (mA·cm <sup>-2</sup> )	Corrosion rate [mm·year <sup>-1</sup> ]
Pure Mg	-1.89 ± 0.01	0.216 ± 0.00	4.93 ± 0.11
Mg/HA	-1.71 ± 0.05	0.408 ± 0.05	9.33 ± 1.17
Mg/CDHA	-1.78 ± 0.05	0.614 ± 0.15	12.68 ± 2.88
Mg-0.2%Ca	-1.66 ± 0.02	0.371 ± 0.12	8.49 ± 0.11
Mg-0.2%Ca/HA	-1.77 ± 0.07	0.533 ± 0.02	12.20 ± 0.52
Mg-0.2%Ca/CDHA	-1.78 ± 0.02	0.524 ± 0.07	12.00 ± 1.70
Mg-1%Zn	-1.65 ± 0.05	0.358 ± 0.03	8.17 ± 0.68
Mg-1%Zn/CDHA	-1.74 ± 0.01	0.473 ± 0.13	10.80 ± 3.09

The corrosion current density provides information about the cathodic reaction during the Mg corrosion, which is connected to the production of H<sub>2</sub> [111,145,147]. Lower values of  $i_{\text{corr}}$  indicate better corrosion resistance [83,145]. From this point of view, the pure metallic phases revealed lower corrosion current densities, consequently a higher corrosion resistance in comparison to the Mg/CaP interpenetrated composites. This can only be explained by the grain size of the magnesium phase and the presence of the Mg<sub>2</sub>Ca intermetallic [55,94,144–146].

The corrosion rates estimated by the Tafel extrapolation measurements were almost three times higher than the values obtained by the H<sub>2</sub> evolution test after 14 days of immersion. This difference has been previously reported [111,143] and is predominantly influenced by two aspects: (1) the dissimilarity in the time of testing, i.e. 14 days vs. ~2 min; and (2) the difference in the exposed surface area to corrode. This second issue is of high relevance, because while surface areas of around 170 mm<sup>2</sup> were exposed to corrosion in the H<sub>2</sub> evolution test, only 19.6 mm<sup>2</sup> were used in the potentiodynamic polarization technique. Furthermore, in the potentiodynamic polarization, the effective area of the metallic phase was easily calculated by means of image analysis and found to be about 7.5 mm<sup>2</sup> on average.

Despite the variance between the methods for the estimation of the corrosion rate in Mg and its alloys, the combination of them provides a better overview of the degradation resistance of the produced materials. In this sense, H<sub>2</sub> evolution divulges how much corrosion occurs in the course of time, while the potentiodynamic polarization test reveals the mechanism involved in the corrosion process [144].

Consequently, an analysis of the corroded surfaces after the potentiodynamic polarization test was carried out in order to investigate the mechanism that governs the corrosion process in the interpenetrated Mg/CaP composites. In general, all the produced materials exhibited pitting corrosion (**Figure 34**). This type of corrosion is one of the most common corrosion mechanisms for Mg alloys and it is related to chemical composition and microstructural features. Therefore, Mg and its alloys usually become the anode when there are two components or when two different grain sizes exist within the same alloy [111,147].

In the case of the interpenetrated Mg/CaP composites, the pitting corrosion was rather a crevice corrosion (**Figure 34**), preferentially localised along the interface between the ceramic and metallic phases and where the amount of the intermetallic phase tended to increase. This effect has been previously observed for similar interpenetrated Mg/CaP composites based on -TCP+MgO/Zn-Mg and HA+ -TCP/MgCa, where this process is explained to be due to the capability of the interface to create a galvanic couple with the ceramic phase [81,82,148].

The degree to which the surface is pitted as shown in **Figure 34** is congruent with the corrosion rates and microstructure of the materials. Thus, Mg alloys revealed small holes compared with the pure Mg and Mg/CaP composites (all of them with a coarse grain microstructure).

The Mg-0.2%Ca alloy presented a higher concentration of small cavities than the other two metallic phases; this could be explained by the fine grain microstructure of this alloy, which could present the effect of previous reports for ZK60 alloys with two different grain sizes, where the coarse-grain areas are passivated due to their higher open corrosion potential (OCP), while the finer grain zones (with a lower OCP) are favourably corroded [149].

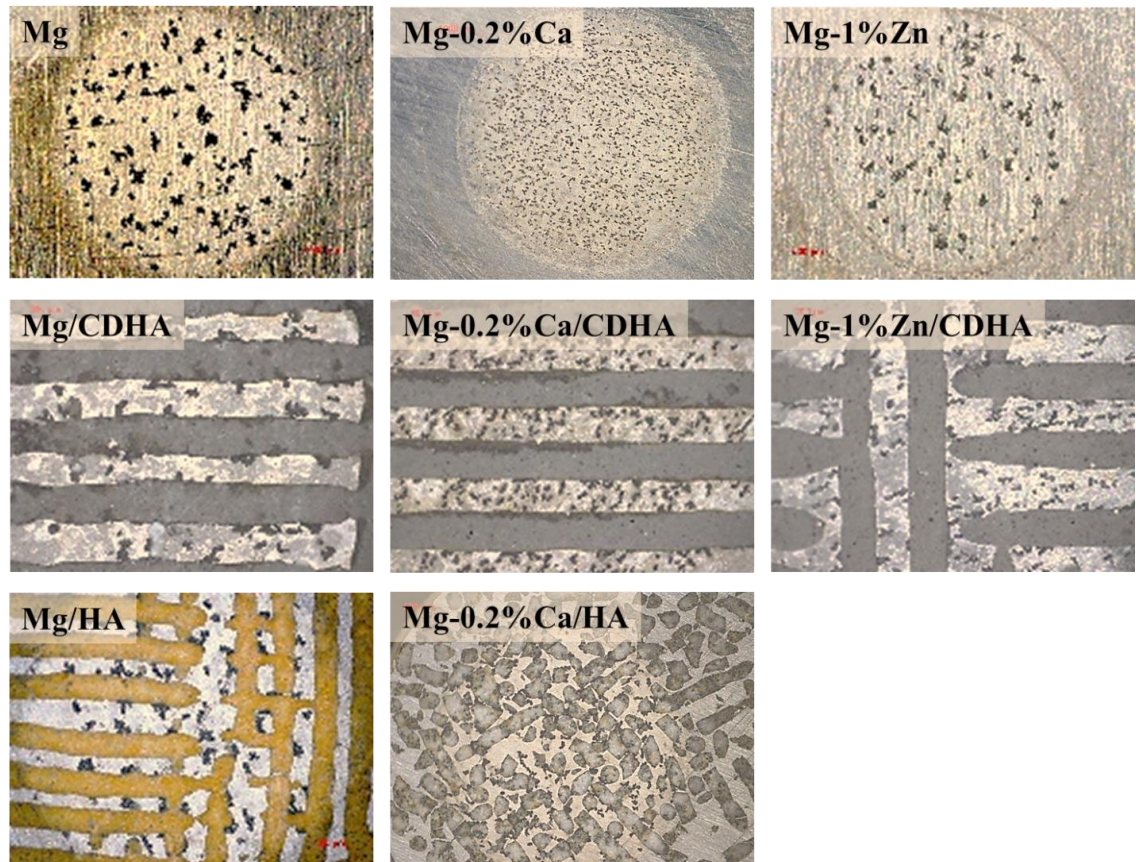


**Figure 34.** Comparison of the corrosion mechanism of initial Mg alloys and different Mg/CaP interpenetrated composites after the potentiodynamic test in SBF at room temperature.

To sum up, the produced Mg/CaP composites revealed a similar corrosion resistance and presented an equal corrosion mechanism. In general, the corrosion rate values of the interpenetrated Mg/CaP composites were slightly higher than the ones found in the literature for similar interpenetrated composites obtained by an infiltration of HA-TCP scaffolds with Mg-1%Ca alloy, with an average corrosion rate of about  $3.4 \text{ mm}\cdot\text{year}^{-1}$  [51,83].

In spite of the fast corrosion rate in the interpenetrated Mg/CaP composites, they exhibited better corrosion resistance than the conventional composites based on Mg and Mg alloys with HA or -TCP particles and produced by powder metallurgy or stirring casting (see **Annex 1**). Such conventional Mg/CaP composites had the drawback of containing free ceramic particles, which revealed corrosion rates in a wide range of  $\sim 1.5\text{-}720 \text{ mm}\cdot\text{year}^{-1}$ , depending on heterogeneous distribution and poor consolidation of the final composite [78,150,151].

### 5.2.3.1. CYTOTOXICITY AND CELL VIABILITY OF INTERPENETRATED Mg/CaP COMPOSITES

The cell viability and cytotoxicity response of the interpenetrated Mg/CaP composites were evaluated under indirect contact with SAOS-2 human cells, previously seeded and adhered to TCPS 96-well plates. The proliferation of SAOS-2 cells in extracts from Mg samples was evaluated by counting the number of cellular nuclei, using the image analysis of each well area after 1, 3 and 6 days of testing.

**Figure 35** shows the proliferation of SAOS-2 cells from the indirect contact with the bare Mg, Mg alloys, and the interpenetrated Mg/CaP composites. The pure Mg revealed a constant number of cells over the time. The Mg-0.2%Ca alloy slightly promoted the cell proliferation after the 3<sup>rd</sup> day of cell culture while the Mg-1%Zn alloy did not reveal any significant difference in the cell proliferation over the testing time (**Figure 35a**).

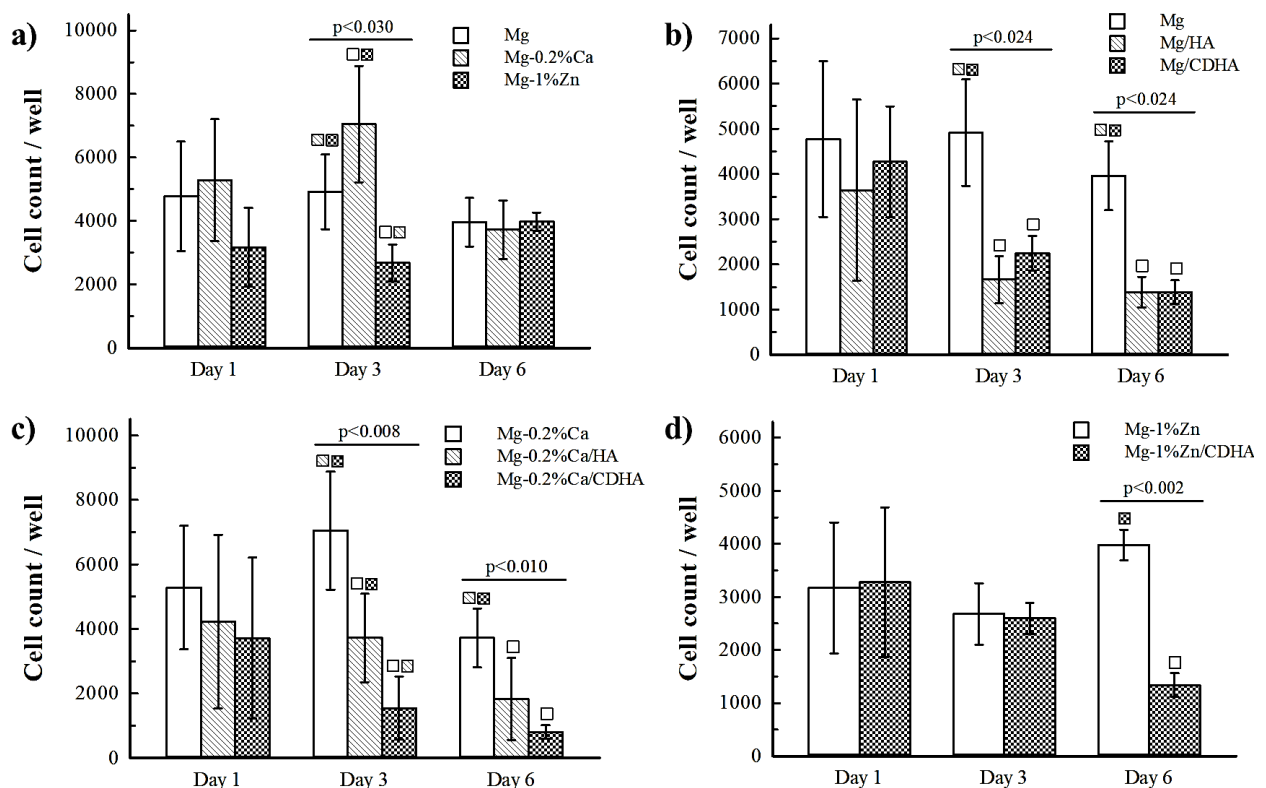


**Figure 35.** SAOS-2-cell proliferation represented as cell count per well. Data are expressed as the mean  $\pm$  S.D. The significant differences between similar sets of samples at particular time points (Mann-Whitney U test;  $p < 0.05$ ;  $n = 8$  per each group) are marked by corresponding group legend pattern.

In the case of the Mg-based composites, the Mg/HA and Mg/CDHA composites had a similar cell proliferation as the pure Mg phase after 24 hours of cell culture. However, the interpenetrated composites revealed a significant and equal decrease in the cell proliferation after the 3<sup>rd</sup> and 6<sup>th</sup> days (**Figure 35b**).

Similarly, the Mg-0.2%Ca/HA and Mg-0.2%Ca/CDHA composites revealed a decrease in the cell proliferation after the 3<sup>rd</sup> and 6<sup>th</sup> days of the test. Nevertheless, the Mg-0.2%Ca/HA composite exhibited a slightly better proliferation effect than the Mg-0.2%Ca/CDHA material over time (**Figure 35c**). The same behaviour was observed in the Mg-1%Zn/CDHA composite, where the proliferation of the SAOS-2 cells gradually decreased after the 3<sup>rd</sup> and 6<sup>th</sup> days of culture (**Figure 35d**).

The decrease in the proliferation is directly connected to the cytotoxic effect of the materials. Thus, the cytotoxicity of the Mg/CaP composites was estimated by means of the cellular viability of live SAOS-2 cells after their contact with the Mg/CaP composites for 1, 3 and 6 days (**Figure 36**).

In agreement with the cell proliferation results, all the Mg alloys and interpenetrated Mg/CaP composites exhibited a cytotoxic effect on SAOS-2 cells after 3 and 6 days of cell culture (**Figure 36a-d**). During the first day of the assay, the only samples without a cytotoxic effect were those of the pure Mg and Mg-0.2%Ca alloy (**Figure 36a**). After the first day of culture, the Mg/HA and Mg/CDHA composites presented a cell viability similar to the control but with a big variation (**Figure 36b**). In general, all the Mg/CaP composites revealed higher cytotoxicity after the 3<sup>rd</sup> and 6<sup>th</sup> days of cell culture in comparison with the bare metallic phases (**Figure 36b-d**).

Previous studies on the cytocompatibility of AZ91D alloy containing HA particles found a strong correlation between the cell viability results and the cell culture procedure or type of cells used in the test [4,83]. Besides that, several Mg alloys have demonstrated good cytocompatibility and cell adhesion/proliferation under *in vitro* and *in vivo* tests [13,51,52,152].

On the other hand, interpenetrated MgCa/HA-TCP composites have revealed a cytotoxicity effect of grade II (mild cytotoxicity [153]) on the L-929 and MG-63 cells, with a constant cell viability of around 60 % during the first 5 days of culture [83]. This grade of cell viability is similar for the first 72 hours in the here studied interpenetrated Mg/CaP composites. However, after the

6<sup>th</sup> day of cell culture, the interpenetrated composites revealed a significant decrease in cell viability reporting values below the 30 %, which denotes grade III in cytotoxicity (moderate reactivity of the material on the SAOS-2 cells), ISO 10993-5:2009 [154]. This cytotoxic effect is explained by the synergetic effect of high osmolarity and pH that exposes the investigated cells to an osmotic shock. From this point of view, nearly all Mg-alloy-based materials would be classified as cytotoxic, as the corrosion of Mg increases the pH between ~9.0-11.5, and at the same time that alters the ion concentration of the *in vitro* media [9,83,88,145,155].

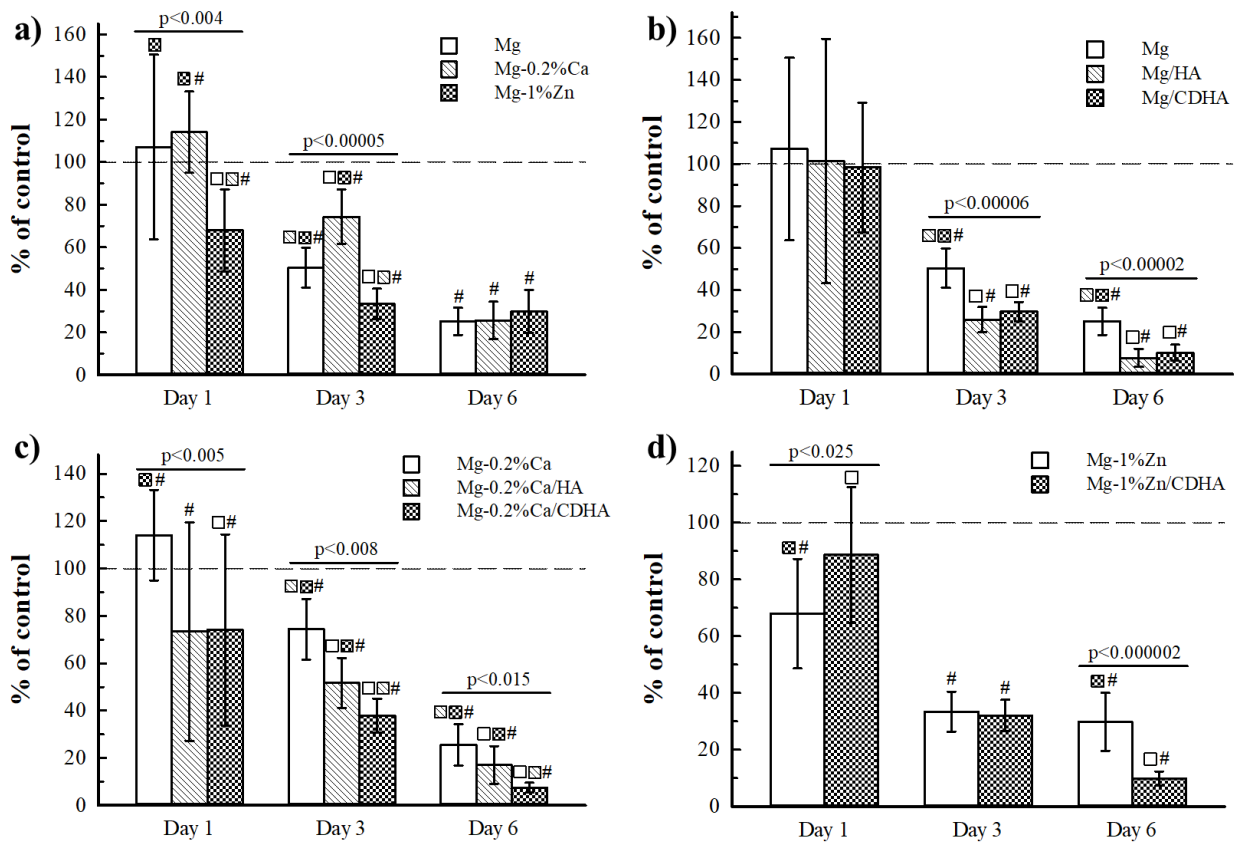


**Figure 36.** SAOS-2 viability represented as % of untreated control. Data are expressed as the mean  $\pm$  S.D. The significant differences between similar sets of samples at particular time points (Mann-Whitney U test;  $p < 0.05$ ;  $n = 16$  per each group) are marked by corresponding group legend pattern. The significant difference of a particular group from 100% of untreated control is marked by # (Student T-test,  $p < 0.05$ ;  $n = 16$  per each group).

Therefore, the high reactivity of the Mg-based composites makes difficult the *in-vitro* test procedures, which, in addition, do not correlate well with the *in-vivo* data [155,156]. In view of the above, the indirect *in-vitro* test can be improved by the use of diluted extracts obtained from the corrosion of the tested Mg-based materials. For instance, 50% and 10% degrees of extract dilution significantly improved the cell viability values of interpenetrated MgCa/HA-TCP composites (up to grade I, slight cytotoxicity) by lowering the effect of a high pH [83].

The same positive results have been reported for the Mg-Zn/ -TCP composites produced by powder metallurgy, which were found safe for cellular applications with a cytotoxicity below grade I in the L-929 cells cultured in similar diluted extracts of the corrosion products. Moreover, this testing methodology agreed better with the good biocompatibility obtained *in vivo* for bone tissue and important visceral organs of rabbits [88].

Despite the low viability percentage obtained with the SAOS-2 cells, the activity of alkaline phosphatase (ALP) was estimated by a commercial colorimetric assay for all the produced materials. This test was performed in order to measure the quantity of the ALP enzyme because of its association with bone tissue formation, among other activities in bone and liver diseases [157]. Therefore, a high level of ALP in any material indicates a strong osteoconductivity property; thus, for example pure Mg and Mg alloys have demonstrated higher ALP activity over other metals such as titanium, reflecting good biocompatibility that promotes bone regeneration [158,159].

Results from the ALP measurement (**Figure 37**) did not reveal any significant difference between the bare metallic phases and the interpenetrated composites at each particular time. All materials exhibited a significant reduction in the ALP activity after the first day of culture. This was in accordance with the decrease in cell proliferation exhibited by the produced materials.

Despite the low cell viability revealed by the interpenetrated Mg/CaP composites, *in vivo* studies have shown the great potential of Mg-based biomaterials, as is the case of pure Mg and alloys such as AZ91D, LAE442, Mg-Li-Ca, and MgCaP composites [77,156,159], other studies, compiled in the **Annex 1**.

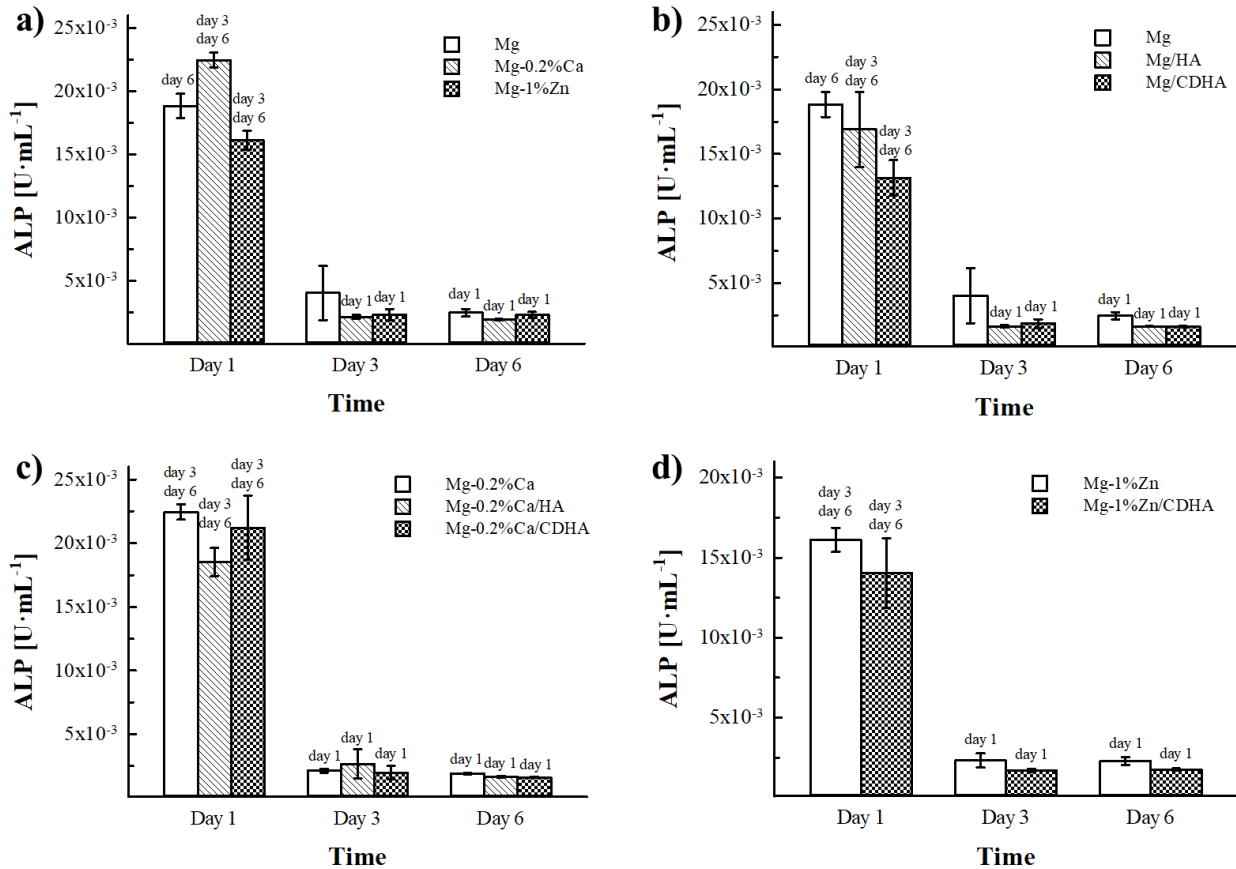


**Figure 37.** Alkaline phosphatase activity of SAOS-2. Data are expressed as the mean  $\pm$  S.D. The significant differences between time points for each sample are shown above each group and time point (one-way ANOVA;  $p < 0.05$ ;  $n = 3$  per each group). No significant differences between samples at particular time points (Mann-Whitney U test;  $p < 0.05$ ;  $n = 3$  per each group) were detected.

To sum up, the ineffective biocompatibility of the manufactured Mg/CaP was mainly connected to the fast degradation behaviour that the materials revealed, which was accompanied by the pH increasing up to an average value of 9.5. Still, based on previous results for similar Mg/CaP composites, these types of materials can find a potential application as degradable biomaterials for orthopaedics [76,83,88,135,151]. The main issues to be solved with this aim are the control of the microstructure and also the degradation behaviour, which will enhance the biocompatibility response in the cells that would be in contact with the materials. In addition, a better *in-vitro* test should be established to pair, in a reliable way, with the *in-vivo* behaviour of these types of complex materials [4,155,156].

## 6. CONCLUSIONS

The existing considerable knowledge of biomaterials for orthopaedics is being continuously developed and new discoveries are being made in terms of the interaction of such materials with the human body. Nevertheless, the necessity of innovating temporal bone-regeneration implants that allow the healing of defective bone tissue and degrade after accomplishing their function must go hand in hand with satisfying the patients and granting them the best possible treatment. In this sense, the manufacturing of predesigned composites combining degradable and bioactive components represents a novel idea in meeting the need for temporary bone fixation implants.

In the thesis, a detailed study on the processing of Mg alloys together with calcium phosphates has been performed with the aim to evaluate the feasibility of their composites as temporary bone-healing implants. The design of the Mg/CaP composites was established in an original way, combining additive manufacturing (robocasting) with a newly introduced metal infiltration technique in order to produce interpenetrated architectural composite structures.

Porous structures with controlled pore size and designed architectural geometry were successfully produced by depositing ceramic pastes, following an orthogonal pattern, to build up cylindrical scaffolds consisting of stoichiometric HA,  $\alpha$ -TCP and  $\beta$ -TCP ceramic phase. The control of the porosity was achieved by conducting a shrinkage study of each material after the sintering of the green bodies. In general, sintered structures present a bulk shrinkage of about 20 % without a clear dependence on the chemical composition of the processed CaP ceramic.

The processing of CDHA scaffolds was done by the hydrolysis of  $\alpha$ -TCP. The final CDHA structures strengthened due to the intercrossing of the resulting plate-like microstructure. No significant change in the nominal pore size of the 3D-printed structures was observed in this type of ceramic structure.

The CAMI was introduced for the first time and proved to be a novel technique for the infiltration of ceramic preforms with a molten metal such as Mg and Mg alloys. The CAMI process allows the manufacturing of interpenetrated composites with different melting points in only a few minutes and under controlled atmosphere to restrict possible reaction between the phases.

The combination of the CAMI process with additive manufacturing techniques allows the production of innovative interpenetrated composites with a diverse organized distribution of the phases according to the requirements of the final application.

The study proved that using CAMI, the micrometric pores (below  $\sim 5 \mu\text{m}$ ) in the CaP preforms were easily infiltrated by the liquid Mg phase. The infiltration success was above 98 % of the initial porosity of the scaffolds. This was achieved not only due to the infiltration technique but also because of the chemical affinity between the materials used. In this way, a chemical reaction between Mg and the CaP ceramics was observed as a reduction process resulting in the dissolution of the ceramic phase.

A chemical route was proposed for the decomposition reaction of the CaP with the contact of liquid Mg phase. However, a deeper study in this area has to be carried out prior to a successful fabrication of Mg/CaP composites for the manufacturing of degradable bioactive materials. The reduction effect of the Mg on the calcium phosphate ceramics was found to be higher in the following order:  $\beta\text{-TCP} > \text{CDHA} > \text{stoichiometric HA}$ . Although the Mg/ $\beta\text{-TCP}$  composites were produced by CAMI, the dissolution of the ceramic phase destroyed the majority of the infiltrated preforms.

Significant differences between Mg/HA and Mg/CDHA interpenetrated composites were found based on the chemical composition, phase distribution and chemical affinity between the constituents of the final composites. By way of microstructural characterization the higher reactivity between Mg and its alloys with CDHA was observed, resulting in a thicker MgO interface formation compared with the stoichiometric HA composites. The doping of 0.2 wt. % of Ca did not have any significant effect on the chemical interaction with the CaP structures. On the other hand, the addition of 1 wt. % of Zn resulted in the thinnest MgO interface, revealing a very low reactivity of this alloy with the CDHA ceramic phase.

The dissolution of the CaP preforms led to the precipitation of the  $\text{Mg}_2\text{Ca}$  intermetallic phase, which is unfavourable for the mechanical and corrosion resistance properties because of its brittleness and formation of a galvanic couple with the pure Mg or Mg alloy matrix during the corrosion process.

In terms of mechanical properties, the manufactured Mg/CaP composites exhibited the required mechanical response under compression for its function as substitutes of cancellous and low-load-bearing cortical bone according to their compressive strength and excellent failure strain above 10 % of deformation before its mechanical failure. In general, HA-based composites revealed better performance, exhibiting almost twice the compressive strength of the CDHA-based composites; which is attributed to: (1) the higher amount of ceramic phase due to its shrinkage after consolidation; and (2) the thicker MgO interface that forms in a cleavage fracture. No statistical difference was found to exist between composites manufactured with the same CaP preform, suggesting that the effect of the MgO interface was not higher than that of the phase distribution.

The resulting microstructure of the metallic phase after the infiltration process consisted of large crystal grains. This coarse microstructure detrimentally affected not only the mechanical properties but also the corrosion behaviour.

The evaluation of the corrosion rate of the composites done for both the H<sub>2</sub> evolution test and the Tafel extrapolation of polarization curves was no a trivial task due to the difficulty of measuring the real surface area of the metallic phase that was exposed to the corrosive medium. In general, the Mg/CaP composites exhibited a faster corrosion rate than the pure Mg phases did.

The HA-based composites revealed better corrosion resistance compared with their CDHA counterparts. This was attributed to the microstructure of the ceramic preforms, which in the case of the CDHA acted as an absorbent of liquid solution (SBF), promoting the corrosion of the metallic phase even in the inner part of the bulk composite body.

As a product of the fast corrosion, the cytocompatibility evaluation resulted in a low affinity of the material with SAOS-2 cells due to the increase in the pH. In the proliferation test, the bare metals revealed a better cytocompatibility response than their composites along the first week of testing. The production of ALP was also low for all the produced materials.

Finally, despite the cytotoxic response of the interpenetrated Mg/CaP composites, the development of these types of materials can still have a potential for their application as degradable biomaterials. This is based on the assumption that the cytocompatibility response can be enhanced by controlling the microstructure and degradation of the Mg-based phase, maintaining a suitable mechanical performance for the production of temporal orthopaedic devices.

## **SUGGESTED FUTURE WORK**

As was observed above, the reactivity between Mg and CaP is an issue that needs to be studied in more detail. A systematic study varying the chemical composition of the CaP, e.g. the Ca/P atomic ratio and initial source, could prove the difference in the affinity between these compounds and determine the effect of the initial characteristics of the calcium phosphate phase on their reactivity by the interaction with molten Mg and its alloys.

Results in the studied composites showed that the addition of Zn to form Mg-Zn alloys enhanced the interaction with CaP by decreasing the reactivity between them; in this way, a study contemplating the presence of Zn in Mg or Zn-based composites represents a highly interesting case of study for future degradable biomaterials.

The variation in the phase distribution in the interpenetrated composites resulted in different mechanical properties. Therefore, a systematic study varying the percentage of the phase and distribution can help to better understand the mechanical properties and fracture mechanism that can be obtained in the interpenetrated Mg/CaP composites. This study can reveal if the predesign of interpenetrated composites is feasible before their manufacturing as an attempt at manufacturing tailored interpenetrated composites.

It is also encouraging to perform a post-processing of the interpenetrated Mg/CaP composites, such as additional heat treatment or surface modification, which can improve the corrosion behaviour and, consequently, the biological response. In this direction, an electro-assisted oxidation applied to forming a protective layer could be one of the options, as well as controlling the final microstructure of the metal phase. This allows improving the mechanical properties as has been proved by extruded Mg/HA composites [78] and special melt shearing technology for the case of Mg/ $\beta$ -TCP [79].

## BIBLIOGRAPHY

- [1] E. Hernlund, A. Svedbom, M. Ivergård, J. Compston, C. Cooper, J. Stenmark, E. V. McCloskey, B. Jönsson, J.A. Kanis, Osteoporosis in the European Union: medical management, epidemiology and economic burden, *Arch. Osteoporos.* 8 (2013) 136. <https://doi.org/10.1007/s11657-013-0136-1>.
- [2] A. Svedbom, E. Hernlund, M. Ivergård, J. Compston, C. Cooper, J. Stenmark, E. V. McCloskey, B. Jönsson, J.A. Kanis, Osteoporosis in the European Union: a compendium of country-specific reports, *Arch. Osteoporos.* 8 (2013) 137. <https://doi.org/10.1007/s11657-013-0137-0>.
- [3] A.K. Nasution, H. Hermawan, Degradable Biomaterials for Temporary Medical Implants BT - Biomaterials and Medical Devices: A Perspective from an Emerging Country, in: F. Mahyudin, H. Hermawan (Eds.), Springer International Publishing, Cham, 2016: pp. 127–160. [https://doi.org/10.1007/978-3-319-14845-8\\_6](https://doi.org/10.1007/978-3-319-14845-8_6).
- [4] F. Witte, F. Feyerabend, P. Maier, J. Fischer, M. Störmer, C. Blawert, W. Dietzel, N. Hort, Biodegradable magnesium–hydroxyapatite metal matrix composites, *Biomaterials.* 28 (2007) 2163–2174. <https://doi.org/10.1016/j.biomaterials.2006.12.027>.
- [5] A.K. Khanra, H.C. Jung, S.H. Yu, K.S. Hong, K.S. Shin, Microstructure and mechanical properties of Mg-HAP composites, *Bull. Mater. Sci.* 33 (2010) 43–47. <https://doi.org/10.1007/s12034-010-0006-z>.
- [6] R.Z. LeGeros, J.P. LeGeros, Calcium phosphate Bioceramics: Past, present and future, *Bioceram.* 15. 240–2 (2003) 3–10. <https://doi.org/DOI 10.4028/www.scientific.net/kem.240-242.3>.
- [7] K. Mensah-Darkwa, R.K. Gupta, D. Kumar, Mechanical and Corrosion Properties of Magnesium–Hydroxyapatite (Mg–HA) Composite Thin Films, *J. Mater. Sci. Technol.* 29 (2013) 788–794. <https://doi.org/10.1016/j.jmst.2013.04.019>.
- [8] M.P. Staiger, A.M. Pietak, J. Huadmai, G. Dias, Magnesium and its alloys as orthopedic biomaterials: A review, *Biomaterials.* 27 (2006) 1728–1734. <https://doi.org/10.1016/j.biomaterials.2005.10.003>.
- [9] F. Witte, N. Hort, C. Vogt, S. Cohen, K.U. Kainer, R. Willumeit, F. Feyerabend, Degradable biomaterials based on magnesium corrosion, *Curr. Opin. Solid State Mater. Sci.* 12 (2008) 63–72. <https://doi.org/10.1016/j.cossms.2009.04.001>.
- [10] F. Witte, The history of biodegradable magnesium implants: A review, *Acta Biomater.* 6 (2010) 1680–1692. <https://doi.org/10.1016/j.actbio.2010.02.028>.
- [11] Y. Chen, Z. Xu, C. Smith, J. Sankar, Recent advances on the development of magnesium alloys for biodegradable implants, *Acta Biomater.* 10 (2014) 4561–4573. <https://doi.org/10.1016/j.actbio.2014.07.005>.
- [12] F. Witte, V. Kaese, H. Haferkamp, E. Switzer, A. Meyer-Lindenberg, C.J. Wirth, H. Windhagen, In vivo corrosion of four magnesium alloys and the associated bone response, *Biomaterials.* 26 (2005) 3557–3563. <https://doi.org/10.1016/j.biomaterials.2004.09.049>.

- [13] A. Myrissa, N.A. Agha, Y. Lu, E. Martinelli, J. Eichler, G. Szakács, C. Kleinhans, R. Willumeit-Römer, U. Schäfer, A.-M. Weinberg, In vitro and in vivo comparison of binary Mg alloys and pure Mg, *Mater. Sci. Eng. C.* 61 (2016) 865–874. <https://doi.org/10.1016/j.msec.2015.12.064>.
- [14] X. Gu, Y. Zheng, Y. Cheng, S. Zhong, T. Xi, In vitro corrosion and biocompatibility of binary magnesium alloys, *Biomaterials.* 30 (2009) 484–498. <https://doi.org/10.1016/j.biomaterials.2008.10.021>.
- [15] D.R. Clarke, Interpenetrating Phase Composites, *J. Am. Ceram. Soc.* 75 (1992) 739–758. <https://doi.org/10.1111/j.1151-2916.1992.tb04138.x>.
- [16] A. Mattern, B. Huchler, D. Staudenecker, R. Oberacker, A. Nagel, M.J. Hoffmann, Preparation of interpenetrating ceramic–metal composites, *J. Eur. Ceram. Soc.* 24 (2004) 3399–3408. <https://doi.org/10.1016/j.jeurceramsoc.2003.10.030>.
- [17] K.M. Sree Manu, L. Ajay Raag, T.P.D. Rajan, M. Gupta, B.C. Pai, Liquid Metal Infiltration Processing of Metallic Composites: A Critical Review, *Metall. Mater. Trans. B.* 47 (2016) 2799–2819. <https://doi.org/10.1007/s11663-016-0751-5>.
- [18] S. Grasso, Y. Sakka, G. Maizza, Electric current activated/assisted sintering ( ECAS ): a review of patents 1906–2008, *Sci. Technol. Adv. Mater.* 10 (2009) 053001. <https://doi.org/10.1088/1468-6996/10/5/053001>.
- [19] R. Orrù, R. Licheri, A.M. Locci, A. Cincotti, G. Cao, Consolidation/synthesis of materials by electric current activated/assisted sintering, *Mater. Sci. Eng. R Reports.* 63 (2009) 127–287. <https://doi.org/10.1016/j.mser.2008.09.003>.
- [20] J. Park, R.S. Lakes, Biomaterials: An introduction, 3rd Ed., Springer US, New York, 2007. <https://doi.org/10.1007/978-0-387-37880-0>.
- [21] M. Rühle, Structure and composition of metal/ceramic interfaces, *J. Eur. Ceram. Soc.* 16 (1996) 353–365. [https://doi.org/10.1016/0955-2219\(95\)00194-8](https://doi.org/10.1016/0955-2219(95)00194-8).
- [22] L.L. Hench, I. Thompson, Twenty-first century challenges for biomaterials Subject collections Twenty-first century challenges for biomaterials, *J. R. Soc. Interface.* 7 (2010) S379–S391. <https://doi.org/10.1098/rsif.2010.0151.focus>.
- [23] H. Larry L, P. Julia M, Third-generation biomedical materials, *Science (80-. ).* 295 (2002) 1014–1017. <https://doi.org/10.1126/science.1067404>.
- [24] Biomaterials Market by Type of Materials (Metallic, Ceramic, Polymers, Natural) & By Application (Cardiovascular, Orthopedic, Dental, Plastic Surgery, Wound Healing, Neurological disorders, Tissue Engineering, Ophthalmology) - Global Forecast to 2024, *Mark. Mark.* (n.d.). <https://www.marketsandmarkets.com/Market-Reports/biomaterials-393.html> (accessed July 12, 2019).
- [25] M. Prakasam, J. Locs, K. Salma-Ancane, D. Loca, A. Largeteau, L. Berzina-Cimdina, Biodegradable Materials and Metallic Implants—A Review, *J. Funct. Biomater.* 8 (2017) 44. <https://doi.org/10.3390/jfb8040044>.
- [26] A.R. Amini, J.S. Wallace, S.P. Nukavarapu, Short-term and long-term effects of orthopedic

- biodegradable implants, *J. Long. Term. Eff. Med. Implants.* 21 (2011) 93–122. <https://doi.org/10.1615/jlongtermeffmedimplants.v21.i2.10>.
- [27] Bohner M., Calcium orthophosphates in medicine: from ceramics to calcium phosphate cements., *Injury.* 31 (2000) SD37–47.
- [28] J. Lu, M. Descamps, J. Dejou, G. Koubi, P. Hardouin, J. Lemaitre, J.P. Proust, The biodegradation mechanism of calcium phosphate biomaterials in bone, in: *J. Biomed. Mater. Res.*, 2002: pp. 408–412. <https://doi.org/10.1002/jbm.10259>.
- [29] N. Sezer, Z. Evis, S.M. Kayhan, A. Tahmasebifar, M. Koç, Review of magnesium-based biomaterials and their applications, *J. Magnes. Alloy.* 6 (2018) 23–43. <https://doi.org/10.1016/j.jma.2018.02.003>.
- [30] Y.F. Zheng, X.N. Gu, F. Witte, Biodegradable metals, *Mater. Sci. Eng. R Reports.* 77 (2014) 1–34. <https://doi.org/10.1016/j.mser.2014.01.001>.
- [31] R.Z. LeGeros, Biodegradation and bioresorption of calcium phosphate ceramics, *Clin. Mater.* 14 (1993) 65–88. [https://doi.org/10.1016/0267-6605\(93\)90049-d](https://doi.org/10.1016/0267-6605(93)90049-d).
- [32] H. YUAN, Z. YANG, Y. LI, X. ZHANG, J.D. DE BRUIJN, K. DE GROOT, Osteoinduction by calcium phosphate biomaterials, *J. Mater. Sci. Mater. Med.* 9 (1998) 723–726. <https://doi.org/10.1023/a:1008950902047>.
- [33] B.S. Chang, C.K. Lee, K.S. Hong, H.J. Youn, H.S. Ryu, S.S. Chung, K.W. Park, Osteoconduction at porous hydroxyapatite with various pore configurations, *Biomaterials.* 21 (2000) 1291–1298. [https://doi.org/10.1016/s0142-9612\(00\)00030-2](https://doi.org/10.1016/s0142-9612(00)00030-2).
- [34] K. Lin, J. Chang, Structure and properties of hydroxyapatite for biomedical applications, in: M.B.T.-H. (Hap) for B.A. Mucalo (Ed.), *Hydroxyapatite Biomed. Appl.*, Elsevier, 2015: pp. 3–19. <https://doi.org/10.1016/b978-1-78242-033-0.00001-8>.
- [35] W. Suchanek, M. Yoshimura, Processing and properties of hydroxyapatite-based biomaterials for use as hard tissue replacement implants, *J. Mater. Res.* 13 (1998) 94–117. <https://doi.org/10.1557/jmr.1998.0015>.
- [36] A. Tampieri, G. Celotti, S. Sprio, A. Delcogliano, S. Franzese, Porosity-graded hydroxyapatite ceramics to replace natural bone, *Biomaterials.* 22 (2001) 1365–1370. [https://doi.org/10.1016/s0142-9612\(00\)00290-8](https://doi.org/10.1016/s0142-9612(00)00290-8).
- [37] P. Habibovic, F. Barrère, C.A. Blitterswijk, K. Groot, P. Layrolle, Biomimetic Hydroxyapatite Coating on Metal Implants, *J. Am. Ceram. Soc.* 85 (2004) 517–522. <https://doi.org/10.1111/j.1151-2916.2002.tb00126.x>.
- [38] P. Ducheyne, W. Van Raemdonck, J.C. Heughebaert, M. Heughebaert, Structural analysis of hydroxyapatite coatings on titanium, *Biomaterials.* 7 (1986) 97–103. [https://doi.org/10.1016/0142-9612\(86\)90063-3](https://doi.org/10.1016/0142-9612(86)90063-3).
- [39] D.M. Liu, Q. Yang, T. Troczynski, Sol-gel hydroxyapatite coatings on stainless steel substrates, *Biomaterials.* 23 (2002) 691–698. [https://doi.org/10.1016/s0142-9612\(01\)00157-0](https://doi.org/10.1016/s0142-9612(01)00157-0).
- [40] J. Park, ed., *Hydroxyapatite*, in: *Bioceramics*, Springer New York, New York, NY, 2008:

pp. 177–197. [https://doi.org/10.1007/978-0-387-09545-5\\_9](https://doi.org/10.1007/978-0-387-09545-5_9).

- [41] B. Bourgeois, O. Laboux, L. Obadia, O. Gauthier, E. Betti, E. Aguado, G. Daculsi, J.-M. Bouler, Calcium-deficient apatite: A first in vivo study concerning bone ingrowth, *J. Biomed. Mater. Res.* 65A (2003) 402–408. <https://doi.org/10.1002/jbm.a.10518>.
- [42] K.S. TenHuisen, P.W. Brown, Formation of calcium-deficient hydroxyapatite from  $\alpha$ -tricalcium phosphate, *Biomaterials*. 19 (1998) 2209–2217. [https://doi.org/10.1016/s0142-9612\(98\)00131-8](https://doi.org/10.1016/s0142-9612(98)00131-8).
- [43] I.R. Gibson, I. Rehman, S.M. Best, W. Bonfield, Characterization of the transformation from calcium-deficient apatite to  $\beta$ -tricalcium phosphate, *J. Mater. Sci. Mater. Med.* 11 (2000) 799–804. <https://doi.org/10.1023/a:1008905613182>.
- [44] D.S. Metsger, T.D. Driskell, J.R. Paulsrud, Tricalcium Phosphate Ceramic—A Resorbable Bone Implant: Review and Current Status, *J. Am. Dent. Assoc.* 105 (1982) 1035–1038. <https://doi.org/10.14219/jada.archive.1982.0408>.
- [45] A.A. Mirtchi, J. Lemaitre, N. Terao, Calcium phosphate cements: study of the  $\beta$ -tricalcium phosphate — monocalcium phosphate system, *Biomaterials*. 10 (1989) 475–480. [https://doi.org/10.1016/0142-9612\(89\)90089-6](https://doi.org/10.1016/0142-9612(89)90089-6).
- [46] R.G. Carrodeguas, S. De Aza,  $\alpha$ -Tricalcium phosphate: Synthesis, properties and biomedical applications, *Acta Biomater.* 7 (2011) 3536–3546. <https://doi.org/10.1016/j.actbio.2011.06.019>.
- [47] S. V Dorozhkin, Calcium orthophosphate cements for biomedical application, *J. Mater. Sci.* 43 (2008) 3028–3057. <https://doi.org/10.1007/s10853-008-2527-z>.
- [48] L. Wang, G.H. Nancollas, Calcium Orthophosphates: Crystallization and Dissolution, *Chem. Rev.* 108 (2008) 4628–4669. <https://doi.org/10.1021/cr0782574>.
- [49] W. Habraken, P. Habibovic, M. Epple, M. Böhner, Calcium phosphates in biomedical applications: materials for the future?, *Mater. Today*. 19 (2016) 69–87. <https://doi.org/10.1016/j.mattod.2015.10.008>.
- [50] V. KARAGEORGIU, D. KAPLAN, Porosity of 3D biomaterial scaffolds and osteogenesis, *Biomaterials*. 26 (2005) 5474–5491. <https://doi.org/10.1016/j.biomaterials.2005.02.002>.
- [51] N. Li, Y. Zheng, Novel Magnesium Alloys Developed for Biomedical Application: A Review, *J. Mater. Sci. Technol.* 29 (2013) 489–502. <https://doi.org/10.1016/j.jmst.2013.02.005>.
- [52] K.F. Farraro, K.E. Kim, S.L.-Y. Woo, J.R. Flowers, M.B. McCullough, Revolutionizing orthopaedic biomaterials: The potential of biodegradable and bioresorbable magnesium-based materials for functional tissue engineering, *J. Biomech.* 47 (2014) 1979–1986. <https://doi.org/10.1016/j.jbiomech.2013.12.003>.
- [53] Y. Yun, Z. Dong, N. Lee, Y. Liu, D. Xue, X. Guo, J. Kuhlmann, A. Doepke, H.B. Halsall, W. Heineman, S. Sundaramurthy, M.J. Schulz, Z. Yin, V. Shanov, D. Hurd, P. Nagy, W. Li, C. Fox, Revolutionizing biodegradable metals, *Mater. Today*. 12 (2009) 22–32.

[https://doi.org/10.1016/s1369-7021\(09\)70273-1](https://doi.org/10.1016/s1369-7021(09)70273-1).

- [54] H.S. Han, S. Loffredo, I. Jun, J. Edwards, Y.C. Kim, H.K. Seok, F. Witte, D. Mantovani, S. Glyn-Jones, Current status and outlook on the clinical translation of biodegradable metals, *Mater. Today*. 23 (2019) 57–71. <https://doi.org/10.1016/j.mattod.2018.05.018>.
- [55] G. Song, D. StJohn, The effect of zirconium grain refinement on the corrosion behaviour of magnesium-rare earth alloy MEZ, *J. Light Met.* 2 (2002) 1–16. [https://doi.org/10.1016/s1471-5317\(02\)00008-1](https://doi.org/10.1016/s1471-5317(02)00008-1).
- [56] H.E. Friedrich, B.L. Mordike, *Magnesium Technology*, Springer-Verlag, Berlin/Heidelberg, 2006. <https://doi.org/10.1007/3-540-30812-1>.
- [57] I.I.I. Cesarano Joseph (Albuquerque, NM), P.D. (Tucson Calvert AZ), Freeforming objects with low-binder slurry, 2000. <https://www.osti.gov/servlets/purl/872863>.
- [58] J.A. Lewis, J.E. Smay, J. Stuecker, J. Cesarano, Direct ink writing of three-dimensional ceramic structures, *J. Am. Ceram. Soc.* 89 (2006) 3599–3609. <https://doi.org/10.1111/j.1551-2916.2006.01382.x>.
- [59] T.A. Baer, J. Cesarano III, P. Calvert, J. Cesarano, T.A. Baer, P. Calvert, Recent developments in freeform fabrication of dense ceramics from slurry deposition, *Solid Free. Fabr. Proceedings, Sept. 1997*. (1997) 25–32.
- [60] J.A. Lewis, G.M. Gratson, Direct writing in three dimensions, *Mater. Today*. 7 (2004) 32–39. [https://doi.org/10.1016/s1369-7021\(04\)00344-x](https://doi.org/10.1016/s1369-7021(04)00344-x).
- [61] Z. Pan, Y. Wang, H. Huang, Z. Ling, Y. Dai, S. Ke, Recent development on preparation of ceramic inks in ink-jet printing, *Ceram. Int.* 41 (2015) 12515–12528. <https://doi.org/10.1016/j.ceramint.2015.06.124>.
- [62] E. Feilden, E.G.-T. Blanca, F. Giuliani, E. Saiz, L. Vandeperre, Robocasting of structural ceramic parts with hydrogel inks, *J. Eur. Ceram. Soc.* 36 (2016) 2525–2533. <https://doi.org/10.1016/j.jeurceramsoc.2016.03.001>.
- [63] J. Franco, P. Hunger, M.E. Launey, A.P. Tomsia, E. Saiz, Direct write assembly of calcium phosphate scaffolds using a water-based hydrogel, *Acta Biomater.* 6 (2010) 218–228.
- [64] A.R. Akkineni, Y. Luo, M. Schumacher, B. Nies, A. Lode, M. Gelinsky, 3D plotting of growth factor loaded calcium phosphate cement scaffolds, *Acta Biomater.* 27 (2015) 264–274. <https://doi.org/10.1016/j.actbio.2015.08.036>.
- [65] A. Butscher, M. Bohner, S. Hofmann, L. Gauckler, R. Müller, Structural and material approaches to bone tissue engineering in powder-based three-dimensional printing, *Acta Biomater.* 7 (2011) 907–920. <https://doi.org/10.1016/j.actbio.2010.09.039>.
- [66] P. Miranda, A. Pajares, E. Saiz, A.P. Tomsia, F. Guiberteau, Mechanical properties of calcium phosphate scaffolds fabricated by robocasting, *J. Biomed. Mater. Res. Part A*. 85A (2008) 218–227. <https://doi.org/10.1002/jbm.a.31587>.
- [67] S. Michna, W. Wu, J.A. Lewis, Concentrated hydroxyapatite inks for direct-write assembly of 3-D periodic scaffolds, *Biomaterials*. 26 (2005) 5632–5639. <https://doi.org/10.1016/j.biomaterials.2005.02.040>.

- [68] P. Miranda, E. Saiz, K. Gryn, A.P. Tomsia, Sintering and robocasting of beta-tricalcium phosphate scaffolds for orthopaedic applications, *Acta Biomater.* 2 (2006) 457–466.
- [69] K.-F. Lin, S. He, Y. Song, C.-M. Wang, Y. Gao, J.-Q. Li, P. Tang, Z. Wang, L. Bi, G.-X. Pei, Low-Temperature Additive Manufacturing of Biomimic Three-Dimensional Hydroxyapatite/Collagen Scaffolds for Bone Regeneration, *ACS Appl. Mater. Interfaces.* 8 (2016) 6905–6916. <https://doi.org/10.1021/acsami.6b00815>.
- [70] I.N. Orbulov, Metal matrix syntactic foams produced by pressure infiltration—The effect of infiltration parameters, *Mater. Sci. Eng. A.* 583 (2013) 11–19. <https://doi.org/10.1016/j.msea.2013.06.066>.
- [71] L. Hu, A. Kothalkar, M. O’Neil, I. Karaman, M. Radovic, Current-Activated, Pressure-Assisted Infiltration: A Novel, Versatile Route for Producing Interpenetrating Ceramic–Metal Composites, *Mater. Res. Lett.* 2 (2014) 124–130. <https://doi.org/10.1080/21663831.2013.873498>.
- [72] Z.A. Munir, U. Anselmi-Tamburini, M. Ohyanagi, The effect of electric field and pressure on the synthesis and consolidation of materials: A review of the spark plasma sintering method, *J. Mater. Sci.* 41 (2006) 763–777. <https://doi.org/10.1007/s10853-006-6555-2>.
- [73] S.D. de la Torre, L. Čelko, M.C. Luna, E.B.M. Jiménez, On the preparation of advanced materials via pulsed electric current sintering procedures, in: *Solid State Phenom.*, 2017: pp. 436–439. <https://doi.org/10.4028/www.scientific.net/ssp.258.436>.
- [74] M. Casas-Luna, S. Tkachenko, M. Horynová, L. Klakurková, P. Gejdos, S. Diaz-De-La-Torre, L. Celko, J. Kaiser, E.B. Montufar, Interpenetrated magnesium-tricalcium phosphate composite: Manufacture, characterization and in vitro degradation test, *Acta Metall. Sin. (English Lett.* 30 (2017). <https://doi.org/10.1007/s40195-017-0560-0>.
- [75] M. Casas-Luna, S. Tkachenko, L. Klakurková, J. Torres, M. Kareš, J. Kaiser, Micro-computed tomography of interconnected  $\beta$ -TCP - Mg composites obtained by current assisted metal infiltration, in: *Met. 2017 - 26th Int. Conf. Metall. Mater. Conf. Proc.*, 2017.
- [76] M. Haghshenas, Mechanical characteristics of biodegradable magnesium matrix composites: A review, *J. Magnes. Alloy.* 5 (2017) 189–201. <https://doi.org/10.1016/j.jma.2017.05.001>.
- [77] K. Kuśnierczyk, M. Basista, Recent advances in research on magnesium alloys and magnesium–calcium phosphate composites as biodegradable implant materials, *J. Biomater. Appl.* 31 (2017) 878–900. <https://doi.org/10.1177/0885328216657271>.
- [78] R. del Campo, B. Savoini, A. Muñoz, M.A. Monge, G. Garcés, Mechanical properties and corrosion behavior of Mg–HAP composites, *J. Mech. Behav. Biomed. Mater.* 39 (2014) 238–246. <https://doi.org/10.1016/j.jmbbm.2014.07.014>.
- [79] D. Liu, Y. Zuo, W. Meng, M. Chen, Z. Fan, Fabrication of biodegradable nano-sized  $\beta$ -TCP/Mg composite by a novel melt shearing technology, *Mater. Sci. Eng. C.* 32 (2012) 1253–1258. <https://doi.org/10.1016/j.msec.2012.03.017>.
- [80] S. HE, Y. SUN, M. CHEN, D. LIU, X. YE, Microstructure and properties of biodegradable  $\beta$ -TCP reinforced Mg-Zn-Zr composites, *Trans. Nonferrous Met. Soc. China.* 21 (2011)

814–819. [https://doi.org/10.1016/s1003-6326\(11\)60786-3](https://doi.org/10.1016/s1003-6326(11)60786-3).

- [81] X.L. Ma, L.H. Dong, X. Wang, Microstructure, mechanical property and corrosion behavior of co-continuous  $\beta$ -TCP/MgCa composite manufactured by suction casting, *Mater. Des.* 56 (2014) 305–312. <https://doi.org/10.1016/j.matdes.2013.11.041>.
- [82] X. Wang, L.H. Dong, J.T. Li, X.L. Li, X.L. Ma, Y.F. Zheng, Microstructure, mechanical property and corrosion behavior of interpenetrating (HA+ $\beta$ -TCP)/MgCa composite fabricated by suction casting, *Mater. Sci. Eng. C.* 33 (2013) 4266–4273. <https://doi.org/10.1016/j.msec.2013.06.018>.
- [83] X.N. Gu, X. Wang, N. Li, L. Li, Y.F. Zheng, X. Miao, Microstructure and characteristics of the metal-ceramic composite (MgCa-HA/TCP) fabricated by liquid metal infiltration, *J. Biomed. Mater. Res. Part B Appl. Biomater.* 99B (2011) 127–134. <https://doi.org/10.1002/jbm.b.31879>.
- [84] X. Gu, W. Zhou, Y. Zheng, L. Dong, Y. Xi, D. Chai, Microstructure, mechanical property, bio-corrosion and cytotoxicity evaluations of Mg/HA composites, *Mater. Sci. Eng. C.* 30 (2010) 827–832. <https://doi.org/10.1016/j.msec.2010.03.016>.
- [85] K.A. Khalil, E.S.M. Sherif, A.A. Almajid, Corrosion passivation in simulated body fluid of magnesium/hydroxyapatite nanocomposites sintered by high frequency induction heating, *Int. J. Electrochem. Sci.* 6 (2011) 6184–6199. [www.electrochemsci.org](http://www.electrochemsci.org) (accessed October 21, 2019).
- [86] K. Narita, Q. Tian, I. Johnson, C. Zhang, E. Kobayashi, H. Liu, Degradation behaviors and cytocompatibility of Mg/ $\beta$ -tricalcium phosphate composites produced by spark plasma sintering, *J. Biomed. Mater. Res. Part B Appl. Biomater.* 107 (2019) 2238–2253. <https://doi.org/10.1002/jbm.b.34316>.
- [87] L. Ren, X. Lin, L. Tan, K. Yang, Effect of surface coating on antibacterial behavior of magnesium based metals, *Mater. Lett.* 65 (2011) 3509–3511. <https://doi.org/10.1016/j.matlet.2011.07.109>.
- [88] K. Yu, L. Chen, J. Zhao, S. Li, Y. Dai, Q. Huang, Z. Yu, In vitro corrosion behavior and in vivo biodegradation of biomedical  $\beta$ -Ca<sub>3</sub>(PO<sub>4</sub>)<sub>2</sub>/Mg–Zn composites, *Acta Biomater.* 8 (2012) 2845–2855. <https://doi.org/10.1016/j.actbio.2012.04.009>.
- [89] M. Tamai, M. Nakamura, T. Isshiki, K. Nishio, H. Endoh, A. Nakahira, A metastable phase in thermal decomposition of Ca-deficient hydroxyapatite, *J. Mater. Sci. Mater. Med.* 14 (2003) 617–622. <https://doi.org/10.1023/a:1024075008165>.
- [90] L. Čelko, M. Menelaou, M. Casas-Luna, M. Horynová, T. Musálek, M. Remešová, S. Díaz-de-la-Torre, K. Morsi, J. Kaiser, Spark Plasma Extrusion and the Thermal Barrier Concept, *Metall. Mater. Trans. B.* 50 (2019) 656–665. <https://doi.org/10.1007/s11663-018-1493-3>.
- [91] N. Jinlong, Z. Zhenxi, J. Dazong, Investigation of Phase Evolution During the Thermochemical Synthesis of Tricalcium Phosphate, *J. Mater. Synth. Process.* 9 (2001) 235–240. <https://doi.org/10.1023/a:1015243216516>.
- [92] T. Schlordt, F. Keppner, N. Travitzky, P. Greil, Robocasting of alumina lattice truss structures, *J. Ceram. Sci. Technol.* 3 (2012) 81–88. <https://doi.org/10.4416/jcst2012-00003>.

- [93] J. Cesarano, T.A. Baer, P. Calvert, Recent developments in freeform fabrication of dense ceramics from slurry deposition, *Solid Free. Fabr. Proceedings, Sept. 1997. (1997)* 25–32.
- [94] Z. Li, X. Gu, S. Lou, Y. Zheng, The development of binary Mg-Ca alloys for use as biodegradable materials within bone, *Biomaterials*. 29 (2008) 1329–1344. <https://doi.org/10.1016/j.biomaterials.2007.12.021>.
- [95] K. Narita, E. Kobayashi, T. Sato, Sintering Behavior and Mechanical Properties of Magnesium/ $\beta$ -Tricalcium Phosphate Composites Sintered by Spark Plasma Sintering, *Mater. Trans.* 57 (2016) 1620–1627. <https://doi.org/10.2320/matertrans.l-m2016827>.
- [96] F. Shapiro, Bone development and its relation to fracture repair. The role of mesenchymal osteoblasts and surface osteoblasts, *Eur. Cells Mater.* 15 (2008) 53–76. <https://doi.org/10.22203/ecm.v015a05>.
- [97] G.L. Song, A. Atrens, Corrosion Mechanisms of Magnesium Alloys, *Adv. Eng. Mater.* 1 (1999) 11–33. [https://doi.org/10.1002/\(sici\)1527-2648\(199909\)1:1<11::aid-ademl1>3.0.co;2-n](https://doi.org/10.1002/(sici)1527-2648(199909)1:1<11::aid-ademl1>3.0.co;2-n).
- [98] F. Ozdemir, I. Evans, O. Bretcanu, Calcium Phosphate Cements for Medical Applications, in: *Clin. Appl. Biomater.*, Springer International Publishing, Cham, 2017: pp. 91–121. [https://doi.org/10.1007/978-3-319-56059-5\\_4](https://doi.org/10.1007/978-3-319-56059-5_4).
- [99] F. Bakan, A Systematic Study of the Effect of pH on the Initialization of Ca-deficient Hydroxyapatite to  $\beta$ -TCP Nanoparticles, *Materials (Basel)*. 12 (2019) 354. <https://doi.org/10.3390/ma12030354>.
- [100] S. Raymond, Y. Maazouz, E.B. Montufar, R.A. Perez, B. González, J. Konka, J. Kaiser, M.-P. Ginebra, Accelerated hardening of nanotextured 3D-plotted self-setting calcium phosphate inks, *Acta Biomater.* 75 (2018) 451–462. <https://doi.org/10.1016/j.actbio.2018.05.042>.
- [101] E. Fernández, M.P. Ginebra, M.G. Boltong, F.C.M. Driessens, J.A. Planell, J. Ginebra, E.A.P. De Maeyer, R.M.H. Verbeeck, Kinetic study of the setting reaction of a calcium phosphate bone cement, *J. Biomed. Mater. Res.* 32 (1996) 367–374. [https://doi.org/10.1002/\(sici\)1097-4636\(199611\)32:3<367::aid-jbm9>3.0.co;2-q](https://doi.org/10.1002/(sici)1097-4636(199611)32:3<367::aid-jbm9>3.0.co;2-q).
- [102] J. Duncan, J.F. MacDonald, J. V. Hanna, Y. Shirosaki, S. Hayakawa, A. Osaka, J.M.S. Skakle, I.R. Gibson, The role of the chemical composition of monetite on the synthesis and properties of  $\alpha$ -tricalcium phosphate, *Mater. Sci. Eng. C*. 34 (2014) 123–129. <https://doi.org/10.1016/j.msec.2013.08.038>.
- [103] M. Mezbahul-Islam, A.O. Mostafa, M. Medraj, Essential Magnesium Alloys Binary Phase Diagrams and Their Thermochemical Data, *J. Mater.* 2014 (2014) 1–33. <https://doi.org/10.1155/2014/704283>.
- [104] M. Pogorielov, E. Husak, A. Solodivnik, S. Zhdanov, Magnesium-based biodegradable alloys: Degradation, application, and alloying elements, *Interv. Med. Appl. Sci.* 9 (2017) 27–38. <https://doi.org/10.1556/1646.9.2017.1.04>.
- [105] A.C. Bîrcă, I.A. Neacșu, O.R. Vasile, I. Ciucă, I.M. Vasile, M.A. Fayeeg, B.Ş. Vasile, Mg-Zn alloys, most suitable for biomedical applications., *Rom. J. Morphol. Embryol.* 59 (2018)

49–54. <http://www.ncbi.nlm.nih.gov/pubmed/29940611> (accessed November 7, 2019).

- [106] Y. Chen, J. Dou, H. Yu, C. Chen, Degradable magnesium-based alloys for biomedical applications: The role of critical alloying elements, *J. Biomater. Appl.* 33 (2019) 1348–1372. <https://doi.org/10.1177/0885328219834656>.
- [107] L. Bolzoni, U. Joshi, R. Alain, D. Garetto, N.H. Babu, Refinement of Mg alloys crystal structure via Nb-based heterogeneous substrates for improved performances, *Mater. Sci. Eng. A.* 723 (2018) 70–78. <https://doi.org/10.1016/j.msea.2018.03.005>.
- [108] S.H. Allameh, M. Emamy, E. Maleki, B. Pourbahari, Effect of Microstructural Refinement on Tensile Properties of AZ80 Magnesium Alloy via Ca Addition and Extrusion Process, *Procedia Mater. Sci.* 11 (2015) 89–94. <https://doi.org/10.1016/j.mspro.2015.11.115>.
- [109] Technical Committee ISO/TC156, ISO 8407:1991 Corrosion of metal and alloys - Removal of corrosion products from corrosion test specimens, 1991. <https://www.iso.org/standard/42634.html> (accessed November 11, 2019).
- [110] M. Esmaily, J.E. Svensson, S. Fajardo, N. Birbilis, G.S. Frankel, S. Virtanen, R. Arrabal, S. Thomas, L.G. Johansson, Fundamentals and advances in magnesium alloy corrosion, *Prog. Mater. Sci.* 89 (2017) 92–193. <https://doi.org/10.1016/j.pmatsci.2017.04.011>.
- [111] G. Song, A. Atrens, Understanding Magnesium Corrosion—A Framework for Improved Alloy Performance, *Adv. Eng. Mater.* 5 (2003) 837–858. <https://doi.org/10.1002/adem.200310405>.
- [112] D. Zhao, T. Wang, J. Kuhlmann, Z. Dong, S. Chen, M. Joshi, P. Salunke, V.N. Shanov, D. Hong, P.N. Kumta, W.R. Heineman, In vivo monitoring the biodegradation of magnesium alloys with an electrochemical H<sub>2</sub> sensor, *Acta Biomater.* 36 (2016) 361–368. <https://doi.org/10.1016/j.actbio.2016.03.039>.
- [113] Y. Wang, M. Wei, J. Gao, J. Hu, Y. Zhang, Corrosion process of pure magnesium in simulated body fluid, *Mater. Lett.* 62 (2008) 2181–2184. <https://doi.org/10.1016/j.matlet.2007.11.045>.
- [114] R. Radha, D. Sreekanth, Insight of magnesium alloys and composites for orthopedic implant applications – a review, *J. Magnes. Alloy.* 5 (2017) 286–312. <https://doi.org/10.1016/j.jma.2017.08.003>.
- [115] F. Liu, H. Zhao, R. Yang, F. Sun, Microstructure and Mechanical Properties of High Vacuum Die-Cast AlSiMgMn Alloys at as-Cast and T6-Treated Conditions, *Materials (Basel)*. 12 (2019) 2065. <https://doi.org/10.3390/ma12132065>.
- [116] C.A. Stüpp, C.L. Mendis, M. Mohedano, G. Szakács, F. Gensch, S. Müller, F. Feyerabend, D. Hotza, M.C. Fredel, N. Hort, Powder metallurgical synthesis of biodegradable mg-hydroxyapatite composites for biomedical applications, in: *Mater. Sci. Forum*, Springer International Publishing, Cham, 2015: pp. 165–171. <https://doi.org/10.4028/www.scientific.net/msf.828-829.165>.
- [117] S. Gallinetti, C. Canal, M.-P. Ginebra, Development and Characterization of Biphasic Hydroxyapatite/ $\beta$ -TCP Cements, *J. Am. Ceram. Soc.* 97 (2014) 1065–1073. <https://doi.org/10.1111/jace.12861>.

- [118] Z. Xing, B. Wang, W. Gao, C. Pan, J.K. Halsted, E.S. Chong, J. Lu, X. Wang, W. Luo, C.H. Chang, Y. Wen, S. Ma, K. Amine, X. Ji, Reducing CO<sub>2</sub> to dense nanoporous graphene by Mg/Zn for high power electrochemical capacitors, *Nano Energy*. 11 (2014) 600–610. <https://doi.org/10.1016/j.nanoen.2014.11>.
- [119] C.K. Chua, M. Pumera, Chemical reduction of graphene oxide: a synthetic chemistry viewpoint, *Chem. Soc. Rev.* 43 (2014) 291–312. <https://doi.org/10.1039/c3cs60303b>.
- [120] M. Rühle, Structure and composition of metal/ceramic interfaces, *J. Eur. Ceram. Soc.* 16 (1996) 353–365. [https://doi.org/10.1016/0955-2219\(95\)00194-8](https://doi.org/10.1016/0955-2219(95)00194-8).
- [121] H. Zhao, L. Li, S. Ding, C. Liu, J. Ai, Effect of porous structure and pore size on mechanical strength of 3D-printed comby scaffolds, *Mater. Lett.* 223 (2018) 21–24. <https://doi.org/10.1016/j.matlet.2018.03.205>.
- [122] X.P. Tan, Y.J. Tan, C.S.L. Chow, S.B. Tor, W.Y. Yeong, Metallic powder-bed based 3D printing of cellular scaffolds for orthopaedic implants: A state-of-the-art review on manufacturing, topological design, mechanical properties and biocompatibility, *Mater. Sci. Eng. C*. 76 (2017). <https://doi.org/10.1016/j.msec.2017.02.094>.
- [123] J.M. Cordell, M.L. Vogl, A.J. Wagoner Johnson, The influence of micropore size on the mechanical properties of bulk hydroxyapatite and hydroxyapatite scaffolds, *J. Mech. Behav. Biomed. Mater.* 2 (2009) 560–570. <https://doi.org/10.1016/j.jmbbm.2009.01.009>.
- [124] Y. Maazouz, E.B. Montufar, J. Guillem-Marti, I. Fleps, C. Öhman, C. Persson, M.P. Ginebra, Robocasting of biomimetic hydroxyapatite scaffolds using self-setting inks, *J. Mater. Chem. B*. 2 (2014) 5378–5386. <https://doi.org/10.1039/c4tb00438h>.
- [125] P. Skalka, K. Slámečka, E.B. Montufar, L. Čelko, Estimation of the effective elastic constants of bone scaffolds fabricated by direct ink writing, *J. Eur. Ceram. Soc.* 39 (2019) 1586–1594. <https://doi.org/10.1016/j.jeurceramsoc.2018.12.024>.
- [126] J. Chen, L. Tan, X. Yu, I.P. Etim, M. Ibrahim, K. Yang, Mechanical properties of magnesium alloys for medical application: A review, *J. Mech. Behav. Biomed. Mater.* 87 (2018) 68–79. <https://doi.org/10.1016/j.jmbbm.2018.07.022>.
- [127] Y. Ding, C. Wen, P. Hodgson, Y. Li, Effects of alloying elements on the corrosion behavior and biocompatibility of biodegradable magnesium alloys: A review, *J. Mater. Chem. B*. 2 (2014) 1912–1933. <https://doi.org/10.1039/c3tb21746a>.
- [128] J.W. Seong, W.J. Kim, Mg-Ca binary alloy sheets with Ca contents of  $\leq 1$ wt.% with high corrosion resistance and high toughness, *Corros. Sci.* 98 (2015) 372–381. <https://doi.org/10.1016/j.corsci.2015.05.068>.
- [129] S. Cai, T. Lei, N. Li, F. Feng, Effects of Zn on microstructure, mechanical properties and corrosion behavior of Mg-Zn alloys, *Mater. Sci. Eng. C*. 32 (2012) 2570–2577. <https://doi.org/10.1016/j.msec.2012.07.042>.
- [130] Y. Uematsu, K. Tokaji, M. Kamakura, K. Uchida, H. Shibata, N. Bekku, Effect of extrusion conditions on grain refinement and fatigue behaviour in magnesium alloys, *Mater. Sci. Eng. A*. 434 (2006) 131–140. <https://doi.org/10.1016/j.msea.2006.06.117>.

- [131] X. Zhao, S. Li, Y. Xue, Z. Zhang, An Investigation on Microstructure, Texture and Mechanical Properties of AZ80 Mg Alloy Processed by Annular Channel Angular Extrusion, *Materials (Basel)*. 12 (2019) 1001. <https://doi.org/10.3390/ma12061001>.
- [132] H.-J. Hu, Y.-L. Ying, Z.-W. Ou, X.-Q. Wang, Comparisons of microstructures and texture and mechanical properties of magnesium alloy fabricated by compound extrusion and direct extrusion, *Mater. Sci. Eng. A*. 695 (2017) 360–366. <https://doi.org/10.1016/j.msea.2017.03.103>.
- [133] S.H. Whang, Introduction, in: Nanostructured Met. Alloy., Elsevier, 2011: pp. xxi–xxxv. <https://doi.org/10.1016/b978-1-84569-670-2.50028-9>.
- [134] D. song YIN, E. lin ZHANG, S. yan ZENG, Effect of Zn on mechanical property and corrosion property of extruded Mg-Zn-Mn alloy, *Trans. Nonferrous Met. Soc. China (English Ed.)*. 18 (2008) 763–768. [https://doi.org/10.1016/s1003-6326\(08\)60131-4](https://doi.org/10.1016/s1003-6326(08)60131-4).
- [135] X. Wang, P. Zhang, L.H. Dong, X.L. Ma, J.T. Li, Y.F. Zheng, Microstructure and characteristics of interpenetrating  $\beta$ -TCP/Mg-Zn-Mn composite fabricated by suction casting, *Mater. Des.* 54 (2014) 995–1001. <https://doi.org/10.1016/j.matdes.2013.09.037>.
- [136] X. Wang, J.T. Li, M.Y. Xie, L.J. Qu, P. Zhang, X.L. Li, Structure, mechanical property and corrosion behaviors of (HA +  $\beta$ -TCP)/Mg-5Sn composite with interpenetrating networks, *Mater. Sci. Eng. C*. 56 (2015) 386–392. <https://doi.org/10.1016/j.msec.2015.06.047>.
- [137] B. Chen, K.-Y. Yin, T.-F. Lu, B.-Y. Sun, Q. Dong, J.-X. Zheng, C. Lu, Z.-C. Li, AZ91 Magnesium Alloy/Porous Hydroxyapatite Composite for Potential Application in Bone Repair, *J. Mater. Sci. Technol.* 32 (2016) 858–864. <https://doi.org/10.1016/j.jmst.2016.06.010>.
- [138] M. Suchenski, M.B. McCarthy, D. Chowaniec, D. Hansen, W. McKinnon, J. Apostolakos, R. Arciero, A.D. Mazzocca, Material Properties and Composition of Soft-Tissue Fixation, *Arthrosc. - J. Arthrosc. Relat. Surg.* 26 (2010) 821–831. <https://doi.org/10.1016/j.arthro.2009.12.026>.
- [139] A. Suryavanshi, V. Borse, V. Pawar, S. kotagudda ranganath, R. Srivastava, Material advancements in bone-soft tissue fixation devices, *Sci. Adv. TODAY*. 2 (2016) 25236.
- [140] V.K. Ganesh, K. Ramakrishna, D.N. Ghista, Biomechanics of bone-fracture fixation by stiffness-graded plates in comparison with stainless-steel plates, *Biomed. Eng. Online*. 4 (2005) 46. <https://doi.org/10.1186/1475-925x-4-46>.
- [141] H.F. Lei, Z.Q. Zhang, B. Liu, Effect of fiber arrangement on mechanical properties of short fiber reinforced composites, *Compos. Sci. Technol.* 72 (2012) 506–514. <https://doi.org/10.1016/j.compscitech.2011.12.011>.
- [142] A. Kaçıtis, I. Nulle, D. Ancans, Mechanical properties of composite biomass briquettes, in: Vide. Tehnol. Resur. - Environ. Technol. Resour., Rezekne Higher Education Institution, 2011: pp. 175–182. <https://doi.org/10.17770/etr2011vol1.898>.
- [143] G. Song, A. Atrens, D. StJohn, An Hydrogen Evolution Method for the Estimation of the Corrosion Rate of Magnesium Alloys, in: Essent. Readings Magnes. Technol., Springer International Publishing, Cham, 2016: pp. 565–572. <https://doi.org/10.1007/978-3-319->

48099-2\_90.

- [144] N.T. Kirkland, N. Birbilis, M.P. Staiger, Assessing the corrosion of biodegradable magnesium implants: A critical review of current methodologies and their limitations, *Acta Biomater.* 8 (2012) 925–936. <https://doi.org/10.1016/j.actbio.2011.11.014>.
- [145] H.R.B. Rad, M.H. Idris, M.R.A. Kadir, S. Farahany, Microstructure analysis and corrosion behavior of biodegradable Mg–Ca implant alloys, *Mater. Des.* 33 (2012) 88–97. <https://doi.org/10.1016/j.matdes.2011.06.057>.
- [146] Q. Yuan, Y. Huang, D. Liu, M. Chen, Effects of solidification cooling rate on the corrosion resistance of a biodegradable  $\beta$ -TCP/Mg–Zn–Ca composite, *Bioelectrochemistry.* 124 (2018) 93–104. <https://doi.org/10.1016/j.bioelechem.2018.07.005>.
- [147] R.-C. Zeng, Z.-Z. Yin, X.-B. Chen, D.-K. Xu, Corrosion Types of Magnesium Alloys, in: *Magnes. Alloy. - Sel. Issue*, IntechOpen, 2018. <https://doi.org/10.5772/intechopen.80083>.
- [148] X. Wang, Q. Nie, X. Ma, J. Fan, T. Yan, X. Li, Microstructure and properties of co-continuous ( $\beta$ -TCP+MgO)/Zn–Mg composite fabricated by suction exsorption for biomedical applications, *Trans. Nonferrous Met. Soc. China.* 27 (2017) 1996–2006. [https://doi.org/10.1016/s1003-6326\(17\)60224-3](https://doi.org/10.1016/s1003-6326(17)60224-3).
- [149] R. Zeng, K.U. Kainer, C. Blawert, W. Dietzel, Corrosion of an extruded magnesium alloy ZK60 component—The role of microstructural features, *J. Alloys Compd.* 509 (2011) 4462–4469. <https://doi.org/10.1016/j.jallcom.2011.01.116>.
- [150] R. Radha, D. Sreekanth, Mechanical and corrosion behaviour of hydroxyapatite reinforced Mg–Sn alloy composite by squeeze casting for biomedical applications, *J. Magnes. Alloy.* (2019). <https://doi.org/10.1016/j.jma.2019.05.010>.
- [151] P. Guo, Z. Cui, L. Yang, L. Cheng, W. Wang, B. Xu, Preparation of Mg/Nano-HA Composites by Spark Plasma Sintering Method and Evaluation of Different Milling Time Effects on Their Microhardness, Corrosion Resistance, and Biocompatibility, *Adv. Eng. Mater.* 19 (2017) 1600294. <https://doi.org/10.1002/adem.201600294>.
- [152] D. Zhao, A. Brown, T. Wang, S. Yoshizawa, C. Sfeir, W.R. Heineman, In vivo quantification of hydrogen gas concentration in bone marrow surrounding magnesium fracture fixation hardware using an electrochemical hydrogen gas sensor, *Acta Biomater.* 73 (2018) 559–566. <https://doi.org/10.1016/j.actbio.2018.04.032>.
- [153] M. Assad, N. Jackson, Biocompatibility Evaluation of Orthopedic Biomaterials and Medical Devices: A Review of Safety and Efficacy Models, in: *Encycl. Biomed. Eng.*, Elsevier, 2019: pp. 281–309. <https://doi.org/10.1016/b978-0-12-801238-3.11104-3>.
- [154] I. International standard, ISO 10993-5:2009 - Biological evaluation of medical devices- Part 5: Tests for in vitro cytotoxicity, 2009. <https://www.iso.org/standard/36406.html> (accessed April 3, 2020).
- [155] J. Fischer, M.H. Prosenc, M. Wolff, N. Hort, R. Willumeit, F. Feyerabend, Interference of magnesium corrosion with tetrazolium-based cytotoxicity assays☆, *Acta Biomater.* 6 (2010) 1813–1823. <https://doi.org/10.1016/j.actbio.2009.10.020>.

- [156] F. Witte, J. Fischer, J. Nellesen, H.-A. Crostack, V. Kaese, A. Pisch, F. Beckmann, H. Windhagen, In vitro and in vivo corrosion measurements of magnesium alloys, *Biomaterials*. 27 (2006) 1013–1018. <https://doi.org/10.1016/j.biomaterials.2005.07.037>.
- [157] K.M. Danikowski, T. Cheng, Colorimetric Analysis of Alkaline Phosphatase Activity in *S. aureus* Biofilm, *J. Vis. Exp.* 2019 (2019). <https://doi.org/10.3791/59285>.
- [158] Y. Zhang, Y. Li, H. Liu, J. Bai, N. Bao, Y. Zhang, P. He, J. Zhao, L. Tao, F. Xue, G. Zhou, G. Fan, Mechanical and Biological Properties of a Biodegradable Mg-Zn-Ca Porous Alloy, *Orthop. Surg.* 10 (2018) 160–168. <https://doi.org/10.1111/os.12378>.
- [159] D. Xia, Y. Liu, S. Wang, R.-C. Zeng, Y. Liu, Y. Zheng, Y. Zhou, In vitro and in vivo investigation on biodegradable Mg-Li-Ca alloys for bone implant application, *Sci. China Mater.* 62 (2019) 256–272. <https://doi.org/10.1007/s40843-018-9293-8>.
- [160] A.H. Yusop, A.A. Bakir, N.A. Shaharom, M.R. Abdul Kadir, H. Hermawan, Porous Biodegradable Metals for Hard Tissue Scaffolds: A Review, *Int. J. Biomater.* 2012 (2012) 1–10. <https://doi.org/10.1155/2012/641430>.
- [161] A.K. Khanra, H.C. Jung, K.S. Hong, K.S. Shin, Comparative property study on extruded Mg-HAP and ZM61-HAP composites, *Mater. Sci. Eng. A.* 527 (2010) 6283–6288. <https://doi.org/10.1016/j.msea.2010.06.031>.
- [162] B. Ratna Sunil, C. Ganapathy, T.S. Sampath Kumar, U. Chakkingal, Processing and mechanical behavior of lamellar structured degradable magnesium–hydroxyapatite implants, *J. Mech. Behav. Biomed. Mater.* 40 (2014) 178–189. <https://doi.org/10.1016/j.jmbbm.2014.08.016>.
- [163] J. Sun, M. Chen, G. Cao, Y. Bi, D. Liu, J. Wei, The effect of nano-hydroxyapatite on the microstructure and properties of Mg–3Zn–0.5Zr alloy, *J. Compos. Mater.* 48 (2014) 825–834. <https://doi.org/10.1177/0021998313478259>.
- [164] C. Prakash, S. Singh, K. Verma, S.S. Sidhu, S. Singh, Synthesis and characterization of Mg-Zn-Mn-HA composite by spark plasma sintering process for orthopedic applications, *Vacuum*. 155 (2018) 578–584. <https://doi.org/10.1016/j.vacuum.2018.06.063>.
- [165] M. Razavi, M.H. Fathi, M. Meratian, Microstructure, mechanical properties and bio-corrosion evaluation of biodegradable AZ91-FA nanocomposites for biomedical applications, *Mater. Sci. Eng. A.* 527 (2010) 6938–6944. <https://doi.org/10.1016/j.msea.2010.07.063>.
- [166] A. Feng, Y. Han, The microstructure, mechanical and corrosion properties of calcium polyphosphate reinforced ZK60A magnesium alloy composites, *J. Alloys Compd.* 504 (2010) 585–593. <https://doi.org/10.1016/j.jallcom.2010.06.013>.
- [167] A. Feng, Y. Han, Mechanical and in vitro degradation behavior of ultrafine calcium polyphosphate reinforced magnesium-alloy composites, *Mater. Des.* 32 (2011) 2813–2820. <https://doi.org/10.1016/j.matdes.2010.12.054>.
- [168] H.R. Zheng, Z. Li, C. You, D.B. Liu, M.F. Chen, Effects of MgO modified  $\beta$ -TCP nanoparticles on the microstructure and properties of  $\beta$ -TCP/Mg-Zn-Zr composites, *Bioact. Mater.* 2 (2017) 1–9. <https://doi.org/10.1016/j.bioactmat.2016.12.004>.

## Annex 1.

**Table 1A.** Comparison of mechanical properties, degradation rate and biocompatibility reports of biomaterials used in orthopaedics and most of the studied magnesium/calcium-phosphate composites manufactured by different methodologies.

Material	Density [g·cm <sup>-3</sup> ]	Elastic modulus [GPa]	Yield strength [MPa]	UTS [MPa]	Elongation [%]	Corrosion rate [mm·year <sup>-1</sup> ]	Biocompatibility	Ref.
Cortical bone	1.8–2.1	3–23	130–180	35–283 164–240 <sup>c</sup>	1.07–2.1	-	-	[8,9,160]
Cancellous bone	1.0–1.4	0.01–1.57	2–12	1.5–38	-	-	-	[8,160]
Ti alloys, Ti-6Al-4V	4.43	114	760–880	830–1025	12	-	-	[8,9]
316L stainless steel	8.0	190	200–300	450–650	30–40	-	-	[8,9]
Co-Cr alloys	8.3–9.2	210–230	450–100	-	-	-	-	[8,11]
WE43 Mg alloy, T6	1.84	44	170	220	-	-	-	[160]
Synthetic HA	3.1	73–117	600	40–200 100–900	-	-	-	[8,9]
Pure Mg, annealed	1.74	45	90	160	-	-	-	[160]
Mg / 10 wt. % HA (P/M)	-	-	117.3 ± 12.1	171.6 ± 16.6	6.7 ± 1.4	1.36	~ 95% (4 d, L929)	[51,84]
Mg / 20 wt. % HA (P/M)	-	58	105.8 ± 9.8	146.9 ± 11.3	4.3 ± 0.7	1.38	~ 85% (4 d, L929)	[51,84]
Mg / 30 wt. % HA (P/M)	-	-	71.7 ± 7.8	92.1 ± 10.8	2.6 ± 0.5	1.43	~ 65% (4 d, L929)	[51,84]
Mg / 40 wt. % HA (P/M)	-	65	-	68	-	~40.0	-	[51]
Mg / 5 wt. % HA (Stirring casting)	-	-	122.3	171.1	-	-	-	[51]
Mg / 10 wt. % HA (Stirring casting)	-	-	137.0	146.4	-	-	-	[51]
Mg / 15 wt. % HA (Stirring casting)	-	-	129.6 147.1 <sup>c</sup>	136.7 298.2 <sup>c</sup>	0.3	-	-	[51,161]
Mg / 5 wt. % HA (P/M Extrusion)	1.714	-	222 <sup>c</sup>	452 <sup>c</sup>	18.5 <sup>c</sup>	~15* (100 h, PBS sol. 37 °C)	-	[78]
Mg / 10 wt. % HA (P/M Extrusion)	1.746	-	219 <sup>c</sup>	415 <sup>c</sup>	17.5 <sup>c</sup>	~23* (100 h, PBS sol. 37 °C)	-	[78]
Mg / 15 wt. % HA (P/M Extrusion)	1.749	-	216 <sup>c</sup>	371 <sup>c</sup>	22.3 <sup>c</sup>	~61* (100 h, PBS sol. 37 °C)	-	[78]

Continue Table 1A...

Material	Density [g·cm <sup>-3</sup> ]	Elastic modulus [GPa]	Yield strength [MPa]	UTS [MPa]	Elongation [%]	Corrosion rate [mm·year <sup>-1</sup> ]	Biocompatibility	Ref.
Mg / 1-5 wt.% HA (P/M Induction heating)	~1.74-1.78	-	-	-	-	8-54.8 (Polarization, SBF)	-	[85]
ZM61 / 15 wt.% HA (Stirring casting)	-	-	225.5 245.3 <sup>c</sup>	225.5 388.3 <sup>c</sup>	0.3	-	-	[51,161]
Mg / 10 wt.% HA (lamellar, P/M)	-	54.2 ± 5.3	-	-	-	-	-	[162]
Mg-Sn / 5 wt.% HA (Stirring casting)	-	66.6 <sup>c</sup>	196 <sup>c</sup>	278.55 <sup>c</sup>	8.03 <sup>c</sup>	354.9 (Polarization, SBF 35 °C)	-	[150]
AZ91D / 20 wt.% HA (P/M)	-	40	264.3 ± 10	-	~2.5	2.0-3.2 (72 h under cell solution)	~100% (2 d, RAW264.7) ~225% (2 d, MG63) ~130% (3 d, HBDC)	[4,51]
Mg-Zn-Zr / 1 wt.% HA nanoparticles (Stirring casting)	-	-	-	-	-	0.75 (20 d in SBF)	Better cytocompatibility than bare alloy	[51]
Mg-3Zn-0.5Zr / 0.5 wt.% HA (Stirring casting)	-	-	255	281	15.4	7.83 (24 days in SBF 37 °C)	-	[163]
Mg-3Zn-0.5Zr / 1 wt.% HA (Stirring casting)	-	-	256	285	18.6	6.45 (24 days in SBF 37 °C)	-	[163]
Mg-3Zn-0.5Zr / 1.5 wt.% HA (Stirring casting)	-	-	275	302	20.9	7.12 (24 days in SBF 37 °C)	-	[163]
Mg-Zn-Mn / 10-20 wt.% HA (P/M-SPS)	-	~30-45	-	-	-	0.97 (Polarization, Ringer Sol.)	-	[164]
Mg / 10 wt.% HA (P/M-SPS)	-	~35-52	-	-	-	0.007-0.113 (Polarization) ~80-720 (H <sub>2</sub> evolution, SBF)	High relative grow rate (72h, L-929)	[151]
AZ91 / 10 Wt.% FA (P/M)	-	34.1	116.5 <sup>c</sup>	~125	5.78	1.671 (Ringer Sol. 37 °C)	-	[51,165]

Continue Table 1A ...

Material	Density [g·cm <sup>-3</sup> ]	Elastic modulus [GPa]	Yield strength [MPa]	UTS [MPa]	Elongation [%]	Corrosion rate [mm·year <sup>-1</sup> ]	Biocompatibility	Ref.
<b>AZ91 / 20 Wt.% FA (P/M)</b>	-	37.5	123.2 °	~130	5.32	0.052 (Ringer Sol. 37 °C)	-	[51,165]
<b>AZ91 / 30 Wt.% FA (P/M)</b>	-	42.3	112.4 °	~120	4.51	0.008 (Ringer Sol. 37 °C)	-	[51,165]
<b>ZK60 / 10 wt.% CPPp (P/M)</b>	-	38	~215 ~230 °	~230 ~470 °	-	0.002 (10 days in SBF 37 °C)	-	[51,166]
<b>ZK60 / 20 wt.% CPPp (P/M)</b>	-	39	~210 ~230 °	~220 494.88 °	-	0.002 (10 days in SBF 37 °C)	-	[51,166]
<b>ZK60 / 30 wt.% CPPp (P/M)</b>	-	38	~195 ~230 °	~200 ~470 °	-	0.002 (10 days in SBF 37 °C)	-	[51,166]
<b>ZK60 / 2.5 wt.% CPPp (P/M)</b>	-	43	~265	~285	-	-	-	[76,167]
<b>ZK60 / 5 wt.% CPPp (P/M)</b>	-	47	319.5	337.4	-	-	-	[76,167]
<b>Mg-3Zn-0.8Zr / 0.5-1.5 wt.% β-TCP (Stirring casting)</b>	-	-	-	~260-280	~15.0	- (Polarization, SBF 37 °C)	-	[80]
<b>Mg-6Zn / 5 wt.% β-TCP (P/M)</b>	1.862	36	-	345 °	-	13.52 (Polarization, SBF 37 °C)	Grade ~0-1 cytotoxicity, L-929 Good in-vivo biocompatibility	[88]
<b>Mg-6Zn / 10 wt.% β-TCP (P/M)</b>	1.904	24	-	339 °	-	15.04 (Polarization, SBF 37 °C)	Grade ~0-1 cytotoxicity, L-929 Good in-vivo biocompatibility	[88]
<b>Mg-6Zn / 15 wt.% β-TCP (P/M)</b>	1.943	21	-	284 °	-	17.56 (Polarization, SBF 37 °C)	Grade ~0-1 cytotoxicity, L-929 Good in-vivo biocompatibility	[88]
<b>Mg / 10-20 wt.% β-TCP (P/M-SPS)</b>	-	-	70-101 °	~220-250 °	~6.5-12 °	-	High cell adhesion Bone marrow derived mesenchymal stem cells (BMSCs)	[86,95]

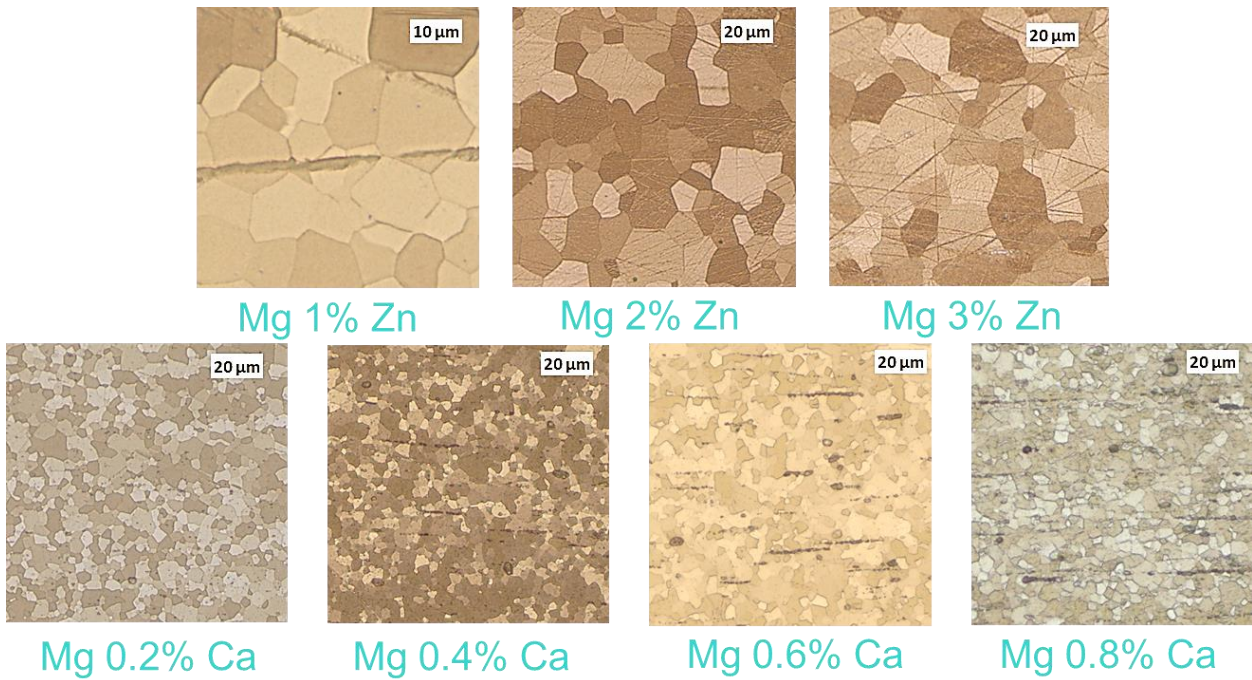
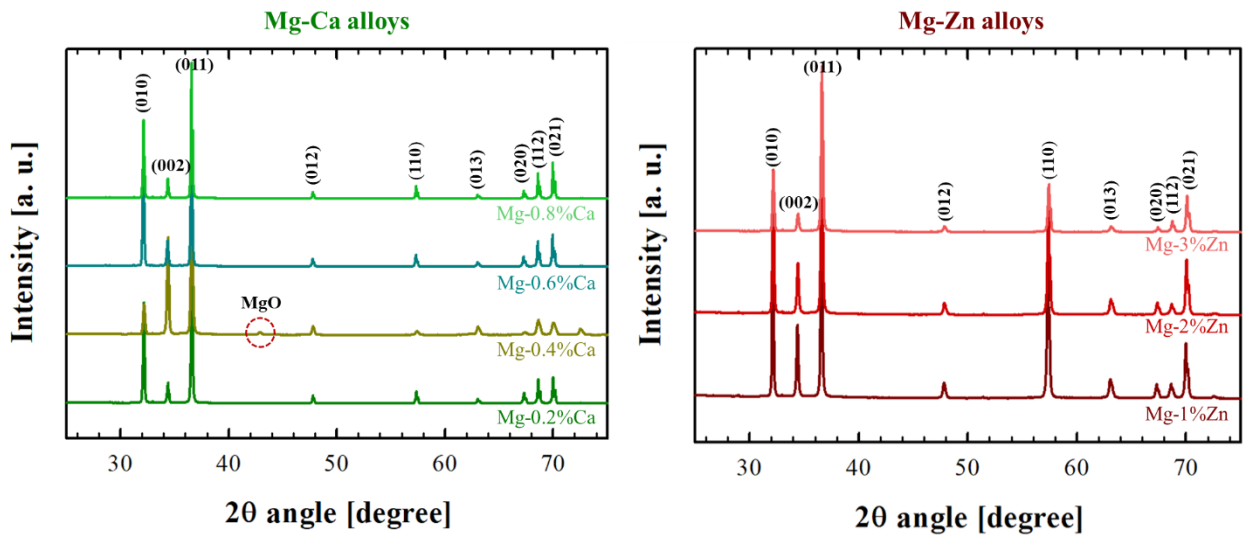
Continue Table 1A ...

Material	Density [g·cm <sup>-3</sup> ]	Elastic modulus [GPa]	Yield strength [MPa]	UTS [MPa]	Elongation [%]	Corrosion rate [mm·year <sup>-1</sup> ]	Biocompatibility/ cell viability	Ref.
Mg-3Zn-1Ca / 1 wt.% β-TCP (Stir-Shear casting)	-	45.3 ± 3	125.4 ± 2	150 ± 3	2.85 ± 0.2	-	-	[79]
Mg-3Zn-0.8Zr / 1 wt.% β-TCP-MgO (Stir-Shear casting)	-	-	295.58	346.11	10.0	-	Cytocompatible (Rat osteoblast, 7d)	[168]
Mg-2Zn-0.5Ca / 1 wt.% β-TCP	-	-	-	-	-	~12.5 (14 d, SBF 37 °C)	-	[146]
Mg-1wt.%Ca / 87% porous HA-TCP (Liquid infiltration)	-	-	-	128.7 ± 15.1 <sup>c</sup>	13.5 ± 0.7 <sup>c</sup>	~3.4 (20 d, Hank's Sol. 37 °C)	100 % corrosion extract showed ~55 % (5 d, L-929 and MG63 )	[51,83]
Mg-3Zn-1Mn / 92% porous β-TCP (Liquid infiltration – vacuum casting)	-	-	-	140 ± 20 <sup>c</sup>	~10.0 <sup>c</sup>	-	-	[135]
Mg-1Ca / 92% porous β-TCP (Liquid infiltration)	-	-	-	147 ± 13 <sup>c</sup>	18 ± 1 <sup>c</sup>	-	-	[81,82]
Mg-1Ca / 92% porous 65β-TCP-35HA (Liquid infiltration)	-	-	-	130 ± 17 <sup>c</sup>	17 ± 1 <sup>c</sup>	-	-	[82]
Mg-1Ca / 92% porous 40β-TCP-60HA (Liquid infiltration)	-	-	-	110 ± 22 <sup>c</sup>	15 ± 3 <sup>c</sup>	-	-	[82]
Mg-1Ca / 92% porous HA (Liquid infiltration)	-	-	-	68 ± 25 <sup>c</sup>	8 ± 2 <sup>c</sup>	-	-	[82]
Mg-5Sn / 90% porous 60β-TCP-40HA (Liquid infiltration)	-	-	-	176 <sup>c</sup>	~30.0 <sup>c</sup>	-	-	[136]
AZ91 / 75% porous HA (Liquid infiltration – squeeze casting)	-	-	-	~108.2 <sup>c</sup>	~10.0 <sup>c</sup>	-	-	[137]

\*Value taken from graphs presented in the publication

<sup>c</sup> values obtained by compression

**Annex 2.** X-ray diffraction patterns and characteristic microstructure of processed Mg-alloys



### Annex 3. Conventional simulated body fluid preparation

**Table 2A.** Reagents, their purities and amounts for preparing 1000 mL of the c-SBF

Reagent	Purity [%]	Amount
NaCl	> 99.5	8.036 g
NaHCO <sub>3</sub>	> 99.5	0.352 g
Na <sub>2</sub> CO <sub>3</sub>	> 99.5	—
KCl	> 99.5	0.225 g
K <sub>2</sub> HPO <sub>4</sub> · 3H <sub>2</sub> O	> 99.0	0.230 g
MgCl <sub>2</sub> · 6H <sub>2</sub> O	> 98.0	0.311 g
1.0 M HCl	—	40.0 mL
CaCl <sub>2</sub>	> 95.0	0.293 g
Na <sub>2</sub> SO <sub>4</sub>	> 99.0	0.072 g
TRIS	> 99.9	6.063 g
1.0 M HCl	—	~0.2 mL

Reagents are listed in sequence of dissolution

TRIS = tris(hydroxymethyl)aminomethane

The final solution is buffered at pH 7.40 at 36.5 °C with TRIS and 1.0 M HCl aqueous solution

## LIST OF ABBREVIATIONS

AA6061	Aluminium alloy 6061
ALP	Alkaline phosphatase
Ar	Argon
BGs	Bioglasses
Ca	Calcium
CAIS	Current-Assisted Infiltration Sintering
CAMI	Current-Assisted Metal Infiltration
CaP	Calcium phosphate(s)
CDHA	Calcium-deficient hydroxyapatite
CPP	Calcium pyrophosphate, $\text{Ca}_2\text{P}_2\text{O}_7$
CRH	Corrosion rate from hydrogen evolution
$\text{CR}_p$	Corrosion rate from the polarization test
c-SBF	Conventional simulated body fluid
DIW	Direct Ink writing
DMEM	Dulbecco's Modified Eagle's Medium
DR	Degradation rate
E	Young's modulus
$E_{\text{corr}}$	Corrosion potential
$\epsilon$	elongation (strain)
EDX	Energy dispersive X-ray SPECTROSCOPY
EU	European Union
FBS	Foetal bovine serum
FGM's	Functional graded materials
Gd	Gadolinium
$\text{H}_2$	Hydrogen
HA	Hydroxyapatite
$i_{\text{corr}}$	Corrosion current density
ICSD	Inorganic Crystal Structure Database
$J_{\text{corr}}$	Corrosion current density
Mg	Magnesium

Mg/CaP	Magnesium - Calcium phosphate composites
MMCs	Metal matrix composites
P	Phosphorus
PBS	Phosphate buffer solution
pNP	p-Nitrophenol
SBF	Simulated body fluid
SEM	Scanning electron microscopy
SF <sub>6</sub>	Sulphur hexafluoride
Si	Silicon
SiC	Silicon carbide
Sol.	Solution
SPS	Spark plasma sintering
Sr	Strontium
TCP	Tricalcium phosphate
TCPS	Tissue culture-grade polystyrene
US	American dollars
UTS	Ultimate tensile strength
vol. %	Volume percent
wt. %	Weight percent
XRD	X-ray diffraction
Y	Yttrium
YS	Yield strength
Zn	Zinc
Zr	Zirconium
α'-TCP	Alpha prima tricalcium phosphate, hexagonal
α-TCP	Alpha tricalcium phosphate, monoclinic
β-TCP	Beta tricalcium phosphate, rhombohedral
μCT	X-ray micro computed tomography
σ <sub>max</sub>	Compressive strength
σ <sub>y</sub>	Compressive yield strength

## LIST OF PUBLICATIONS

- [1] E.B. Montufar, K. Slámečka, **M. Casas-Luna**, P. Skalka, E. Ramírez-Cedillo, M. Zbončák, J. Kaiser, L. Čelko, Factors governing the dimensional accuracy and fracture modes under compression of regular and shifted orthogonal scaffolds, *J. Eur. Ceram. Soc.* (2020). <https://doi.org/10.1016/j.jeurceramsoc.2020.03.045>
- [2] **M. Casas-Luna**, J.A. Torres-Rodríguez, O.U. Valdés-Martínez, N. Obradović, K. Slámečka, K. Maca, J. Kaiser, E.B. Montufar, L. Čelko, Robocasting of controlled porous CaSiO<sub>3</sub>–SiO<sub>2</sub> structures: Architecture – Strength relationship and material catalytic behavior, *Ceram. Inter.* 46 (2020) 8853-8861. <https://doi.org/10.1016/j.ceramint.2019.12.130>
- [3] L. Čelko, M. Menelaou, **M. Casas-Luna**, M. Horynová, T. Musálek, M. Remešová, S. Diaz-De-La-Torre, K. Morsi, J. Kaiser, Spark Plasma Extrusion and the Thermal Barrier Concept, *Metall. Mater. Trans. B* 50 (2019) 656-665. <https://doi.org/10.1007/s11663-018-1493-3>
- [4] **M. Casas-Luna**, H. Tan, S. Tkachenko, D. Salamon, E.B. Montufar, Enhancement of mechanical properties of 3D-plotted tricalcium phosphate scaffolds by rapid sintering, *J. Eur. Ceram. Soc.* 39 (2019) 4366-4374. <https://doi.org/10.1016/j.jeurceramsoc.2019.05.055>
- [5] S. Tkachenko, M. Horynová, **M. Casas-Luna**, S. Diaz-de-la-Torre, K. Dvořák, L. Celko, J. Kaiser, E.B. Montufar, Strength and fracture mechanism of iron reinforced tricalcium phosphate cermet fabricated by spark plasma sintering. *J. Mech. Biomed. Mater.* 81 (2018) 16-25. <https://doi.org/10.1016/j.jmbbm.2018.02.016>
- [6] E.B. Montufar, **M. Casas-Luna**, M. Horynová, S. Tkachenko, Z. Fohlerová, S. Diaz-de-la-Torre, K. Dvořák, L. Čelko, J. Kaiser, High strength, biodegradable and cytocompatible alpha tricalcium phosphate-iron composites for temporal reduction of bone fractures. *Acta Biomater.* 70 (2018) 293-303. <https://doi.org/10.1016/j.actbio.2018.02.002>
- [7] **M. Casas-Luna**, M. Horynová, S. Tkachenko, L. Klakurková, L. Celko, S. Diaz-de-la-Torre, E. Montufar, Chemical Stability of Tricalcium Phosphate–Iron Composite during Spark Plasma Sintering. *J. Comp. Sci.* 2 (2018) 51. <https://doi.org/10.3390/jcs2030051>
- [8] **M. Casas-Luna**, S. Tkachenko, M. Horynová, L. Klakurková, P. Gejdos, S. Diaz-De-La-Torre, L. Celko, J. Kaiser, E.B. Montufar, Interpenetrated magnesium–tricalcium phosphate composite: Manufacture, characterization and in vitro degradation test. *Acta Metall. Sinica (English Letters)* 30 (2017) 319-325. <https://doi.org/10.1007/s40195-017-0560-0>

- [9] M. Horynová, **M. Casas-Luna**, E.B. Montufar Jimenéz, S. Díaz de la Torre, L. Čelko, L. Klakurková, G. Diéguez-Trejo, K. Dvořák, T. Zikmund, J. Kaiser, Fracture mechanism of interpenetrating iron-tricalcium phosphate composite, vol 258, Trans. Tech. Publ. (2017) 333-336. <https://doi.org/10.4028/www.scientific.net/SSP.258.333>
- [10] S. Díaz de la Torre, L. Čelko, **M. Casas-Luna**, E.B. Montufar Jimenéz, On the preparation of advanced materials via pulsed electric current sintering procedures, vol 258, Trans. Tech. Publ. (2017) 436-439. <https://doi.org/10.4028/www.scientific.net/SSP.258.436>
- [11] **M. Casas-Luna**, E.B. Montufar Jimenéz, M. Horynová, P. Gejdoš, L. Klakurková, S. Díaz de la Torre, J. Kaiser, L. Čelko, Tricalcium phosphate-magnesium interface: Microstructure and properties, vol 258, Trans. Tech. Publ. (2016) 412-415. <https://doi.org/10.4028/www.scientific.net/SSP.258.412>
- [12] E.B. Montufar, M. Horynová, **M. Casas-Luna**, S. Diaz-De-La-Torre, L. Celko, L. Klakurková, Z. Spotz, G. Diéguez-Trejo, Z. Fohlerová, K. Dvorak, Spark Plasma Sintering of Load-Bearing Iron–Carbon Nanotube-Tricalcium Phosphate CerMets for Orthopaedic Applications. JOM 68 (2016) 1134-1142. <https://doi.org/10.1007/s11837-015-1806-9>

## PATENTS

- Mexican patent No. 365570: “Proceso de obtención de compósitos metálicos porosos con hidroxiapatita para implantes y el compósito de metal-hidroxiapatita” (Fabrication process of porous metallic composites with hydroxyapatite for implants and the metal-hydroxyapatite composite).
- Patent application MX/a/2015/016632: “Proceso de infiltración metálica en redes porosas cerámicas y/o metálicas utilizando la técnica de sinterizado por infiltración asistida por corriente eléctrica” (Metal infiltration process of porous ceramics and/or metallic networks using the technique of current-assisted infiltration sintering).

## **INTERNSHIP, TRAININGS AND OTHER ACTIVITIES**

### Internships:

- 2-month training internship (summer 2017) at the Magnesium Innovation Centre in the Helmholtz Centre in Geesthacht, Germany (MAGIC – HZG), under the supervision of Prof. Norbert Hort. The internship helped me in the design and casting of magnesium alloys containing calcium and zinc.
- 2-month internship (spring 2018) at the National Polytechnic Institute of Mexico (CIITEC – IPN) with Prof. Sebastián Díaz de la Torre, in order to perform the infiltration of calcium phosphate scaffolds with magnesium and Mg alloys

### Trainings:

- Self-user of the core facilities at CEITEC-VUT for SEM-EDX, XRD, XPS, RAMAN, micro hardness indentation, metallographic preparation

### Conferences:

- 8th International Conference on Materials Structure & Micromechanics of Fracture (MSMF8).
- 2015 and 2017 European Biomaterial Society Congress
- OZ-16 International Symposium on Nanostructures
- 25th ISMANAM congress
- 10th BIOMETAL congress
- Advanced Ceramics Applications VII 2018 congress
- Advanced Ceramics Applications VIII 2019 congress
- Fracture of Advanced Ceramics 2019 congress

### Awards and scholarships:

- PhD Talent 2015
- Erasmus-trainings
- CEITEC PhD scholarship

## **PARTICIPATION IN RESEARCH PROJECTS:**

- VUT-junior project 2018: “Wollastonite: synthesis and processing of porous scaffolds through 3D-printing”.
- VUT-junior project 2019 in collaboration with the Faculty of Civil Engineering (FAST): “Synthesis, processing and characterization of advanced BaO-MgO-Al<sub>2</sub>O<sub>3</sub>-SiO<sub>2</sub> system, as a candidate for near-future thermal and environmental barrier coatings”.
- VUT-junior project 2019: “Characterization and degradation assessment of magnesium-based biomaterials under physiological conditions”.

## LIST OF FIGURES

<b>Figure 1.</b> Schematic representation of material design requirement for biomaterials .....	11
<b>Figure 2.</b> Schematic time-line for an ideal degradable biomaterial depicting the healing period against the degradation time [3]. .....	12
<b>Figure 3.</b> Pourbaix (potential-pH) diagram of pure Mg – H <sub>2</sub> O at 25 °C and schema of corrosion mechanism [53]. .....	16
<b>Figure 4.</b> Schematic process for the robocasting manufacturing of porous scaffolds for orthopaedic applications [69]. .....	20
<b>Figure 5.</b> Schematic of the current-activated pressure-assisted infiltration for the production of interpenetrated ceramic-metal composites, and pictures of the resulting Ti <sub>2</sub> AlC foams infiltrated by aluminium alloy [71]. .....	22
<b>Figure 6.</b> Schematic of the current-assisted metal infiltration arrangement and graphite die design to avoid the loading of fragile preform, and pictures of Mg/bovine bone before and after metal infiltration. ....	23
<b>Figure 7.</b> Graphite-die design and initial arrangement for the current-assisted metal infiltration technique. ....	36
<b>Figure 8.</b> XRD pattern and microstructure observation of a) initial β-TCP powder (VWR, Belgium); and b) XRD after sintering at 1100 °C for 5 h. ....	44
<b>Figure 9.</b> a) Computed design for the construction of cylindrical scaffolds in blue and real-time sample printing by means of robocasting process; b) characteristic sample after sintering with a nominal pore size of 150 μm; c) top view of a characteristic scaffold with a 150-μm pore size; d) top view of a characteristic scaffold with a nominal 1000-μm pore size; e) SEM image of typical microstructure after the sintering of β-TCP strands; and f) detailed micrograph of the microstructure and inner porosity of the β-TCP scaffolds. ....	45
<b>Figure 10.</b> a) Characteristic screw-like specimen obtained from the CAMI of β-TCP preforms with a nominal pore size of 500 μm infiltrated by pure Mg; b) optical microscopy images from a transversal cut of the cylindrical sample (the metallic and ceramic phases are marked); c) detail of a cylindrical strand revealing the molten metal infiltration and interaction between the materials. ....	46

<b>Figure 11.</b> Percentage of infiltration degree in Mg/ $\beta$ -TCP composites obtained by CAMI with respect to the initial pore size of the ceramic preforms. Insets show the characteristic longitudinal cut of the imaging reconstruction by $\mu$ -CT, where the ceramic phase is highlighted in yellow and the Mg in green. ....	47
<b>Figure 12.</b> $\mu$ -CT reconstruction of Mg/ $\beta$ -TCP composites with different nominal pore sizes of the ceramic preforms. Mg is highlighted in green colour, $\beta$ -TCP is in yellow, and the remaining porosity is in blue.....	48
<b>Figure 13.</b> X-ray diffraction pattern from the interpenetrated Mg/ $\beta$ -TCP composite. ....	49
<b>Figure 14.</b> Optical microscopy images of Mg/ $\beta$ -TCP interpenetrated composite. a) General overview; b) detail of the interface; c) detail of the metallic phase revealing the presence of Mg <sub>2</sub> Ca intermetallic phase; d) SEM micrograph and distribution of elements registered by EDX from a characteristic region of the composite. ....	50
<b>Figure 15.</b> Compressive stress-strain curves for different $\beta$ -TCP preforms infiltrated with pure Mg by CAMI. ....	51
<b>Figure 16.</b> a) Initial Mg/ $\beta$ -TCP discs for the degradation test; b) Mg/ $\beta$ -TCP disc after 24 h of immersion in saline solution; c) Mg/ $\beta$ -TCP sample after the removal of corrosion products; d) corrosion rates over time for pure magnesium and Mg/ $\beta$ -TCP composite. ....	53
<b>Figure 17.</b> XRD of the different conditions for the synthesis of $\beta$ -TCP. Variables are the Ca/P ratio, pH value and calcination temperature.....	55
<b>Figure 18.</b> X-ray diffraction patterns of synthesised CaP powders. Arrow indicates the transformation of $\alpha$ -TCP after the hydrolysis.....	58
<b>Figure 19.</b> Characteristic consolidated HA (a-c) and CDHA (d-f) scaffolds obtained by the robocasting of ceramic pastes.....	60
<b>Figure 20.</b> (a) Characteristic X-ray diffraction patterns of the initial pure Mg and Mg alloys. Representative optical micrographs of (b) Mg-1%Zn, (c) Mg-0.2%Ca, and (d) pure Mg. ....	63
<b>Figure 21.</b> Degradation rates of Mg alloys through the first month of immersion in SBF at 37 °C, calculated by the mass loss technique.....	65
<b>Figure 22.</b> Degradation rate assessment of Mg alloys along 2 weeks of immersion in SBF solution at 37 °C by the H <sub>2</sub> evolution assay.....	66
<b>Figure 23.</b> Cell proliferation assay of produced Mg alloys containing the lowest and the highest concentration of alloying elements compared with pure Mg. ....	67

<b>Figure 24.</b> Current-assisted metal infiltration (CAMI) temperature ramp processing.....	69
<b>Figure 25.</b> Characteristic HA and CDHA structures. (a) Top view of a HA preform after sintering and its characteristic microstructure; (b) Top view of a CDHA preform and its characteristic microstructure; (c) pore-size distribution of the HA and CDHA preforms measured by mercury intrusion porosimetry. ....	72
<b>Figure 26.</b> Image reconstruction made from X-ray computed tomography of Mg/CaP interpenetrated composites together with the calculated degree of infiltration and volumetric phase percent. ....	73
<b>Figure 27.</b> Representative X-ray diffraction patterns of interpenetrated Mg-based composites (Mg/HA and Mg/CDHA). ....	75
<b>Figure 28.</b> Representative micrographs of typical interpenetrated HA-based composites with pure Mg and Mg-0.2%Ca alloy: a) Mg/HA; b) detail of the interface between HA and Mg; c) Mg-0.2%Ca/HA composite; d) detail of the interface between Mg-0.2%Ca and HA. ....	76
<b>Figure 29.</b> Representative micrographs of the interpenetrated CDHA-based composites with different Mg alloys: a) Mg/CDHA; b) detail of the interface between CDHA and pure Mg; c) Mg-0.2%Ca/CDHA; d) detail of the interface between CDHA and Mg-0.2%Ca alloy; e) Mg-1%Zn/CDHA; and f) detail of the interface between CDHA and Mg-1%Zn alloy. ....	77
<b>Figure 30.</b> a) Lineal EDX chemical analysis on typical interface between Mg and CaP, interface from Mg/CDHA composite. b) Representative micrograph of interpenetrated composites, Mg-0.2%Ca/HA with Mg <sub>2</sub> Ca intermetallic phase; and c) detail of Mg phase pointing out the Mg <sub>2</sub> Ca intermetallic as a product of the reduction of the CaP phase. ....	78
<b>Figure 31.</b> Room-temperature compressive mechanical properties of initial Mg alloys, CaP preforms, and processed interpenetrated composites: a) yield strength and b) ultimate compressive strength. ....	82
<b>Figure 32.</b> Representative stress-strain curves at room temperature from the compression test of interpenetrated Mg/CaP composites: a) Pure Mg-based composites; b) Mg-0.2%Ca-based composites; c) Mg-1%Zn-based composites; d) initial CaP preforms; e) typical fracture surface in HA-based composites; and f) typical fracture surface in CDHA-based composites. ....	83
<b>Figure 33.</b> Corrosion rate profiles calculated from the H <sub>2</sub> evolution test of: a) pure Mg-based composites; b) Mg-0.2%Ca-based composites; and c) Mg-1%Zn-based composites. Also,	

characteristic polarization curves of d) pure Mg-based composites; e) Mg-0.2%Ca-based composites; and f) Mg-1%Zn-based composites..... 87

**Figure 34.** Comparison of the corrosion mechanism of initial Mg alloys and different Mg/CaP interpenetrated composites after the potentiodynamic test in SBF at room temperature. .... 90

**Figure 35.** SAOS-2-cell proliferation represented as cell count per well. Data are expressed as the mean  $\pm$  S.D. The significant differences between similar sets of samples at particular time points (Mann-Whitney U test;  $p < 0.05$ ;  $n = 8$  per each group) are marked by corresponding group legend pattern..... 91

**Figure 36.** SAOS-2 viability represented as % of untreated control. Data are expressed as the mean  $\pm$  S.D. The significant differences between similar sets of samples at particular time points (Mann-Whitney U test;  $p < 0.05$ ;  $n = 16$  per each group) are marked by corresponding group legend pattern. The significant difference of a particular group from 100% of untreated control is marked by # (Student T-test,  $p < 0.05$ ;  $n = 16$  per each group)..... 93

**Figure 37.** Alkaline phosphatase activity of SAOS-2. Data are expressed as the mean  $\pm$  S.D. The significant differences between time points for each sample are shown above each group and time point (one-way ANOVA;  $p < 0.05$ ;  $n = 3$  per each group). No significant differences between samples at particular time points (Mann-Whitney U test;  $p < 0.05$ ;  $n = 3$  per each group) were detected..... 95

## LIST OF TABLES

<b>Table 1.</b> Chemical formulas, Ca/P atomic ratios and solubility of some CaP compounds .....	15
<b>Table 2.</b> Mechanical and corrosion properties of binary Mg alloys for biodegradable implants [11,56]. .....	18
<b>Table 3.</b> Number of interpenetrated Mg/CaP composites produced by the infiltration of CaP preforms with pure Mg and Mg alloys.....	37
<b>Table 4.</b> Nominal dimensions and final dimensions after the sintering of preliminary $\beta$ -TCP scaffolds. ....	46
<b>Table 5.</b> Mechanical properties of different interpenetrated Mg/ $\beta$ -TCP composites based on the initial nominal pore size of the ceramic preform measured under compressive test.....	51
<b>Table 6.</b> Synthesis conditions for HA and $\beta$ -TCP powders produced by chemical precipitation and after 3-hour heat treatment, with the resulting chemical composition by the Rietveld analysis...	56
<b>Table 7.</b> Final dimensions and shrinkage of bioceramic scaffolds after consolidation processing. ....	59
<b>Table 8.</b> Elemental analysis (wt. %) of pure Mg and processed binary Mg alloys.....	61
<b>Table 9.</b> Comparison of degradation rate calculated by the mass loss and H <sub>2</sub> evolution techniques for pure Mg and its alloys containing a low amount of Ca or Zn after 2 weeks in SBF at 37 °C.	64
<b>Table 10.</b> Chemical composition of the interface in the Mg/CaP composites.....	79
<b>Table 11.</b> Compressive mechanical properties of interpenetrated Mg/CaP composites and the initial constituents. ....	79
<b>Table 12.</b> Degradation rate of produced interpenetrated Mg/CaP composites and their metallic counterparts estimated by the H <sub>2</sub> evolution assessment after 2 weeks in SBF at 37 °C. ....	85
<b>Table 13.</b> Corrosion potential, corrosion current density and degradation rate estimated by the Tafel extrapolation of obtained polarization curves using SBF at room temperature. ....	88
<b>Table 1A.</b> Comparison of mechanical properties, degradation rate and biocompatibility reports of biomaterials used in orthopaedics and most of the studied magnesium/calcium-phosphate composites manufactured by different methodologies .....	114